DUCTILITY IN TUNGSTEN: A TREATISE ON PROCESSING, CHARACTERIZATION, AND ANALYSIS OF PLASTICALLY DEFORMED MATERIAL

Dissertation

by

ZACHARY SOLOMON LEVIN

Submitted to the Office of Graduate and Professional Studies of
Texas A&M University
in partial fulfillment of the requirements for the degree of

DOCTOR OF PHILOSOPHY

Chair of Committee,	Karl T. Hartwig
Committee Members,	Thomas Lalk
	Donald G. Naugle
	Ibrahim Karaman
Head of Department,	Andreas A. Polycarpou

December 2016

Major Subject: Mechanical Engineering

ABSTRACT

The goal of this work was to increase the room temperature ductility of polycrystalline tungsten to over 10% tensile elongation. In conjunction with this, the objective goals were to determine the underlying deformation mechanisms and the microstructure influences that alter the mechanical behavior.

In this work, centimeter diameter polycrystalline tungsten rods were plastically deformed to strains between 1.15-4.6 through equal channel angular extrusion (ECAE) at 320^{o}C. Microstructure characterization was done by optical and scanning electron microscopy; the texture was analyzed by X-ray diffraction. Mechanical behavior was characterized through Vickers hardness measurements and three-point bend testing. From the three-point bend test yield strength, ultimate flexural strength and fracture energy were determined. Failure mechanisms were analyzed by examination of through fracture surfaces and crack paths on specimens following failure.

The results show that bulk polycrystalline tungsten can be processed to strain >4 at 320^{o}C by ECAE at slow strain rates. This processing with ECAE produced bulk material with a ductility of ~19% at room temperature, while increasing the strength and fracture energy far above those of the as received material.

Through comparisons of fracture energy results from fracture toughness data on single crystals, it was determined that room temperature ductility is due to the orientation of the {110} planes along the principal stress direction. Microstructure refinement and grain elongation produced by ECAE undoubtedly contribute to the

strength and improved fracture resistance. Severe plastic deformation processing also altered the mode of crack propagation from intergranular in the as received material from along subgrain boundaries to transgranular with increased grain boundary delamination.

This work shows that it is possible to plastically deform polycrystalline tungsten at relatively low temperatures to large amounts of strain, and that this processing beneficially affects the mechanical behavior by increasing the ductility, strength and fracture energy.

DEDICATION

For my parents

ACKNOWLEDGEMENTS

Thanks go to all my friends and colleagues at Texas A&M University, whose camaraderie was greatly appreciated. Others that made this work possible are Dr. David Foley and Dr. Shryeas Balachandra , my fellow group members and friends, whose input, guidance, and conversations made this work possible, thought provoking, and enjoyable. I would like to thank Robert Barber, whose expertise made the processing of the material used for this study possible. The efforts of Dr. Sarah Shaw are also greatly appreciated for her support and exceptional proof reading skills.

I also would like to thank my committee chair, Dr. Hartwig, and my committee members, Dr. Karaman, Dr. Lalk, and Dr. Naugle, for their guidance and support throughout the course of this research.

This work would not have been possible without the financial support of the SMART scholarship program, ARDEC, and SFI Inc.

NOMENCLATURE

AKS	Aluminum Potassium Silicon
AR	As Received
CI	Confidence Interval
DBTT	Ductile-to-Brittle Transition Temperature
DU	Depleted Uranium
ECAE	Equal Channel Angular Extrusion
ED	Extrusion Direction
El	Elongation
FD	Flow Direction
FE	Fracture Energy
HEBM	High Energy Ball Milling
HPT	High Pressure Torsion
KEP	Kinetic Energy Penetrator
LD	Longitudinal Direction
MA	Mechanical Alloying
MPa	Megapascal
SPD	Severe Plastic Deformation
UFS	Ultimate Flexural Strength
WHA	Tungsten Heavy Alloy
YS	Yield Strength

TABLE OF CONTENTS

Page

LIST OF FIGURES

Page

LIST OF TABLES

Page

CHAPTER I

INTRODUCTION

Tungsten has played a critical role in the advancement of civilization over the past century. The element has been used in light bulbs, cutting tools, radiation shielding, and x-ray tubes. Tungsten is a refractory metal, a group of elements in the periodic table (W, Nb, Ta, Mo, Re) known for high density, high melting temperature, high strength, and resistance to chemical attack. Of these metals, Tungsten has the highest melting temperature (3420^{o}C), density (19.25g×cm^{-3}), and has a Young's modulus of 400 GPa [1]. These exceptional material and environmental properties continue to make tungsten an essential metal for commercial, scientific, and industrial applications. Although tungsten's use in light bulbs is slowly being phased out and replaced by more energy efficient sources of illumination, new uses for this refractory metal continue to be investigated.

The high temperature strength, creep resistance, and low evaporation and erosion rates in harsh environments make tungsten a potential material for future fusion reactors [2]. For other applications, its high density is attractive. These applications include kinetic energy penetrators (KEP), which rely on mass and velocity to be effective. Depleted uranium (DU) is currently the best material for KEPs, but given the concerns regarding DU's lingering toxicity, tungsten may be a suitable replacement material [3-5]. However, the brittle low temperature failure and mushrooming impact behavior of tungsten and tungsten-based materials still pose a challenge for its KEP use.

The first major research efforts on tungsten occurred in the early 1900's to develop filaments for incandescent light bulbs. Tungsten rods were transformed into thin ductile wires that could be bent and spooled without failure through a process of working the metal while decreasing the temperature [6]. This was a great achievement that allowed for the development of robust light bulbs with greater life spans than previous bulbs. The source of this ductility was determined to be the long fibrous microstructure produced during this working process [7].

The cause of tungsten's lack of ductility has long been linked to impurities that migrate to grain boundaries critically weakening them and causing failure [8]. Fracture phenomena of tungsten have been studied extensively. In the 1990's, work by Reidle and Gumbsch established that (100) and (110) are the primary cleavage planes in tungsten single crystals. It was learned that the crack tips in these crystals are blunted by the nucleation and migration of dislocations away from the high stress field near the crack tip [9-11]. Low temperature testing revealed that plastic strain and the presence of dislocations increased fracture toughness. Further research on working of tungsten through severe plastic deformation (SPD) by both high-pressure torsion (HPT)[12-14] and equal channel angular extrusion (ECAE)[14-18], demonstrated that it was possible to improve the strength, increase the ductility, and lower the recrystallization and ductile-to-brittle transition temperatures of polycrystalline tungsten. The highest ductility observed using an SPD approach was achieved through a combination of ECAE at 1000^{o}C followed by lower temperature rolling. This produced a 100 μm thick tungsten specimen with 8% elongation at room temperature [19]. However, creating bulk pure

tungsten with significant ductility still remains a challenge. Because of this, other metals are often added to tungsten to produce alloys that have some of the desired mechanical properties of tungsten while retaining some ductility [1].

Tungsten-based materials are produced through two methods: doping and alloying. Doping is done through the addition of trace metals; potassium is most commonly used and is added during the powder reduction process. After tungsten powder has been consolidated and drawn into wire, the potassium present forms elongated bubbles that inhibit equiaxed grain growth, which is linked to brittle failure [20, 21]. This method is effective for improving the durability of tungsten wires. However, the formation of bubbles long enough to arrest grain growth is only observed after heavy working and thus is difficult to achieve in bulk material.

Alloying can be performed by creating either a solid solution or a two-phase alloy. In a solid solution alloys tungsten is combined with another refractory metal to form a single-phase material [22]. Of these, rhenium is most effective in increasing ductility, lowering the DBTT, and increasing the high temperature creep resistance[23-25]. Unfortunately, rhenium is approximately two orders of magnitude more expensive than tungsten so its use is not economically feasible for most applications.

Combining other metals with low tungsten miscibility produces two-phase alloys. These alloys, known as pseudo-alloys, have the structure of a metal matrix composite where the tungsten phase acts as the particle reinforcement. The material properties of these composites referred to as tungsten heavy alloy (WHA), are a compromise between the high density and strength of tungsten and the malleability of

the matrix material. Tungsten heavy alloys typically contain around 90% tungsten, with a matrix phase composed of ductile material. Metals with FCC-type lattice structure are popular for the matrix. Iron (Fe) and Nickel (Ni) alloys are frequently used, but Copper (Cu), is also common. These metals are added to tungsten either through a powder metallurgy process or by imbedding the tungsten phase with a melted matrix phase. The effects of tungsten concentration [26-28], matrix composition[29, 30], sintering conditions [31, 32], heat treatment [33], and working [34-37] have on the mechanical properties has been thoroughly investigated. It has been established that microstructure plays a critical role in the mechanical behavior and failure. This microstructure influence has also been studied by modeling the particle-matrix interactions and the effects of tungsten phase morphology [38, 39]. Typically, increasing the tungsten content and working improve the strength of WHAs at the cost of ductility.

Based on this research, some questions remain about the processing of these tungsten materials. A great deal of research has been performed on tungsten to improve the ductility and explain the mechanism for brittle failure. Past research with ECAE demonstrates that this process improves the mechanical behavior, and specifically ductility and strength. The processing temperature for much of this research was done at elevated temperatures near the recrystallization point of tungsten in the range of 1000-1200^{o}C. One outcome of this high-temperature processing is that the true limits of grain refinement have yet to be observed. Unfortunately past ECAE research on tungsten focused on routes intended to preserve the original dimensions of billets rather than creating microstructures associated with ductility [7].

As with pure tungsten, there is a dearth of research on the effects severe plastic deformation has on WHAs. Area reduction extrusion has also been evaluated, but processing for this was done at high temperatures and thus grain refinement was limited [40]. Furthermore, the effects of particle morphology and microstructure on the response of WHAs to extrusion remain unknown for large amounts of deformation, that is; they are not independent variables. These variables are difficult to separate, as elongation of the tungsten phase typically correlates with microstructural refinement. Evaluation of these variables independently could allow for improved understanding and further improvement of the mechanical properties and alter failure mechanisms of these alloys.

An opportunity exists to use ECAE to investigate the influence of grain refinement, morphology, and texture on the mechanical behavior of tungsten, specifically ductility and strength. Equal channel angular extrusion and slow extrusion rates make it possible to deform hard metals at temperatures much lower than previously studied. Using ECAE processing routes that produce elongated morphologies enables the effects of temperature, and strain on the ductility and strength of tungsten materials to be further investigated.

CHAPTER II

OBJECTIVE

The objective of this work is to investigate how equal channel angular extrusion can be used to processes commercially pure polycrystalline tungsten, and the effect of that processing on microstructure, texture and mechanical behavior specifically ductility and strength. Further more to establish the key microstructure features that enable improved mechanical behavior, be that strength, hardness, fracture energy, or ductility.

CHAPTER III

LITERATURE REVIEW

History

The history of tungsten begins 14 billions years ago in the powerful supernovas caused by the decay of stars into neutron stars. The shock wave produced by these supernovas subjects the outer star region to intense pressure and high temperatures, creating the right environment for proton and neutron absorption, transforming lighter elements, such as iron and nickel, into heavier ones. This matter then joined the rest of the material floating in space and some of it eventually combined to form our solar system.

The concentration of tungsten in the universe is approximately 1 part per billion [1] . However, on earth it can be found in concentrations much greater and as high as 1 or 2% in certain formations. The two main minerals containing tungsten are differentiated by the presence of calcium, manganese, and iron. Those containing manganese and iron are referred to as wolframite while those containing calcium are called scheelite.

Discovery

Tungsten containing minerals were first identified in the Middle Ages, by the producers of tin, due to the formation of foam during smelting, reducing tin production. It was because of this relationship to tin that the tungsten minerals were first named wolfsschaum or wolfram, which translates to wolf's foam or wolf's cream in German. In Germany wolfram remains the word for tungsten. The legacy of wolfram continues, as the letter W symbolizes tungsten in the periodic table of elements. The name tungsten first appears in 1757 in A.F. Cronstedt's description of the mineral later identified as scheelite. Cronstedt, a Swedish mineralogist, named the mineral tung(heavy) and sten(stone) because of its high density. In 1781, C. W. Scheele developed a process for extracting tungstic acid from this mineral, later to be named after him. By 1783, this tungstic acid $WO_3 \bullet H_20$ was used to produce the first tungsten metal by reduction with charcoal. [1]

Tungsten Filament

Before the 1900's most of the research using tungsten focused on its use as an alloying addition to steels for increasing strength and hardness. This changed with the invention of the light bulb. Edison original bulb used a carbon filament that was inefficient and had a short lifespan. A replacement material was needed. High melting temperature materials were sought as a replacement as they would increase the

luminosity and lifespan. Platinum, tantalum and many other metals were considered possible replacements before tungsten filaments were produced. Initially, combining powdered tungsten with organic binders produced tungsten filaments. The mixture was then "squirted" through dies to form a filament that was sintered through self-resistance in a reducing atmosphere. This process volatilized the organic material leaving behind a pure metal filament. These filaments were very brittle and many bulbs did not survive shipping. This problem would not be solved until the invention of ductile tungsten.

Tungsten Processing

The inventor of the ductile tungsten filament, William D. Coolidge, filed the patent for his work in 1908, and many of the steps he described are still used to this day to produce tungsten and other powder metallurgy products. The procedure involves three stages: consolidation, high temperature working, and low temperature working.

Consolidation

Tungsten powders are pressed into a solid commonly referred to as "green" compact. The compact is then pre-sintered in a hydrogen atmosphere at temperatures between 1200^{o}C-1300^{o}C. After this step the tungsten can be handled but is still fragile with up to 40% voids. The tungsten is then sintered through self resistance heating by passing electric current for 10-15 minutes, so that it reaches temperatures of 3200^{o}C [6,

7]. This step fully consolidates the tungsten rod improving the materials strength so that is can be processed further without fracture.

Hot Working

The main purpose of hot working tungsten is to eliminate any remaining porosity left after sintering [41]. It is done at very high temperatures, >1400^{o}C. The process of hot working is typically done through multiple swaging operations, decreasing the temperature with each step. Near the recrystallization temperature annealing at ~1000^{o}C, and recrystallization ~1400^{o}C are sometime done to soften the tungsten for further swaging.

Cold Working

Cold working is done below the tungsten recrystallization temperature, 1000-1400^{o}C. The purpose of cold working is to increase the strength and fracture toughness through grain size refinement, grain boundary elongation, and texture alignment [42]. To accomplish this without fracturing the tungsten, the temperature is slowly decreased as the amount of strain increases. The Coolidge method initially includes swaging the tungsten followed by area reduction extrusion and concluding with wire drawing. The amount of total strain and processing temperature used by Coolidge and other tungsten processing techniques including rolling, swaging, ECAE and HPT are depicted in Figure

1. In order to represent all data on the same relevant scale, published size reductions were converted into strain by the use of the relation:

Equation 1 $$\varepsilon = ln\left({d_o}/{d_f}\right)$$

where d_o and d_f correspond to original and final dimension of the work piece.

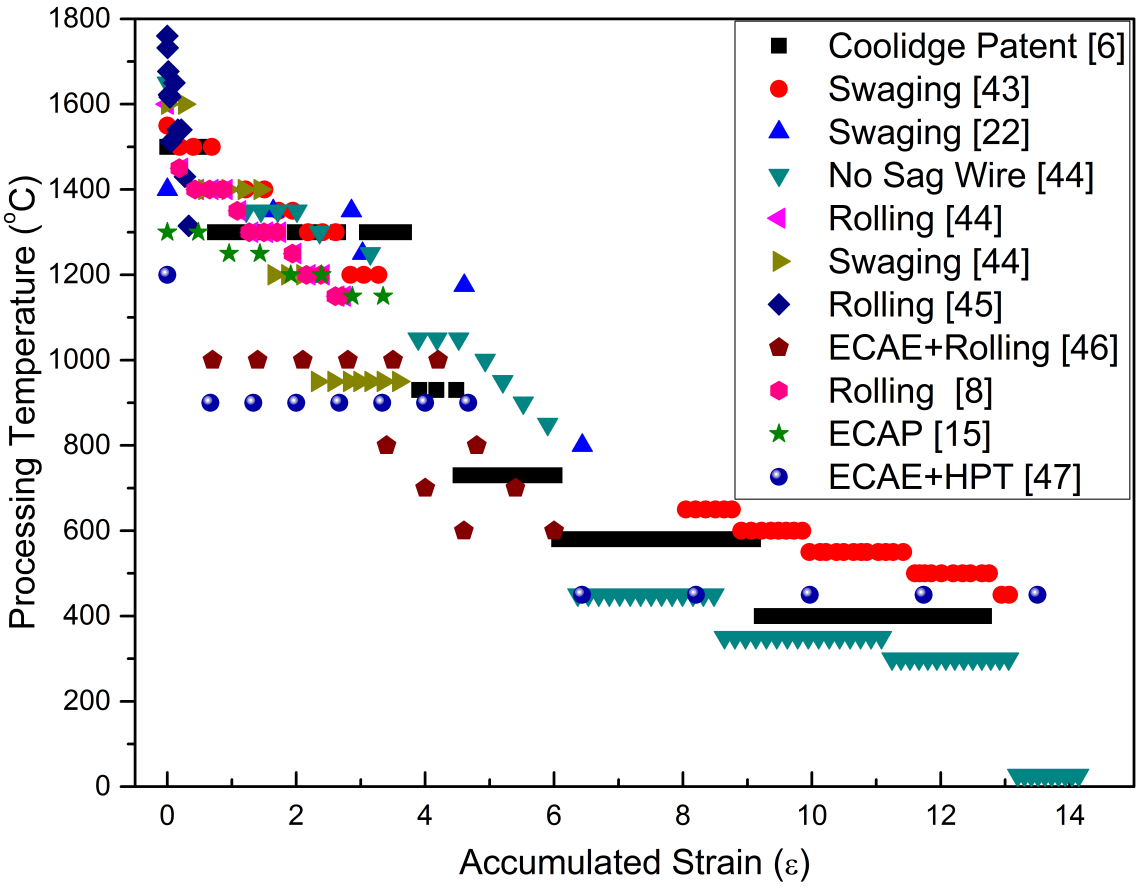

Figure 1. Collection of temperature and strain data for deformation processing of pure tungsten [6],[43],[22],[44],[45],[46],[8],[15], and [47].

Tungsten Properties

Tungsten is a transition refractory metal with a density of ~19.3g/cm^3, and melting temperature ~3420^{o}C. The atomic radius of tungsten is 137pm. Tungsten has an ionization energy of 7.98eV, and forms a stable BCC type crystal structure with a lattice parameter ~3.16**Å**. FCC and HCP configurations are also possible but are metastable and have only been observed in thin films. The Young's, Shear, and Bulk moduli of tungsten are *E*= 390-410 GPa, *G*=156-177 GPa, and *K*=305-310 GPa; the poisson's ratio *varies* between 0.280-0.30 depending on lattice orientation and measurement method. of Tungsten is also one of the most isotropic metals with an anisotropy coefficient of 1.01 at room temperature [1].

Temperature Dependence

The high melting temperature and strength of tungsten makes it a common material used in high temperature applications. It retains significant strength at temperatures above 900^{o}C [48]. However, above ~200^{o}C, tungsten readily oxidizes. It can only be used in a protective atmosphere at temperature ≥200^{o}C.

Several authors have investigated the effect of temperature on the mechanical behavior of tungsten. Much of the very high temperature research was conducted in the 1960's and 1970's on polycrystalline sheets and wires [8]. More recently, single crystal and polycrystalline bulk tungsten have also been examined. Results from these and other

investigations can be seen in Figure 2, Figure 3, and Figure 4. This collection of data shows that the yield strength and ultimate strength of tungsten varies depending on processing history and temperature. Worked tungsten retains significantly higher strength than single crystal or annealed material up to temperatures of 1000°C. Above these temperatures strength decreases rapidly as dislocations are eliminated and grain size increases.

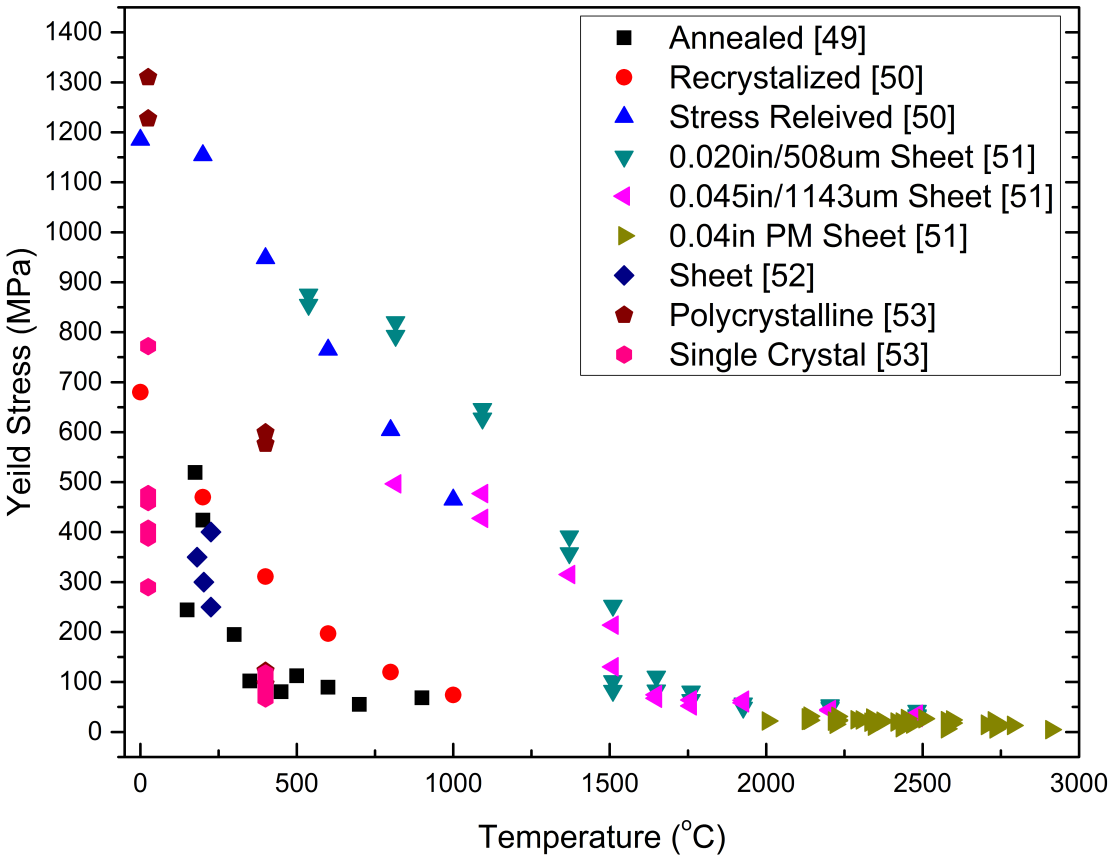

Figure 2. Yield stress of pure tungsten at temperatures from ambient to near 3000°C. Source [49],[50],[51],[52], and [53]

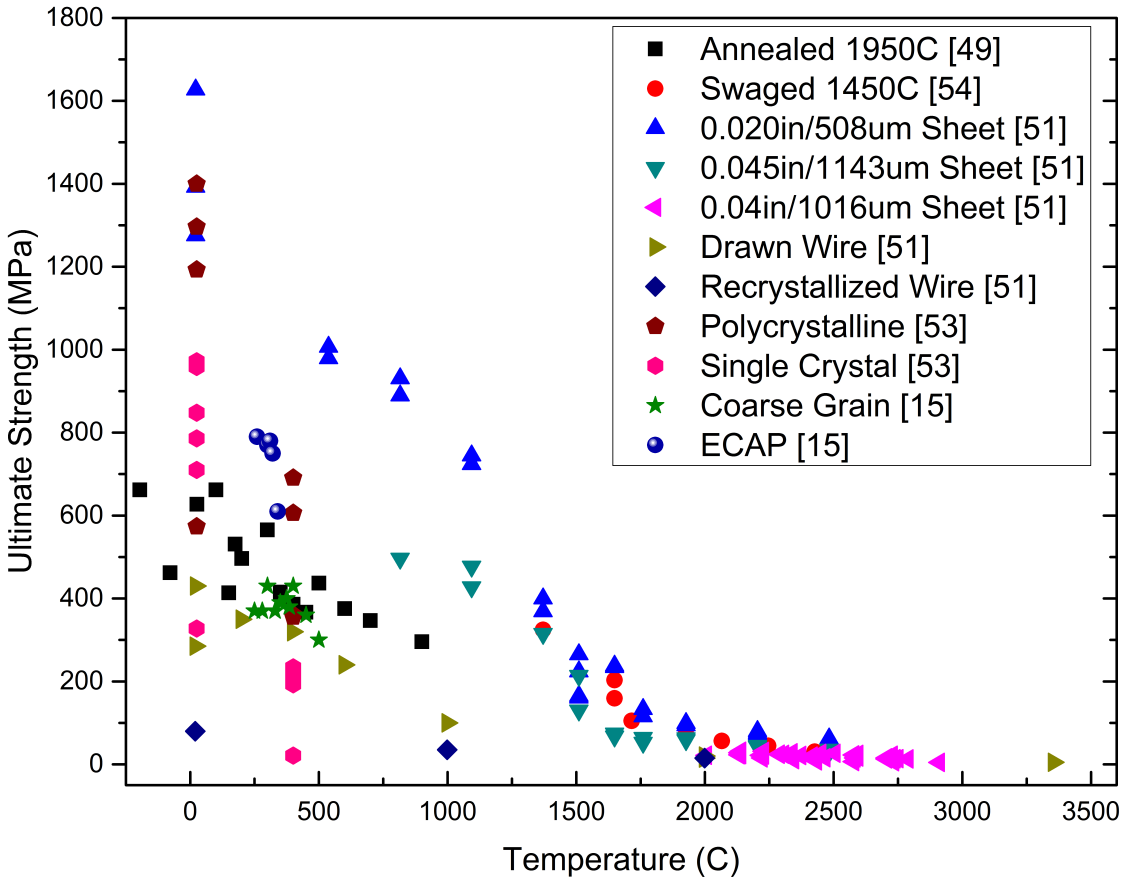

Figure 3. Ultimate strength of pure tungsten at temperatures from ambient to near the melting point. Source [49],[54],[51],[53], and [15]

The effect of temperature on ductility is illustrated in Figure 4 for several different tungsten products. Most of these results indicate that at room temperature there is little to no ductility and that only above 300°C does it begin to soften. This corresponds to the ductile to brittle transition (DBT), where the failure mode changes form transgranular cleavage to intergranular. Between 300°C and 1500°C there is a steady increase in the ductility, with a dramatic increase above 1500°C. This is the case for most tungsten products, however, a few exceptions exist. Heavily cold worked and

especially high purity tungsten have shown substantial ductility at temperatures below the normal polycrystalline material DBTT [15, 49]. Notable examples of this are heavily worked tungsten through processes of SPD that increase the strength to 4 GPa [13] in compression, and ~8% ductility [19], at room temperature in very thin sheet. For this test case, the processing imparting ductility included the reduction in cross section from approximately 1mm to 100 μm.

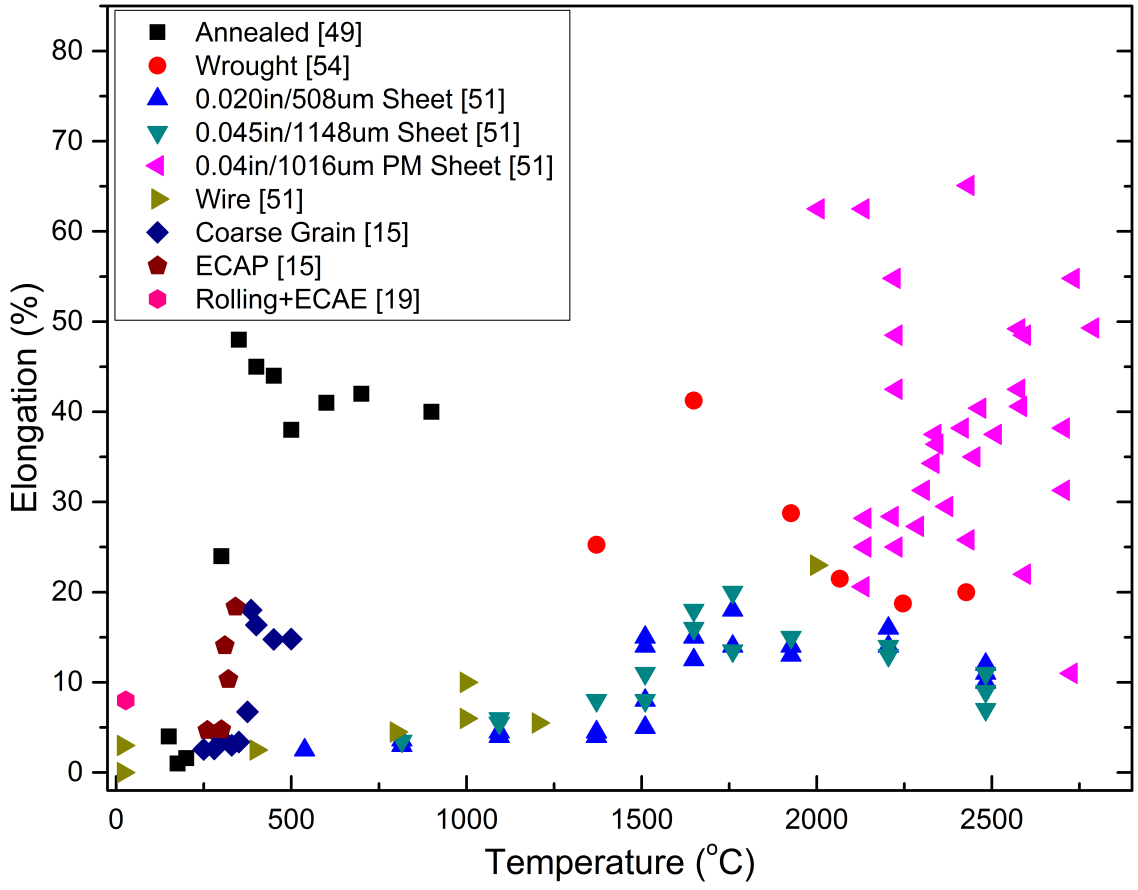

Figure 4. Elongation of pure polycrystalline tungsten at temperatures between 0°C and 2750°C. Source [49],[54],[51],[15], and [19]

Cold Work

Cold working is the most important processing stage for improving the mechanical properties of pure tungsten. The lower temperatures used in processing impart microstructural changes that are necessary for increasing the strength, and ductility. By using a temperature step down approach, as seen in Figure 1, the tungsten microstructure is elongated and refined. These gradual microstructure changes improve tungsten grain boundary cohesion, and lower the DBTT, by increasing the grain boundary area, generating dislocations, refining grains, and redistributing contaminates [55].

Conventional Processing

Fabrication of wires and sheets are the most common examples of cold working tungsten, and many investigations have found that by increasing the amount of work through cross section reduction, the strength and ductility also increase [6]. The results of some of these experiments are detailed in Figure 5. From these data it is important to note that irrespective of the processing method wire drawing, swaging, or rolling, strength follows a near linear trend with the log of material thickness, indicating a possible size effect to strengthening. If this were the case, it would imply that producing bulk tungsten with similar properties might be impossible.

A size effect can be evaluated by comparing recrystallized, and as worked tungsten wires. If strengthening were due to a size effect, a similar increase in strength would be anticipated for recrystallized tungsten. However this is not the case, and recrystallized tungsten wire shows no increase in strength with diameters smaller than 100μm. This further indicates that mechanical behavior is dominated by the several microstructure fractures and therefore it may be possible to produce bulk tungsten with greater ductility.

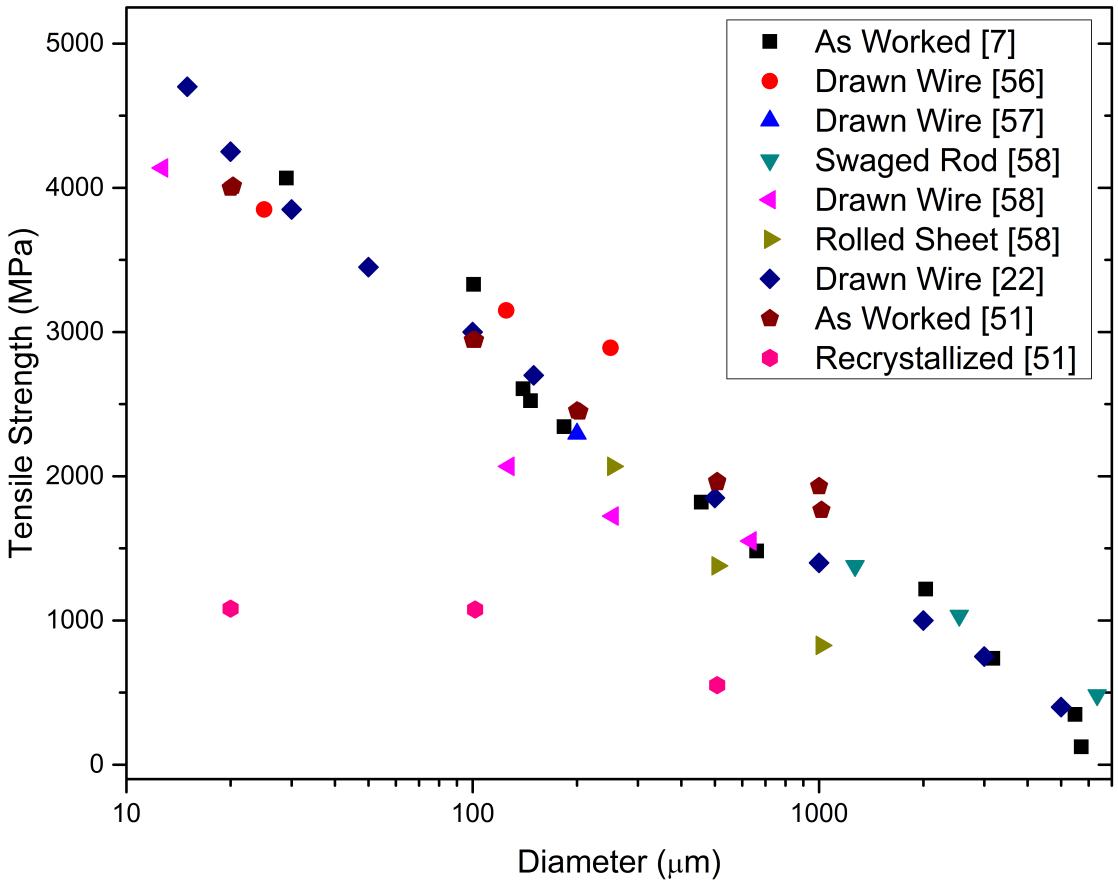

Figure 5. Tensile strength of tungsten wire with varying diameter. Source [7],[56],[57],[58],[22], and [51].

Severe Plastic Deformation Processing

Research into Severe Plastic Deformation (SPD) of tungsten has shown some promising results for enhancing strength and ductility. Using high pressure torsion (HPT), Q. Wei et al. were able to produce tungsten with sub 100nm sized grains with a flow stress of 3100MPa under loading rates of ~ $10^3 s^{-1}$. This was done by upsetting the tungsten to 30% strain at 600°C and then performing five full rotations of HPT at 500°C, producing an equivalent to a Von Mises strain of more than 90 at the disk edge [13].

Equal Channel Angular Extrusion (ECAE) has given results similar to HPT. S. Mathaudhu et.al. showed that the recrystallization temperature and grain size of tungsten decreased with an increase in number of extrusions and by decreasing the processing temperature [18]. Q. Wei and L.J. Kecskes we able to produce 100μm thick tungsten samples with nearly ~8% elongation at room temperature, by first processing with ECAE at 1000°C followed by rolling at 600°C [19]. Other notable findings from this work were that ductility increased by lowering the rolling temperature, and that subsequent rolling at a higher temperature eliminated an increase in ductility imparted at lower temperatures. This reaffirms the temperature step down approach used by Coolidge and indicates that mechanical behavior is highly dependent on the working temperature and the formation of a highly elongated microstructure.

The improved mechanical properties of severely deformed tungsten must be due to changes in microstructure that occur during cold working. In general, cold-working breaks down tungsten grains into smaller grains and sub grains, generates dislocations,

and may elongate original grain boundaries, depending on how strain is applied. Refining the grain size not only increases strength through the Hall-Petch effect, or grain boundary strengthening, but also increases the total grain boundary area. Because impurities are attracted to the grain boundaries, increasing the total area decreases the corresponding grain boundary concentration, and increases grain boundary strength. An increase in the number of dislocations increases strength by pinning and inhibiting dislocation motion, and increases fracture toughness through the blunting of cracks by providing sources for dislocation nucleation near the high stress field near the crack tip [59]. Dislocations and may also become sinks for interstitial atoms, trapping them within the crystal lattice, preventing them from migrating to the grain boundaries weakening them [1, 44]. These features result in increased grain boundary cohesion, and reduce the susceptibility for fracture through lower energy intergranular cleavage.

Severe Plastic Deformation

Severe plastic deformation (SPD) refers to a group of processing techniques where by material is heavily plastically deformed. These techniques are done to improve the mechanical behavior by producing fine microstructures with superior mechanical behavior [46]. Prominent examples of SPD are high-pressure torsion (HPT), equal channel angular extrusion (ECAE), and high-energy ball milling (HEBM) also known as mechanical alloying (MA).

Equal Channel Angular Extrusion

Equal channel angular extrusion (ECAE) was originally developed in the 1970's as a method of cold working that does not reduce the work piece cross section. Multiple manifestations of ECAE are possible including bar, plate, and continuous processing [60]. The unifying characteristic of ECAE is that the material is forced through a confined channel and "around" a corner. The sudden change in direction ("around" the corner) produces simple shear inside the work piece. Figure 6 illustrates the layout of a 90^o die angle ECAE tool. Interested readers should refer to the work of the inventor, V.M. Segal [61-63], for further details.

The amount of shear and the equivalent Von Mises strain are determined by the angle of extrusion, the number of passes, and the sharpness of the die angle [62]. Assuming little to no friction and a sharp angle tool design strain can be determined by the following equation:

Equation 2 $\varepsilon_t = 2N\frac{\cot\theta}{\sqrt{3}}$

Where N is the number of extrusions, and θ is half the die angle. Using this formula the equivalent Von Mises strains for a single 90^o and 120^o die angle extrusion are 1.15 and 0.68 [61]. As dimensions do not change during this process, ECAE is not limited by a cross section area reduction as other deformation processing methods often are. Additionally, rotation of the billet between extrusion steps allows for some control over

microstructure and texture through the application of different strain histories. Several different processing routes exist. A schematic of a traditional 90^{o} ECAE die, and processing schedule for different ECAE routes, are shown in Figure 6 and Table 1.

Table 1. Billet rotation for ECAE route A, B, C, Bc, and E.

ECAE Route	Rotation in Degrees After Extrusion			
	N=1	N=2	N=3	N=4
A	0	0	0	0
B	+90	-90	+90	-90
C	180	180	180	180
Bc	+90	+90	+90	+90
E	+180	+90	+180	+90

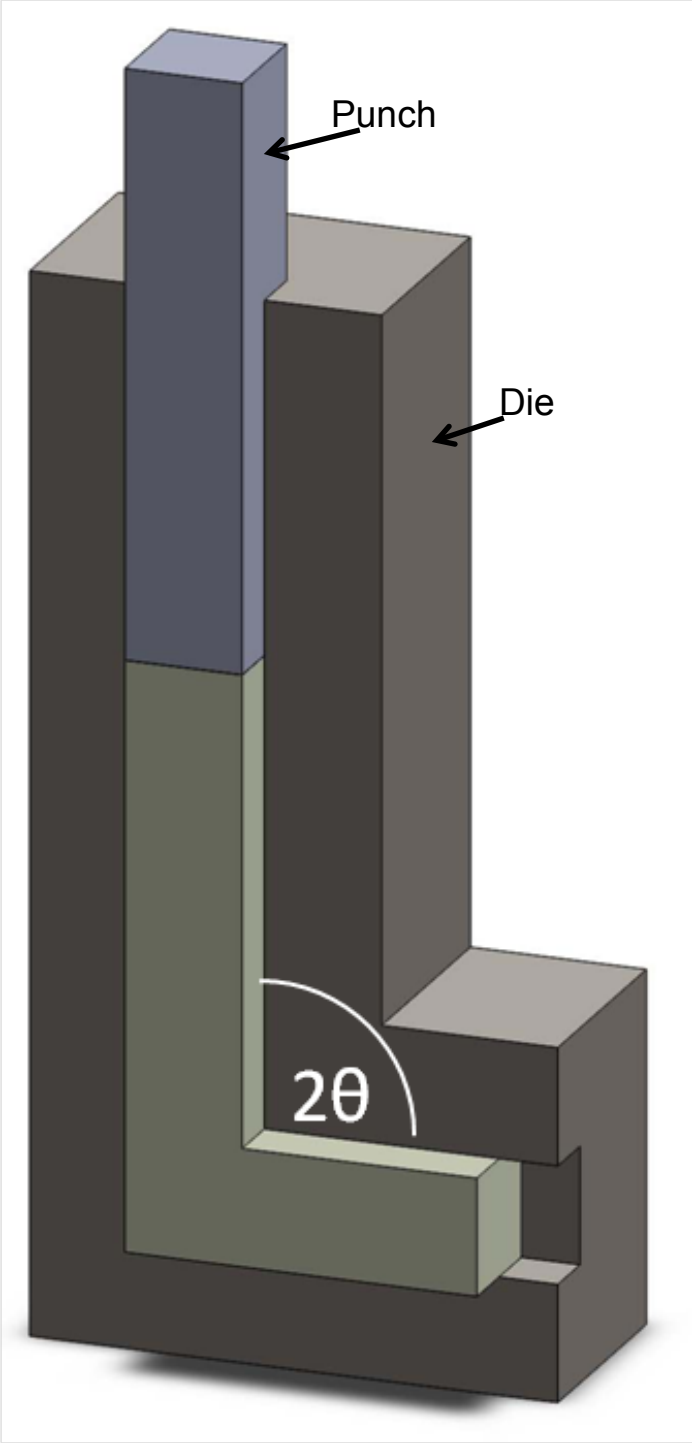

Figure 6. Illustration of classic 90^{o} die angle ECAE extrusion for a square cross section bar (billet).

High Pressure Torsion

High pressure torsion (HPT) was initially developed by P.W. Bridgman in 1946 [64], during his investigation into high pressure physics. It was not until the mid 1970's that research into using HPT as a method for processing metals was developed [13, 65-67]. As the name indicates, HPT involves pressing a sample, in the form of a small disk, between two anvils under very high pressure (several GPa is common). Rotating one of the anvils, produces working through simple shear. The high loads required limit the specimen size to small disks of material. Nominal dimension are roughly 10mm in diameter and 1mm thick.

Unlike other SPD methods such as ECAE, the amount of strain via HPT increases with distance from the center of the disk work piece, resulting in nonuniform stain, microstructure, and behavior [13]. Various equations have been used to determine the amount of strain in HPT [66, 68], based on different assumptions. A good approximation is, [68]

Equation 3 $$\boldsymbol{\varepsilon_t = ln\left(1 + \frac{2\pi Nr}{\sqrt{3}h}\right)}$$

Where *N* is the total number of rotations, *r* is the distance from the center and *h* is the sample height. For example, a disc measuring 1mm in height with a radius of 5mm would undergo a strain of ~3.62 at the disk edge per revolution. This estimation for the amount of strain can vary by as much as 20% depending on the assumptions used [66].

The main advantage of HPT is the ability to impart large amounts of strain without reducing the overall specimen size. This method produces very fine microstructures; with grain diameters of hundreds of nanometers in fully consolidated material. However, the small sample size limits the use of HPT. Samples are generally only large enough to perform material behavior characterization studies in compression, so evaluating the affect on ductility and tensile strength is difficult.

High Energy Ball Milling

High-energy ball milling (HEBM) is a processing technique where by powders are broken down and refined through collision and deformation. To do this, powdered powdered material is placed inside a hardened metal container with either hard metal or ceramic balls, sealed, and then spun, typically in a planetary motion. Rotating the container at high speeds causes the hardened balls, referred to as the grinding medium, to repeatedly collide with the metal powder. During these collisions the metal powder is heavily deformed, sometimes to the point that the particles break apart. These newly exposed metal surfaces can then be mechanically welded together through further collisions with the grinding medium. This process is referred to as mechanical milling (MM) or mechanical alloying (MA). The difference being that with MA different kinds of powders combines to then create a new homogenous alloy powder. Notably, it is possible to produce materials that are meta-stable, with compositions or structures that would not be possible to produce through more conventional other means [69]. Other

SPD techniques may be promising for the consolidation of these powders. However, their meta-stable nature makes them sensitive to temperature transformations [70-72]. This can be avoided if subsequent processing is done a sufficiently low temperature.

Processes of Severe Plastic Deformation

Refining the microstructure with SPD is accomplished first by the generation of many line defects. These defects accumulate eventually forming areas with high missorientation, Further increasing the number of dislocations causes these areas to form small subgrains within the original crystal. These subgrains begin with a low degree of missorentation but as the strain increases, the missorentation increases until high angle boundaries are formed. The processing temperature also influences the final grain size of SPD processed material. Numerous studies have shown that processing at lower temperatures produces finer grain sizes [60, 73-78]. This is due the thermal activation of dislocations. Lower temperatures limit the rate of dislocation motion and hence annihilation at grain boundaries and increases the numbers that pile up. New grain boundaries form as a result.

The grain size of tungsten processed by SPD at various temperatures is shown in Figure 7 and Figure 8.The methods of SPD are shown in both figures while Figure 8 also has data from more traditional processing methods, like rolling, swaging, and area reduction extrusion.

Temperature is not the only factor that determines grain size. The deformation method and total amount of strain also influence final grain size [73]. In general, HEBM produces the finest microstructures, followed by HPT and then ECAE. Even by the same methods, finer microstructures are produced with greater amounts of strain, as shown in Figure 7 for instances of multiple grain sizes at a given temperature.

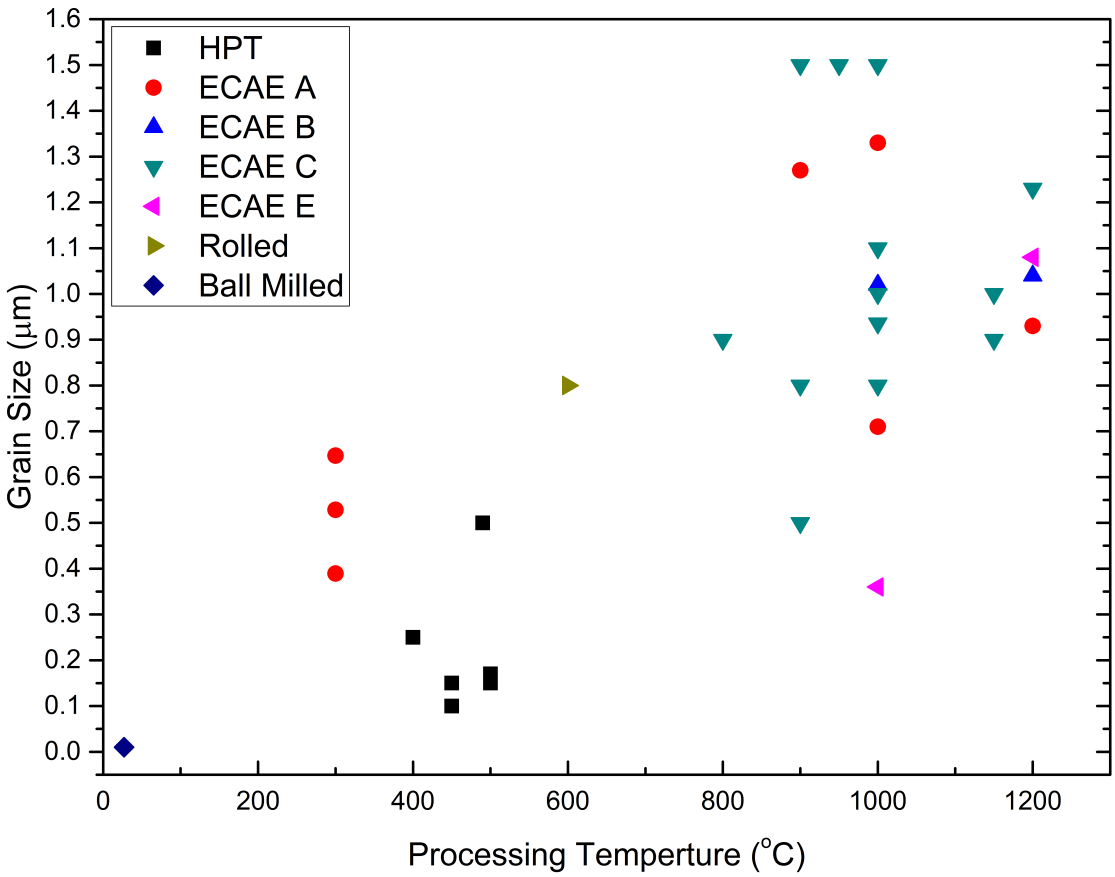

Figure 7. Grain size of tungsten processed by different severe plastic deformation methods at various temperatures.

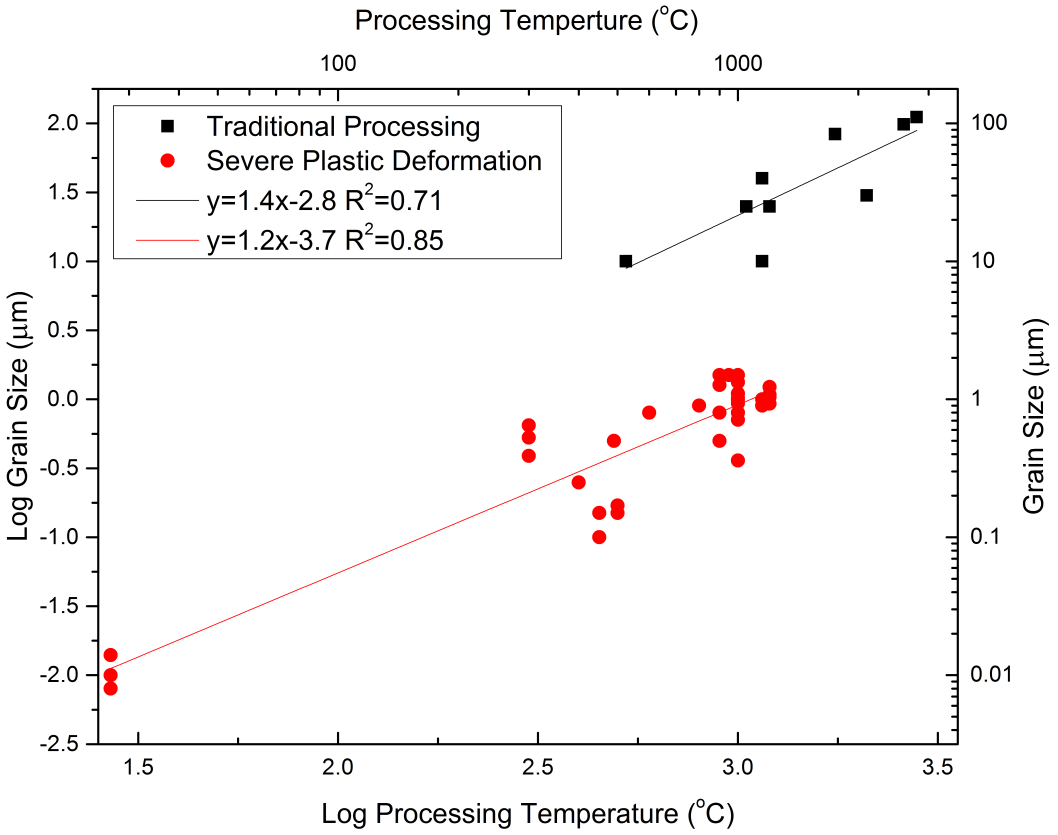

Figure 8. Log Log plot of tungsten grain size and processing temperature.

The differences in grain size, between SPD and traditional techniques, is most likely due to the fact that the goal of high temperature processing is different from that of low temperature processing. High temperature processing is typically done with the intent of eliminating porosity and reshaping the tungsten for further processing. Because of this it is often recrystallized between processing steps that would thus increase the grain size. Unfortunately, there is a lack of data available on the grain size and processing temperature and method of strain for commercially pure tungsten wires and sheet.

Tungsten Alloys

The exceptional properties of tungsten (high melting temperature, density, strength) combined with its poor workability (low ductility, brittle fracture) make tungsten alloys more useful than pure tungsten for many applications. These alloys fall into several categories: solid solution, precipitation hardening, dispersion strengthened, and heavy alloys. The later refers to a group of pseudoalloys composed of a nearly pure tungsten phase embedded in a ductile metal matrix.

Solid Solution Alloys

The solid solution alloys generally combine tungsten with other refractory metals including molybdenum, niobium, tantalum, and rhenium. Molybdenum and tungsten are completely miscible in any concentration because of the similar crystal structure and lattice size 3.1468Å (Mo) to 3.1585 Å (W), and only small differences in valence band structure [44] . The differences in lattice sizes for tantalum and niobium are much greater at 3.3026Å (Ta) and 3.3004Å (Nb) than that of tungsten, limiting solubility. Alloying with these elements improves high temperature strength and restricts grain growth. Alloys with tantalum and niobium have also been shown to increase the DBTT [44]. Scavenging elements included in very low quantities <<1% include: carbon, hafnium, titanium, and zirconium, have been shown to improve the ductility of binary and ternary alloys of tungsten with molybdenum, tantalum, and niobium [79].

Rhenium is by far the most important of these tungsten alloying elements, producing a material with greater ductility, workability, lower DBTT, and greater tensile and creep strength at high temperatures [1, 24, 44, 80-83]. The cause of this improved mechanical behavior is due to, the reduction in Peierls-Nabarro stress due to the alloys electronic configuration [80], the promotion of twinning as a mechanism of deformation [24], as well as increasing the solubility of the interstitial species, oxygen and carbon, that weaken grain boundaries [82]. The increase in solubility of interstitial species, especially near the limit of rhenium solubility ~27% [25], redistributes these element away from the grain boundaries and dislocations, promoting grain boundary cohesion [1]. These W-Re alloys are the most commercially important tungsten alloys, but their use is limited due to the high cost of rhenium which is approximately two orders of magnitude greater than that of tungsten [1].

The tungsten-based alloys are typically fabricated through a powder metallurgy process, because of the melting point of tungsten and other refractory elements. Pure powders are combined, either by mixing or ball milling and then pressed and sintered. The alloys can be formed by swaging, extrusion, and drawing similar to pure tungsten [1, 84, 85]. Tungsten rhenium alloys with up to 30% Re, have also been fabricated through chemical vapor deposition [86, 87], by co-depositing tungsten and rhenium in their hexafluoride form (WF_6 & ReF_6) in a hydrogen (H2) atmosphere[88].

Dispersion/Precipitation Alloys

The dispersion and precipitation hardened tungsten alloys are the most common commercial tungsten product. These materials are used for welding electrodes, light bulb filaments, and X-ray targets. Coolidge and fellow coworkers, while producing the first tungsten filaments, inadvertently created these alloys. It was noted by Coolidge that the type of crucible used for reducing tungsten oxide (WO_3) to pure tungsten powder impacted the performance of the final filaments [6]. Later, the source of the improvement was traced to trace amounts of alumina and silica that were picked up from the boats during the reduction process. Further work on these alloys lead to the addition of potassium oxide, to create non-sag or AKS (aluminum, silicon, potassium) tungsten [20, 89]. The addition of these elements alters grain growth at elevated temperatures, forming an elongated interlocking microstructure, instead of the typical bamboo type micro-structure. The interlocking structure improves filament longevity by preventing the sagging seen in pure tungsten filaments, caused by recrystallized grains slipping under their own weight [20, 21, 90, 91]. The enhanced structure is produced by the presence of potassium bubbles forming along grain boundaries. Alumina and silica's main contribution is that they increase the pickup of potassium oxide, and then are mostly removed during the sintering process, leaving 55-70% of the potassium remaining [44, 92].

Thoriated and zirconiated tungsten are two other examples of dispersion strengthened tungsten alloys. These materials have a higher strength than non-sag

tungsten but do not form the same interlocking microstructure and are primarily used in higher temperature applications [93, 94]. The addition of thorium to tungsten increases the electron yield of tungsten by 10,000 times at 1500K [95], and therefore thoriated tungsten is used when high electron emission is desired. These dopants are usually added during the reduction process [22, 44].

Tungsten Heavy Alloy (WHA)

Tungsten heavy alloys (WHAs) are a group of metal alloys used for their strength, density, and thermal stability. Creating a WHA requires the use of a powder metallurgy technique, such as sintering, due to the high melting temperature of tungsten (3422^{o}C). Common metals used for this alloying include iron, nickel, cobalt, and copper [96-98]. WHA microstructures normally consist of a nearly pure spherical tungsten phase, comprising more than 85% of the volume, surrounded by a ductile metal matrix [99-102]. This approach to alloying yields a composite two-phase material with some of tungsten's exceptional properties including high density and strength, with an improved ductility and workability. While these features are common in WHA, the manner in which the alloy is consolidated and subsequently processed greatly influences the final material properties.

Composition, heat treatment conditions, and strain all influence the properties of WHA. Work by Rabin [103], with tungsten-iron-nickel alloys demonstrated an increase in yield stress and a decrease in elongation with increasing tungsten content: (565MPa

and 36% El) at 88%W to (612MPa and 12% El) at 97%W. The tensile strength at 88% W is 907MPa and reaches a maximum of 986MPa at 93%W, then drops to 888MPa at 97%W in commercial alloys. Composition is not the only factor influencing mechanical properties. Increasing sintering time at 1480^{o}C of a 95%W alloy from 30 to 600 minutes reduced the yield stress from 602 to 558 MPa, and tensile strength from 917 to 835MPa, with little change in the elongation (18% el). Longer sintering times increase the tungsten particle size and weaken the final WHA composite.

The temperature of processing has a large influence on the microstructure and mechanical behavior of WHA. Research by several authors showed that increasing the sintering temperature from 1450 to 1550^{o}C decreases the yield and tensile strength while increasing ductility [103, 104]. Secondary thermal processing also alters the mechanical properties of worked of WHA. Figure 9 and Figure 10, show the tensile strength and elongation of several different WHA as a function of processing temperature. It can be seen that there is a moderate increase in strength and a modest decrease in elongation at temperatures around 500^{o}C. Multiple investigators have noted this. This property has been linked to an aging effect [105-107]. The trend reverses near the tungsten recrystallization temperature of ~1000^{o}C [99].

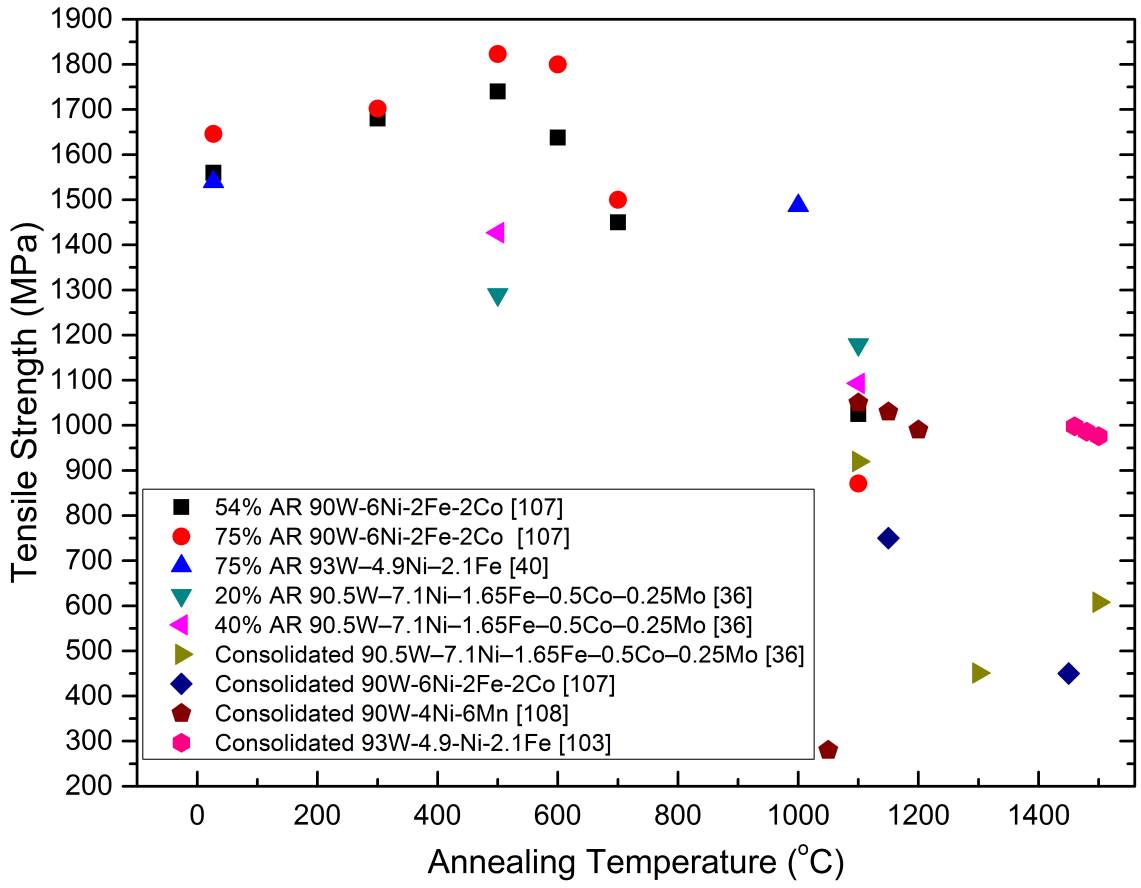

Figure 9. Tensile Strength (MPa) as a function of processing temperature for several WHAs with different composition and level of plastic strain. Source [107], [40] ,[36], [108], and [103]

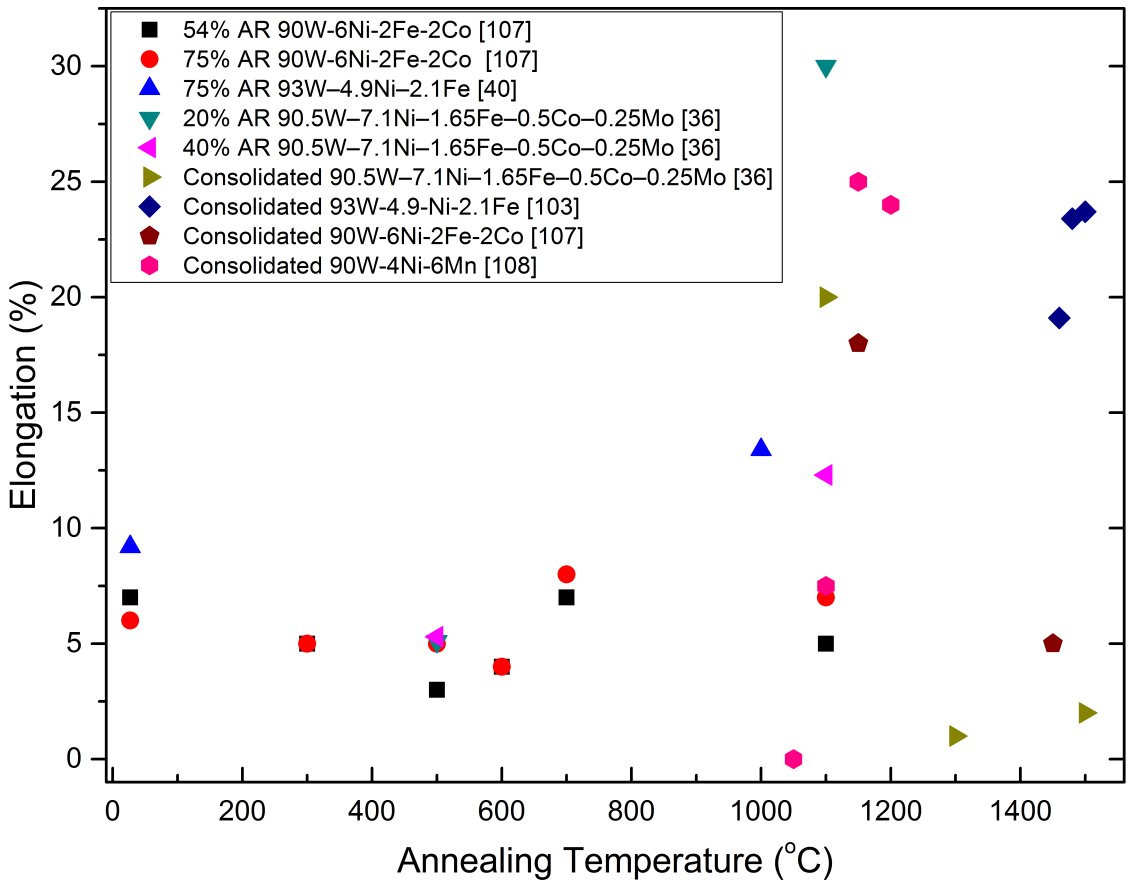

Figure 10. Elongation (El%) as a function of processing temperature for several WHAs with different composition and level of working. Sources [107], [40] ,[36], [103], and [108]

Working the WHA is another way to alter mechanical behavior. Working of tungsten heavy alloy has been shown to change the stress strain response, from dual slope, typical of metal matrix composites [109], to a single slope similar to a typical metal [36]. Examples of this difference in behavior are depicted in Figure 11 for WHA and tungsten in the as received and worked states. This behavior can be explained through hardening of both composite phases [110].

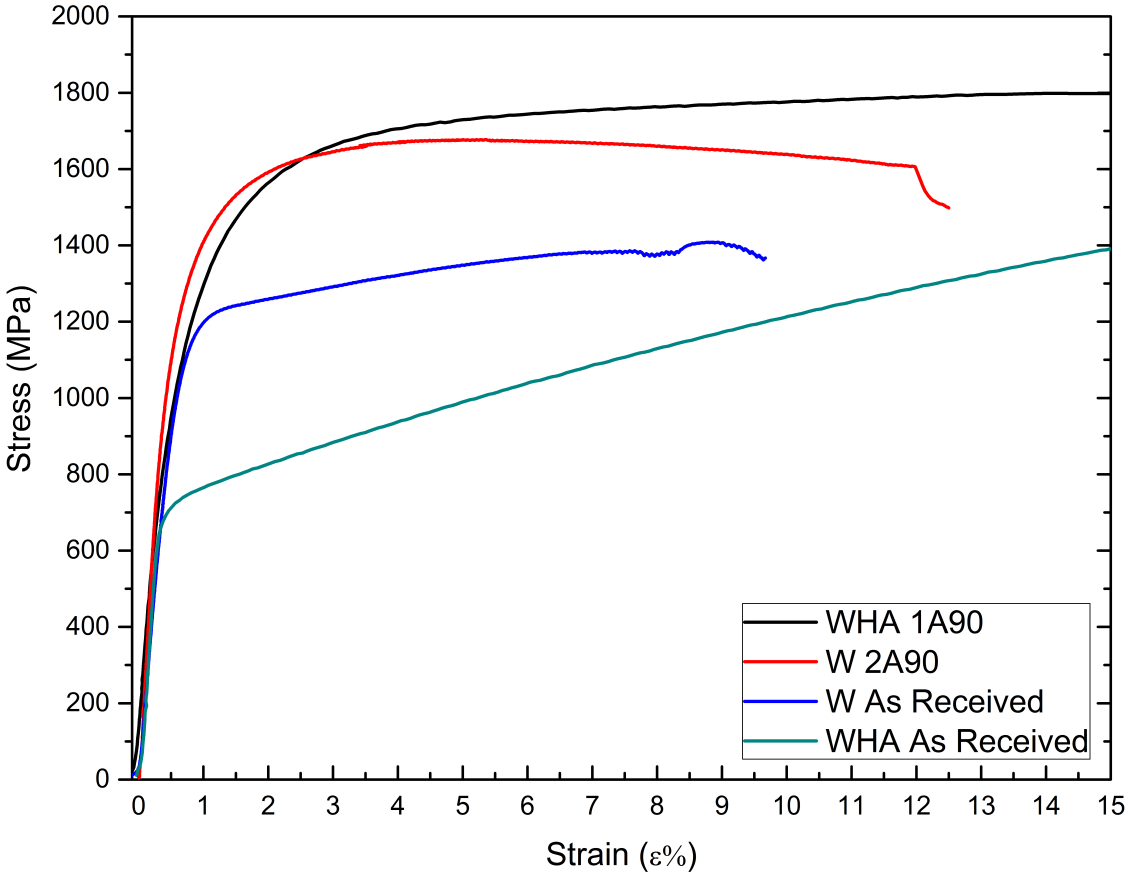

Figure 11. Stress-strain curves for tungsten and WHA in As received ECAE processed states.

Research by Srikanth and Upadhyaya demonstrated that cold working and annealing can increase the strength and ductility of WHA [111]. Swaged W-Fe-Ni alloys also have a decrease in work hardening, and an increase in strain rate sensitivity, approaching pure tungsten, as the composition approaches 97%W [112]. It could be expected that working could also impart anisotropy, possibly degrading performance, however, Rittel et al, demonstrated that 25% cold worked WHA rod, had little effect on the mechanical behavior and failure, when tested at 0^{o}, 45^{o}, and 90^{o} to the rod axis [113].

Working eliminates porosity, strain hardens the matrix and tungsten phases, and generally increases the tungsten particle matrix bond strength [114, 115]. Tensile strength and elongation data for multiple WHAs is presented in Figure 12 and Figure 13, illustrating the influence of working.

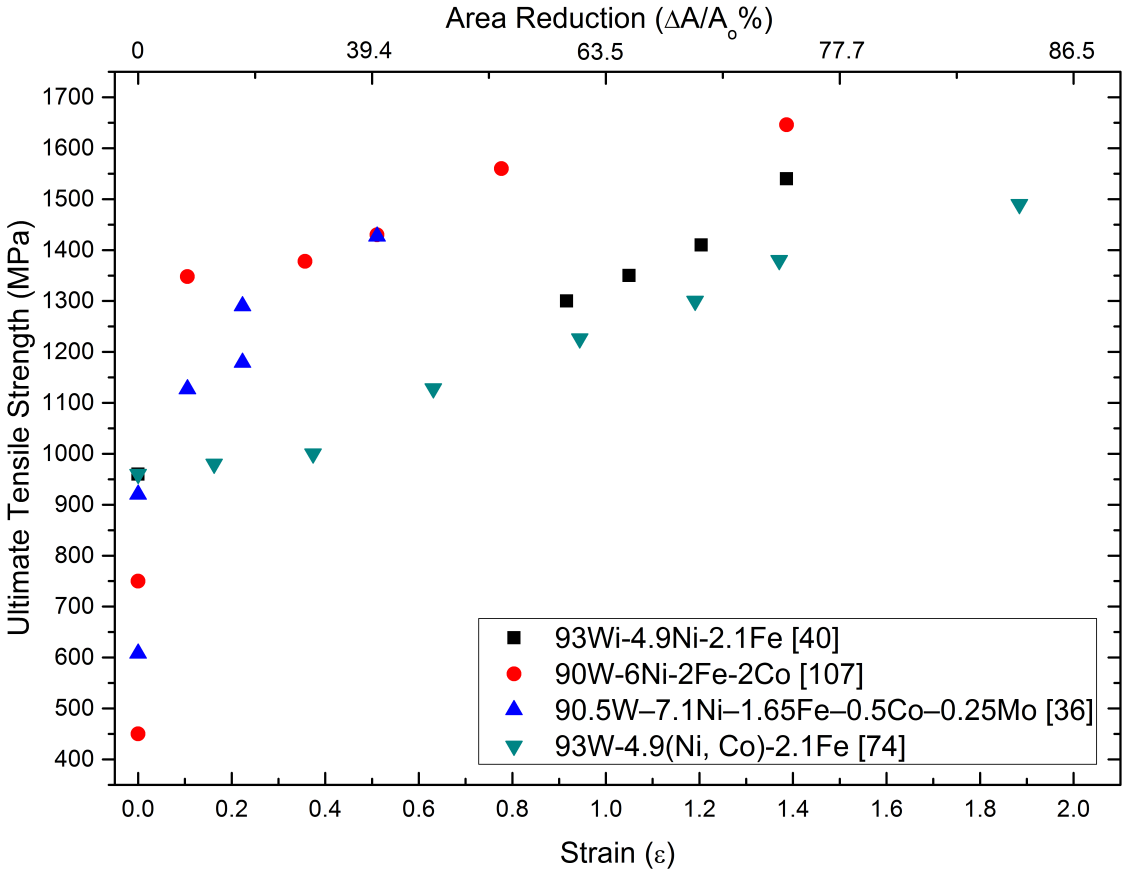

Figure 12. Ultimate Tensile Strength (MPa) for several as a function of accumulated strain by area reduction. Sources [40], [107], [36], and [74]

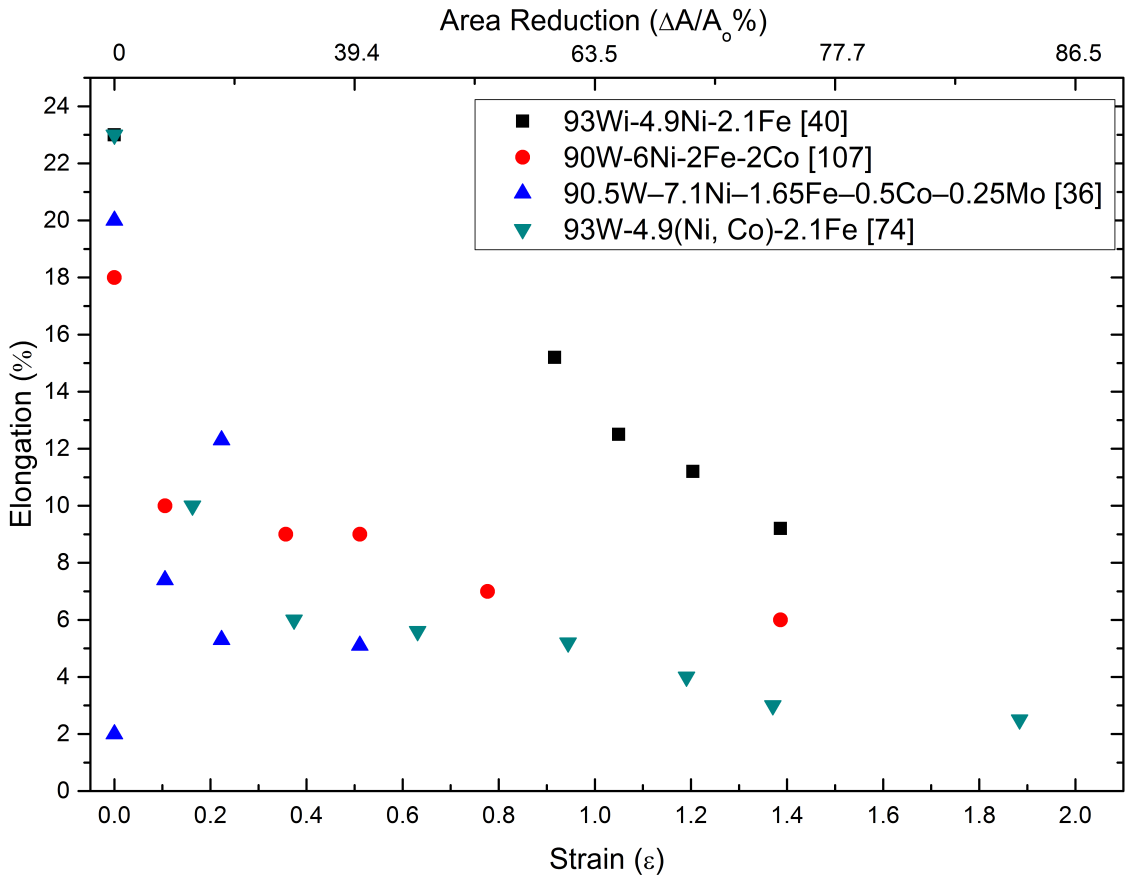

Figure 13. Elongation of different tungsten heavy alloys as a function of accumulated strain, by area reduction. Sources [40], [107], [36], and [74]

Failure in WHA

Post mortem analyses on WHA tension specimens indicates that failure generally starts at the point where two tungsten particles come into contact. Once formed, this crack propagates through the tungsten particle and into the matrix phase. The crack tip is then blunted as it propagates through the more ductile matrix. Once the strain capacity of the matrix is exhausted, debonding of the matrix and tungsten phases occurs followed by

failure [27]. Nucleation of these cracks occurs frequently, however only a few cracks will be able to propagate and cause failure [26].

Conversely, during compression, where debonding does not occur, failure is caused by cleavage fracture that begins at stress concentrations at defects within the tungsten grains. As this failure mode requires more energy, WHA's have greater strength in compression than in tension [116].

Modeling

Numerous researchers have investigated the thermo mechanical response of tungsten heavy alloys. They indicate that WHA undergoes some thermal softening in compression at high strain rate due to adiabatic heating through plastic deformation [36, 117, 118], as well as an increase in strength with strain rate [110]. Increasing temperature decreases flow stress and increases the ductility [117]. These trends are similar to that of pure tungsten [119]. The mechanical behavior and failure of WHA has been modeled in both compression [120, 121] and tension [118], using a variety of constitutive and finite element analyses [122]. These studies indicate that the tungsten particle size, shape, volume and contiguity (number of W-W contacts) influence the composites mechanical behavior. In general, increasing the amount of tungsten and tungsten contiguity increases the strength, and decreases the ductility. However, while the amount of work done on WHA is extensive, experimental and modeling investigations have primarily focused on nearly round tungsten particles produced

during the sintering process. Some work has also been done on more elongated tungsten particles but these are limited to aspect ratios (l/w) only as high 4 [34].

Deformation Mechanisms in Tungsten

Dislocation glide, twinning, and cleavage are all mechanisms for accommodating deformation in tungsten [123]. Slip is most likely to occur on the {011} or {122} planes along the close packed <111> direction [1]. Twinning does not readily occur but has been observed in tungsten of high purity along the {112} plane in the <111> direction [124]. Twins have also been observed in tension at low temperature and in material worked at temperatures below 1500^{o}C [125]. In polycrystalline tungsten, cleavage occurs readily in between and inside of tungsten grains [126].

Temperature has a critical effect on the deformation of tungsten. At temperatures below ~370K the nucleation of dislocations limits plastic deformation, while at higher temperatures their mobility is a controlling factor. Peter Gumbsch and others demonstrated this by comparing the fracture toughness of pristine and pre-deformed tungsten single crystals [10, 59]. At temperatures below 370K the pre-deformed tungsten showed higher fracture toughness than undeformed material. Above 370K this trend was reversed, leading to the conclusion of nucleation-controlled deformation below 370K, and mobility-controlled deformation above. This is due in part to the activation of new slip systems and a reduction in yield and critical resolved shear stress with increasing temperature. Results from investigations on tungsten single crystal, indicate that the

yield strength of the {001}, {011}, and {111} oriented on a single crystal all decrease with temperature, while the critical resolved shear stress of the {001} peaks at 200^{o}C [1, 127].

Tungsten Cleavage

The tendency for brittle fracture in tungsten is a major limitation of its wide spread use. The failure behavior of tungsten is typified by a brittle failure at low to moderate temperatures with a sudden increase in ductility over a narrow range of temperatures (200-300^{o}C) followed by ductile failure at higher temperatures. The sudden increase in ductility is referred to as the ductile to brittle transition [DBT]. The point where ductile failure occurs is referred to as ductile to brittle transition temperature [DBTT]. Measuring the property shift with temperature can be done through various methods, including microhardness [55], tensile testing [15], as well as 3-point [10, 11, 126, 128], and 4 point bend test [129]. Impurities with the exception of carbon and boron [130-132], surface condition [129], faster strain rates [59, 133], dislocation density [10], and polycrystals [126], increase the DBTT of tungsten, due to their effect on decreasing the mobility of dislocations and weakening the grain boundaries.

In tungsten single crystals cleavage most frequently occurs along (100) planes but can also fail on the (110) planes [134]. The preference of the (100) plane can be attributed to the low fracture energy along the low index crack systems (100)<011> and (100)<010>, as well as the greater number of orthogonal, propagation directions on the

(100) plane [11, 59]. In polycrystalline material fracture is predominated by transgranular cleavage with an increasing propensity for intergranular fracture at higher temperatures [50, 133].

Ductile to Brittle Transition

Mechanical failure in tungsten is one of the primary limitations to its more wide spread use. Because of this, the understanding how, why, and under what circumstances the failure mode changes is key to making greater utilization of tungsten possible. Tungsten like other BCC metals undergoes a transition from ductile-to-brittle failure with decreasing temperature. This change in failure mode is caused by differences in the interactions between dislocations and the propagation of cracks. At high temperatures, above the DBTT where failure is ductile, bulk deformation is accommodated by screw dislocations which have been calculated to have an activation energy of Qscrew~2eV [135]. At the DBTT where semi-brittle failure occurs, there is some crack tip plasticity, but the activation energy for this process determined by the shift in DBTT with strain rate has been calculated to be around Q_{DBT}=0.2eV [59].

These differences in activation energy from the screw dislocation and strain rate calculations seem to indicate that in the region of semi-brittle failure, screw dislocation are either being aided by the high stress field around the crack tip reducing the Peierls barrier for screw dislocation motion. Or a non-screw type dislocation causes crack tip blunting. This process has been modeled by several researchers concluding that non-

edge dislocations are responsible [59]. However, the defect/notch sensitivity of the DBTT suggests that the nucleation of dislocations is the limiting process. The process controlling the DBT and semi-brittle failure have been evaluated experimentally by the introduction of dislocations prior to fracture tests at temperatures between 77-600K [59]. Dislocations were generated through compression of tungsten single crystal with a {100}<010> crack system at 400^{o}C to 1% strain. At low temperatures 77-200K, the fracture toughness for the pre-deformed material is greater than the unworked material. Fracture toughness for pre-strained material increases less than the untreated samples at higher temperatures. The fracture toughness of unworked tungsten increases steadily above 200K reaching a sharp peak of K~27MPa×m$^{-½}$ at 370K. The fracture toughness of pre-deformed tungsten remains constant to 370K, and then reaches a peak of ~57K MPa×m$^{-½}$ at 470K. This indicates that at low temperatures, below 200K, dislocations improve toughness by acting as sources for nucleation for additional dislocations. While at higher temperatures they inhibit dislocation motion. This suggests that at low temperatures crack tip blunting is a dislocation nucleation controlled event while at higher temperatures >200K it is propagation controlled.

Brittle to ductile failure in polycrystalline tungsten differs slightly from that in single crystals, because of the powder metallurgy process used in their fabrication. Besides the presence of grain boundaries, polycrystalline tungsten has a greater dislocation density and a <110> texture aligned in the working direction [126, 128, 136]. These differences alter crack propagation and the DBT from single crystal material. Typically, polycrystalline tungsten fails along grain boundaries with some trans-granular

crack propagation as well [126, 128, 137]. At liquid nitrogen temperatures the fracture toughness of polycrystalline tungsten is higher than for single crystal tungsten. However this improvement disappears at room temperature. The greater toughness at cold temperatures is due to, strengthening from a smaller grain size, a higher dislocation density, and the imperfect alignment of the {001} and {011} planes. This makes crack propagation more difficult because cracks cannot continuously move along the lowest energy planes but instead have to transfer to higher ones before propagation can continue. Branching through grains at low temperature also consumes more energy for crack propagation than directly along the lattice [128].

The fracture toughness of polycrystalline tungsten is highly anisotropic. In fracture toughness tests of swaged polycrystalline tungsten rods, specimens taken orthogonally from the worked direction showed significantly less toughness, more inter-granular fracture, and a high DBTT than samples taken parallel to the sample length [126]. This behavior has been modeled to behave similar to a composite material with tough fibers along one direction that are bound by a brittle phase. These models predict that the mode of failure will change from brittle to ductile when the ratio between fracture energy for within a grain, R_{ig} (inter-granular) and around a grain, R_{tg} (trans-granular) is $\frac{R_{ig}}{R_{tg}} \leq 0.25$ [126]. This is in agreement with experimental results, indicating a change in failure mode at 200°C coinciding with when the ratio of , $\frac{R_{ig}}{R_{tg}} \leq 0.28$ [126].

These results result indicate that it may be possible to lower the DBTT of tungsten by increasing the amount of energy required for trans-granular fracture. With

lower DBT, it may be possible to improve the room temperature ductility of tungsten as well.

Role of Impurities

Contamination by interstitial species has been widely recognized as the primary source for embrittlement in polycrystalline tungsten. These elements namely, hydrogen, oxygen, nitrogen, carbon and silicon, have orders of magnitude difference in solubility at the eutectic temperature and room temperatures, 1000-100 μg/g vs <0.1μg/g [1]. On cooling the balance of interstitial impurities are forced to the grain boundaries exacerbating the already weak grain boundary adhesion. Joseph R. Stephens examined the effects of oxygen and carbon on the DBTT and strength of pure tungsten [130]. Figure 14 shows the results of the impact on oxygen and carbon concentration on the DBTT for poly and single crystal tungsten. At similar concentrations oxygen and carbon increased the DBTT of both polycrystalline and single crystal tungsten. The effects on strength were not as simple. Oxygen decreased the strength of polycrystalline tungsten with little effect on single crystal, and carbon increased the strength of both. It was concluded from these results that oxygen is the primary source for weakening of grain boundaries, while carbon acts as a source for dislocation pinning.

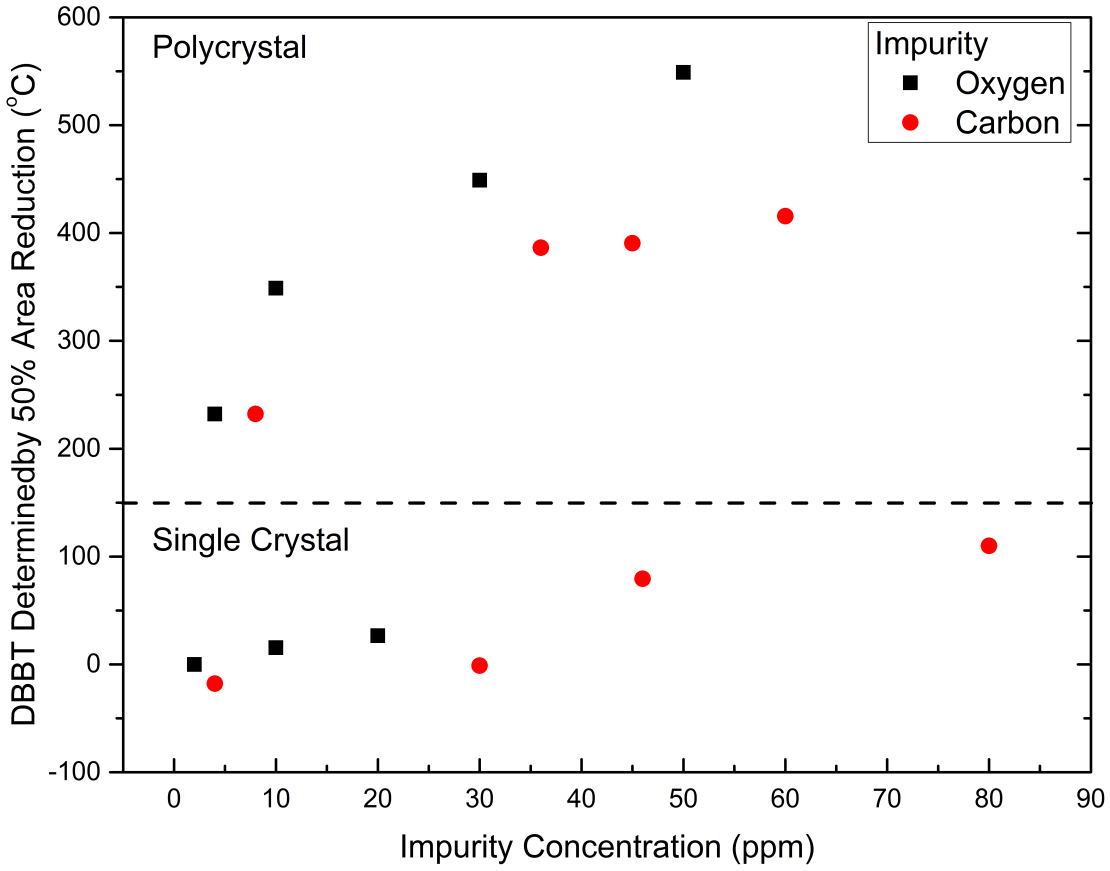

Figure 14. Ductile to brittle transition temperatures of polycrystalline and single crystal tungsten with concentrations of oxygen and carbon impurities ranging from 4-80 parts per million. Data from [130] .

Literature Review Summary

Investigation of the processing, mechanical behavior, and underlying physical phenomena in tungsten is a topic that has been thoroughly pursued since the turn of the 20^{th} century, attesting to its desirable mechanical properties. Much of this research has focused on processing, chemical composition, and alloying. The role of microstructure and texture has been one of the key areas of research into the development of tungsten. To date this research has been limited by the high temperatures needed to processes this material. However with techniques like equal channel angular extrusion, the previously established processing window can be broadened expanding the microstructures and mechanical behaviors available for investigation.

CHAPTER IV

MATERIALS AND METHODS

Materials

Wrought high purity 99.97% tungsten rods measuring 12mm in diameter were obtained from Plansee (Reutte, Austria) and used for this research project. The chemical composition, determined by the manufacturer, is replicated in Table 2:

Table 2. Chemical Composition of Commercial 99.97 Tungsten supplied by Plansee

W	**min**	**99.97%****						
Al	max.	15 µg/g	Cr	max.	20 µg/g	Cu	max.	10 µg/g
Fe	max.	30 µg/g	K	max.	10 µg/g	Ni	max.	20 µg/g
Si	max.	20 µg/g	Mo	max.	100 µg/g	C	max.	30 µg/g
H	max.	5 µg/g	N	max.	5 µg/g	O	max.	20 µg/g
Cd	max.	5 µg/g	Hg	max.	1 µg/g	Pb	max.	5 µg/g

Cr(Vi) +Organic impurities (e.g. PBB, PBDE, PFOS, PFOA)*

*The presence of Cr(VI) and organic impurities can be excluded definitely because of the production process (multiple heat treatment at temperatures above 1000^{o}C in H2-atmosphere

**Metallic purity without Mo

This material is polycrystalline and manufactured through powder metallurgy.

Procedures

Prior to SPD processing, the tungsten bar material was placed inside a square 25.4 mm, 304 stainless steel bar with a 12 mm diameter centered cavity, referred to as a can. These cans were flushed with argon to reduce oxygen contamination prior to

insertion of tungsten. After the tungsten was inserted, a 12 mm diameter 304 SS plug was placed in the cavity, behind the tungsten rod and welded into place. The can and plug dimensions were chosen so a minimum 25mm of stainless steel was adjacent to the tungsten rod on both ends.

Processing the tungsten was done with the use of a square work piece cross section 90^{o} die angle, sliding wall-type, ECAE tool. All extrusions were performed at $320^{o}C \pm 10^{o}C$ at extrusion speeds between less than 1.0 mm/s, with no rotation between extrusions (referred to as Route A). Between extrusion passes the billet was machined to allow for reinsertion into the ECAE tool. Lubrication was provided by anti-seize lubricant and by wrapping the steel billet with 0.025mm thick graphite sheet. After insertion into the die, the billet was allowed to reach thermal equilibrium with the heated tool for 1 hour prior to extrusion.

Sample Preparation

Following ECAE processing the tungsten rod was extracted from the SS can and sectioned into 2mmx14mm plates, along the flow plane of the extrusion, using electrical discharge machining (EDM). The EDM surface was then removed by mechanical polishing with silicon carbide polishing pads. These samples were then sectioned into 1mm thick specimens so that the final sample dimensions for bend testing was 1mmx2mmx14mm. The EDM surfaces from sectioning where all removed by

mechanical polishing. The sample surface was then electrolytically polished. Visualizing the grain boundaries for optical microscopy was done by electrolytic etching.

Microscopy

A FEI Quanta 600 FE-SEM scanning electron microscope (SEM) was used to evaluate the grain size and fracture surfaces of the tungsten specimens. Secondary and backscatter detection modes were used for this evaluation. Characterization of the grain width and average subgrain diameter were done on the flow plane with the use of Fiji software formally known as ImageJ. Grain widths were measured in several locations on optical micrographs of etched samples. Average subgrain diameters were determined by measuring the length and width of individual grains and then averaging those values together to get a value for grain diameter. All grain diameter values were used to determine the average grain diameter for each material. Measurements were taken at several locations at varying levels of magnification in order to fully characterize the material. This method is vulnerable to human error and bias necessitating measurement of numerous grains. However, as this process is time consuming and laborious, a compromise between these two must be made. For this reason the following criterion was used to characterize subgrain diameter. Subgrain measurements were made until the standard error was less than 5% of the arithmetic mean.

Equation 4 $\frac{\sigma}{\sqrt{n}} \leq 0.05 \times \mu$

Where *n* is the sample size, σ is the standard deviation, and μ is the arithmetic mean. This criteria is based solely on the authors experience.

As all samples were electro-polished prior to testing, it was possible to examine the deformed and fractured specimens after testing without further surface preparation. The crack deflection angle was determined by measuring the angle between the loading direction and crack surface. Figure 15 illustrates this crack deflection angle.

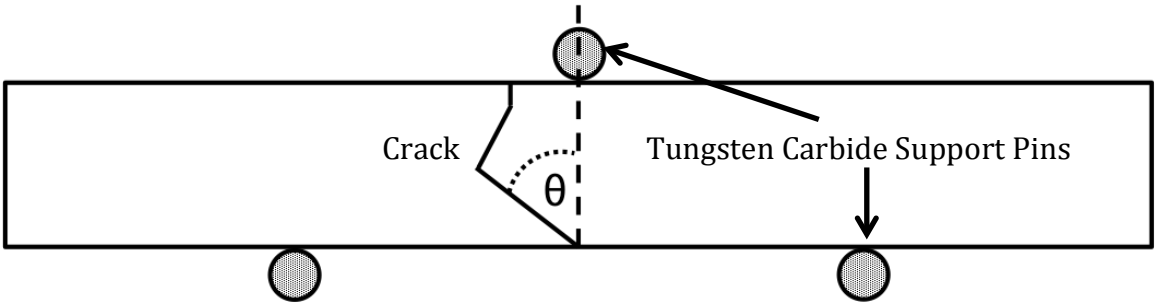

Figure 15. The crack deflection angle (θ) with respect to specimen orientation (side view).

Vickers Hardness

Vickers hardness measurements were made on the polished flow plane surface with a Leco Microhardness Tester LM300AT using a 300 g load. A total of 13 measurements were made on each sample. The highest and lowest values were disregarded and the remaining data were used to determine the mean and standard deviation.

The 3-Point Bend Test

Three-point bend tests were conducted with a custom-made test apparatus. The three-point bend apparatus was constructed from H13 tool steel; support pins were made from precision ground 0.20 mm diameter tungsten carbide (WC). The distance between, the supports was 7 mm. The sockets holding the WC rollers were coated with graphite before the rollers were attached. Rollers were held in place by nickel wire. The H13 tool steel, WC rollers and nickel wire were all chosen for their high-temperature properties, given that testing would be conducted at temperatures up to ~500^{o}C.

A three-zone, clamshell-type furnace was used to perform elevated temperature tests. An illustration of the furnace and apparatus arrangement is shown in Figure 16.

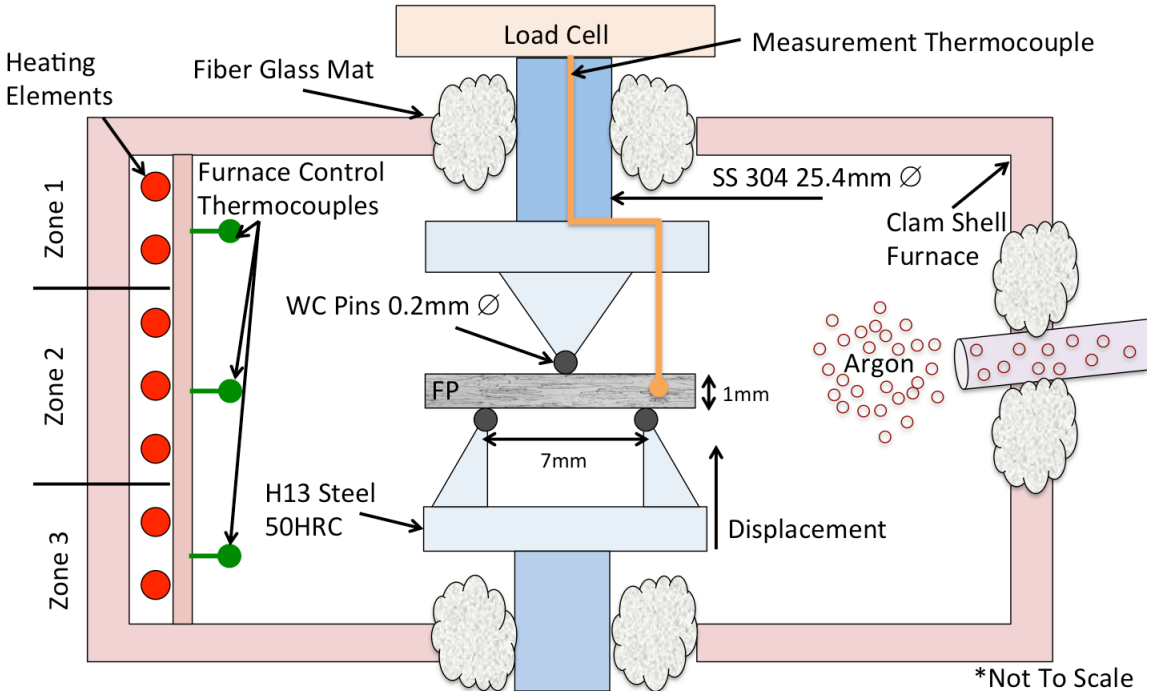

Figure 16. Illustration of elevated temperature 3-point bend test apparatus and furnace enclosure.

The specimen temperature was determined by the use of two K-type thermocouples. The chamber temperature was measured with a nickel-clad K-type thermocouple, threaded through the test apparatus with the end near the test specimen. A system calibration thermocouple wrapped in fiberglass insulation, was attached with nickel wire to the underside of a sacrificial test specimen, placed in the testing position, and held in place through slight contact with the three point bend apparatus. Temperature measurements of the specimen and chamber were made at several temperatures in order to establish a correlation. The furnace controllers were set at the desired temperature and then the furnace was allowed to reach equilibrium. Measurements of the chamber and specimen were made only after they reached a steady

state temperature, meaning values did not increase by more than 0.2°C over the course of several minutes. The thermocouple arrangement is shown in Figure 17. The correlation between the specimen temperature and the chamber temperature is shown in Figure 18.

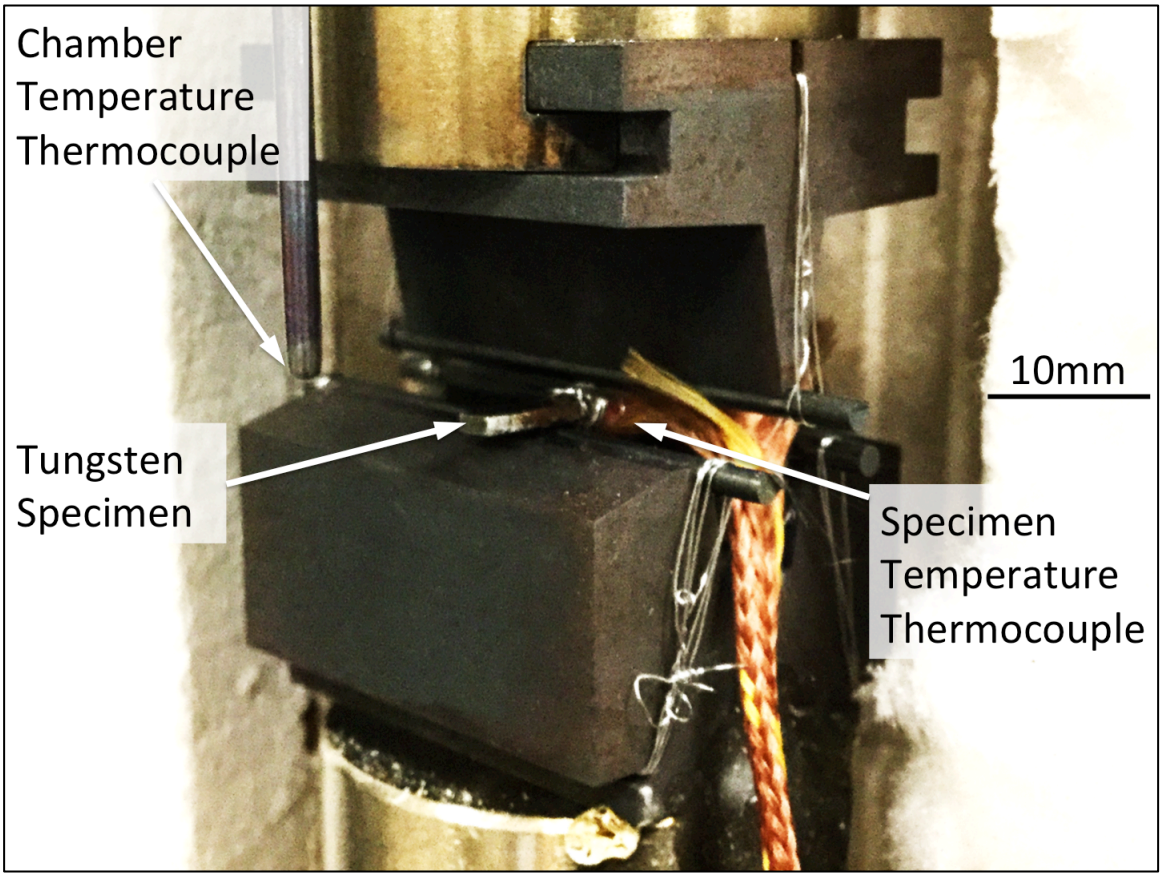

Figure 17. Photo of Three-point bend test apparatus with thermocouple arrangement used for furnace calibration.

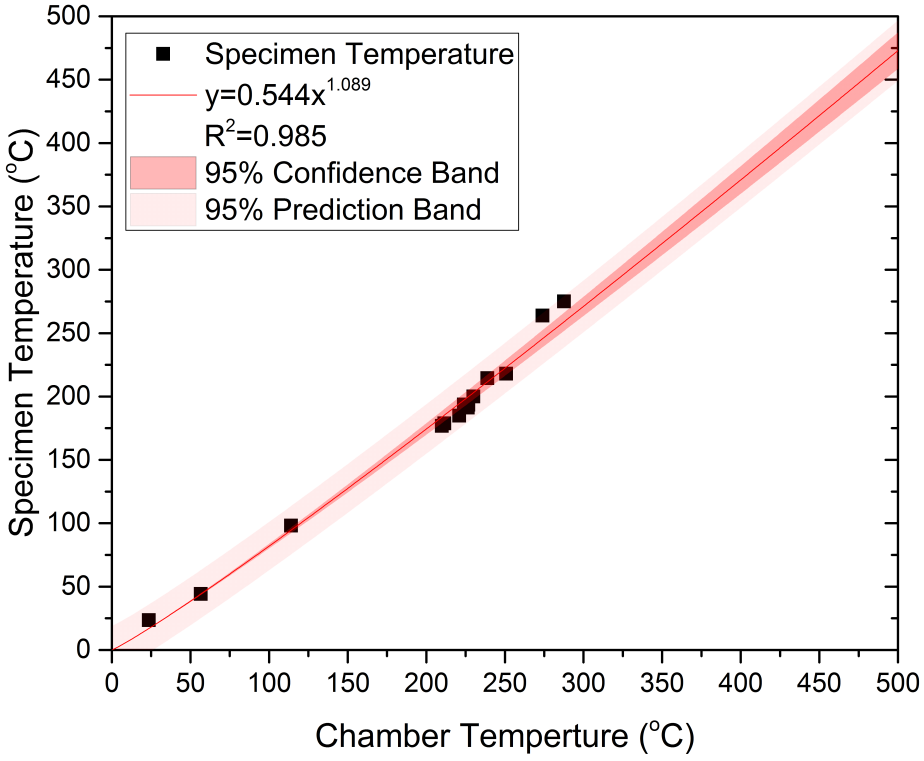

Figure 18. Specimen and chamber temperature data with exponential fit of data showing 95% confidence band and 95% perdition bands, indicating uncertainty in temperature calibration.

Prior to testing, specimens were placed inside the heated test frame, and the furnace controller temperature was allowed to reach equilibrium. The gaps around the furnace and test set-up were filled with fiberglass insulation. Argon was initially used for all elevated temperature tests. However, it was noted that at temperatures below 300°C there were no signs of oxidation, and the argon had little effect on the chamber and specimen temperatures, so the use of Ar was discontinued for lower temperatures tests. An inverted electronics was used to evaluate mechanical behavior at -45°C. This was

done as it required no alterations to the test apparatus and produced a stable temperature, due to the phase change of the refrigerant. Samples were tested at a cross head displacement rate of 0.01 mm/s with the longitudinal plane normal to the loading direction.

Determining stress and strain values were done through the load-displacement data and specimen dimensions using Equation 5 and Equation 6.

Equation 5 $\boldsymbol{\sigma_f = \frac{3FL}{2bd^2}}$

Equation 6 $\boldsymbol{\varepsilon_f = \frac{6Dd}{L}}$

Where σ_f is the flexural stress, ϵ_f is the flexural strain, F is the applied load, L is the span length, D is displacement, b is the sample width, and d is the sample depth.

The fracture energy (FE) was determined directly from the load and displacement data. Total energy was determined through Equation 7, by integrating the load displacement curve from initial to final displacement. The FE was calculated by normalizing the total energy by the cross sectional area of each specimen.

Equation 7 $\mathbf{Energy} = \boldsymbol{\int_{D_0}^{D_f} L(D)\, dD}$

Equation 8 $\mathbf{FE} = \boldsymbol{\frac{Energy}{b \times d}}$

Confirmation of the strain values calculated by the three-point bend Equations 2 and 3 was done by manually measuring the length along the upper and lower surfaces of several samples at several instances during testing. This was done by recording several

bend tests at room temperature, and then measuring the lengths manually at multiple times with ImageJ software. The upper and lower surface lengths were measured from end to end of the specimen as these points remained constant. Each total length measurement was then subtracted from the length of the undeformed regions determined in the image immediately prior to failure. These undeformed lengths were determined by measuring the linear region, with no curvature, at the ends of the specimen. It is assumed that the undeformed lengths are smallest at this moment. With this data the strain along the upper and lower surface was determined at each instance using Equation 9-12;

Equation 9 $\boldsymbol{l_{ud} = l_{Lf} + l_{Rf}}$

Equation 10 $\boldsymbol{l_i = l_t - l_{ud}}$

Equation 11 $\boldsymbol{l_0 = l_{t=0} - l_{ud}}$

Equation 12 $\boldsymbol{\Delta l_i = l_i - l_0 = l_t - l_{t=0} - 2l_{ud}}$

Equation 13 $\boldsymbol{\varepsilon_i = \frac{\Delta l_i}{l_0}}$

Where l_{ud} is the total undeformed length, l_{Rf} and l_{Lf} are the undeformed lengths on the left and right end of the specimen, l_t is the total length at each time t, l_i is the deformed length at $t=i$, l_0 is the initial length at $t=0$, Δl_i is the change in length, and ε_i is the strain at $t=i$. A diagram indicating the location of each measured length is shown in Figure 19.

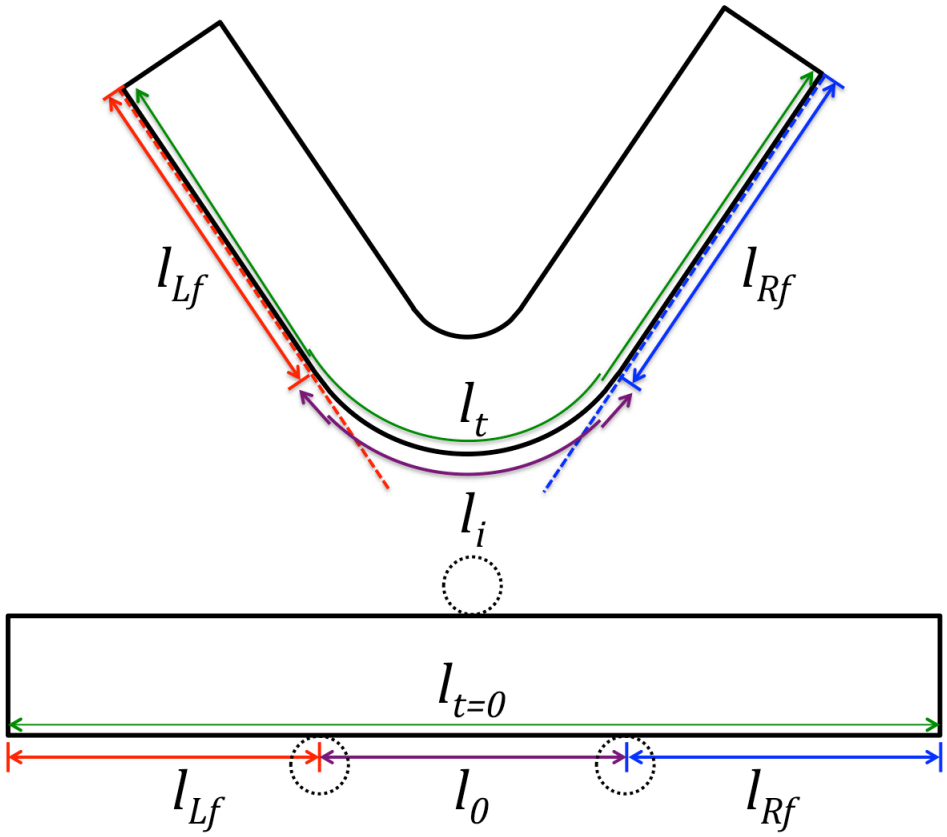

Figure 19. Illustration indicating the location of length measurements used to calculate strain.

Texture measurements were made with a Bruker XRD. Measurements were taken on the flow plane of each sample with the extrusion direction aligned with the x-axis, with a scan speed of 1 second and an increment change of 0.01°. The following peaks were measured to determine pole figures; {200}, {211}, {220} and {222}. The angles for each scan can be seen in Table 3. The raw texture data was analyzed using the PopLA texture software. Pole figures were generated using Matlab software package with the MTex 4.3.1 Toolbox. Only the {200}, {211} and {222} peaks were used to

analyze the AR and 1A material. The 2A and 4A materials were analyzed using these peaks as well as all 4 peaks collected. Only small variations were noticeable between these pole figures so those composed of all 4 peaks were used.

Table 3. Tungsten peak locations and 2θ locations used for texture analysis

Peak {ijk}	Location (2θ)		
	Center	Left	Right
{200}	58.253	57.751	58.342
{211}	73.204	72.904	73.942
{220}	86.946	86.692	87.655
{222}	115.086	113.607	115.206

CHAPTER V

RESULTS

Microstructure

Microstructures of as received (AR) and ECAE-processed tungsten samples used in this work are shown in Figure 20. Average grain width and average subgrain diameter are shown at each extrusion level in Figure 21 and histograms of the average subgrain diameter data are shown in Figure 22. The optical micrographs reveal the impact of ECAE on the tungsten microstructure morphology. With each ECAE pass the initial recrystallized grain boundaries are elongated. The SEM images reveal the differences in microstructure between the different levels of processing. The initial as received (AR) sub grains are nearly equiaxed and approximately 2.8 μm in diameter. During the first extrusion the average grain diameter decreases to 0.9 μm and these grains are contained within segmented bands. After two extrusions the grain size is ~0.73 μm and the grains appear more elongated with sharper edges. With further extrusions the rate of grain size refinement decreases; after four passes the subgrain size is approximately ~0.65 μm. The microstructure of 4A material also appears to have the most uniform microstructure with aligned/elongated grains.

The initial tungsten subgrains of the AR material, shown in Figure 20, appear to be consistent with a recrystallized microstructure. The aspect ratio of these grains is ~2, which may indicate some prior hot working. After the first extrusion the subgrain

microstructure becomes banded with each band broken into distinct subgrains with a average aspect ratio of ~3.6. With two extrusions that subgrains are further refined and the aspect ratio becomes ~3.1. The refinement of the 2A material does not appear to be as constant as the 1A material, as differing regions have slightly different microstructures and orientations. Evidence for this can be seen in the subgrain histogram of 2A material, which does not have the distinct peak in grain size as the other materials. After four extrusions the subgrains are highly refined, with the smallest aspect ratio of ~2.5. These grains also have a uniform orientation nearly aligned with the extrusion direction.

In optical micrographs seen in Figure 20, the original grain boundaries can be clearly seen. The average grain width and average subgrain diameter are shown in Figure 21, with errors bars indicating the standard deviation. In the AR material the grains are nearly equiaxed with an average grain width of ~22 μm. After the first extrusion the grain width decreases to ~15 μm, and the tungsten grains are now oriented at approximately 22.5^{o} from the extrusion direction. The aspect ratio increases by approximately 5 times that of the AR material. With a second extrusion the average grain width is ~8 μm, with ~13.3^{o} orientation from the extrusion direction, and an aspect ratio of approximately 17 times the AR material. With the fourth extrusion the average grain width is ~5 μm, the grains are oriented 7^{o} from the extrusion direction, and the aspect ratio has increased by approximately 65 times that of the AR material.

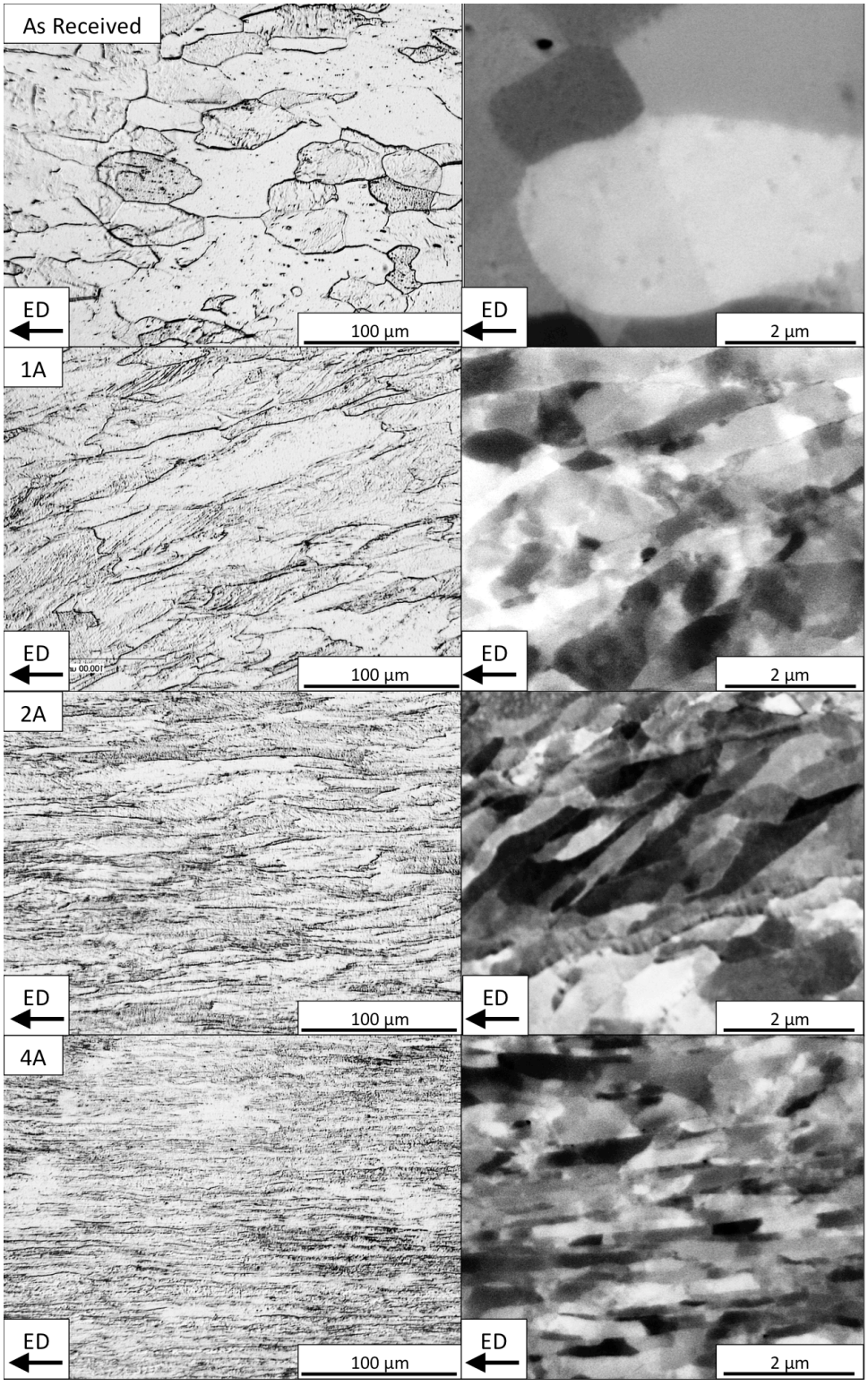

Figure 20. (Left) optical micrographs of as received (AR) and ECAE processed tungsten. (Right) SEM images using backscatter detector.

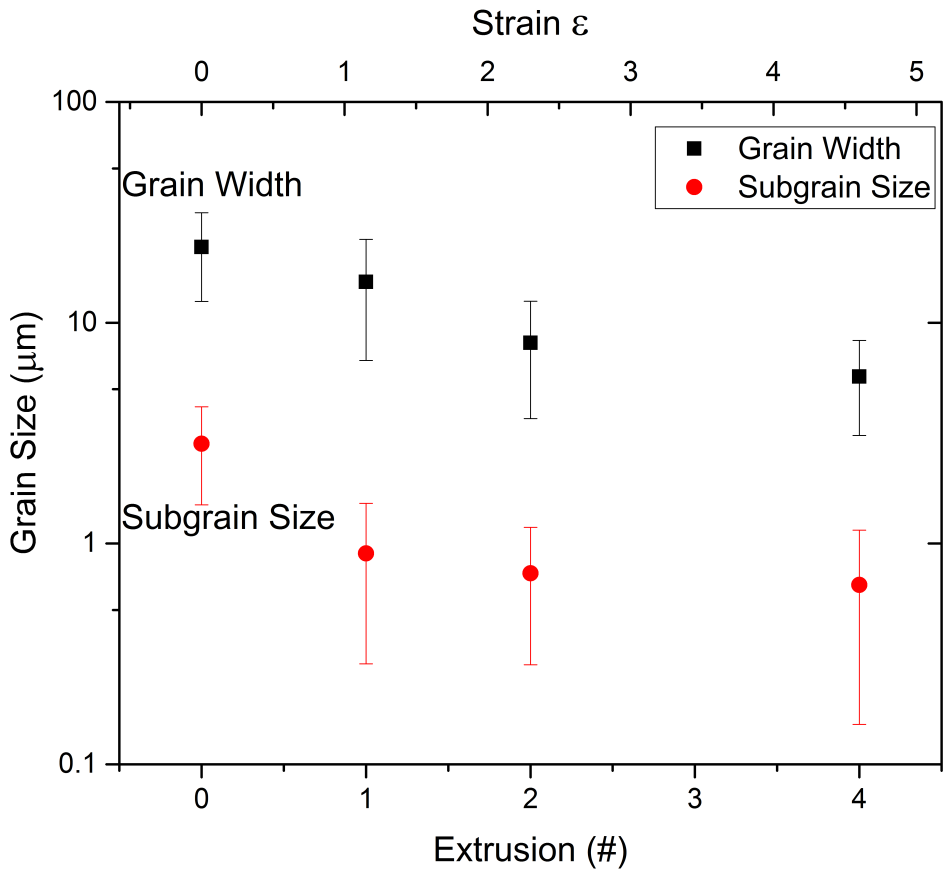

Figure 21. Width of recrystallized tungsten grains and average subgrain diameter of as received and ECAE processed tungsten. Error bars indicate standard deviation of mean.

The effects of grain size refinement can be seen in the subgrain histograms for each material in Figure 22, a minimum of 270 but as many as 500 separate grains were measured in order to estimate average subgrain diameter and produce these histograms. The curve fit overlaid on each histogram is a lognormal distribution, typically used for particle or powder size distributions. With the first extrusion not only is the average subgrain diameter reduced but the grain size distribution is also narrowed. A second extrusion further reduced the subgrain size but the non-uniform refinement noted previously in SEM micrographs is evident in the subgrain plateau between 0.2-0.8 μm. With four extrusions the grain size is further reduced and the size distribution is narrower. 2A material. The similar size distribution is due to the size plateau in the 2A material, as a larger number of grains are near the mean value were measured. The narrowing of grain size is evident by the decrease in width of the histograms around the mean; this is quantized by the 95% confidence interval (CI) above and below the mean value. Summarized results for grain width, average subgrain diameter, 95% confidence interval (CI) for average grain diameter, and subgrain aspect ratio are listed in Table 4.

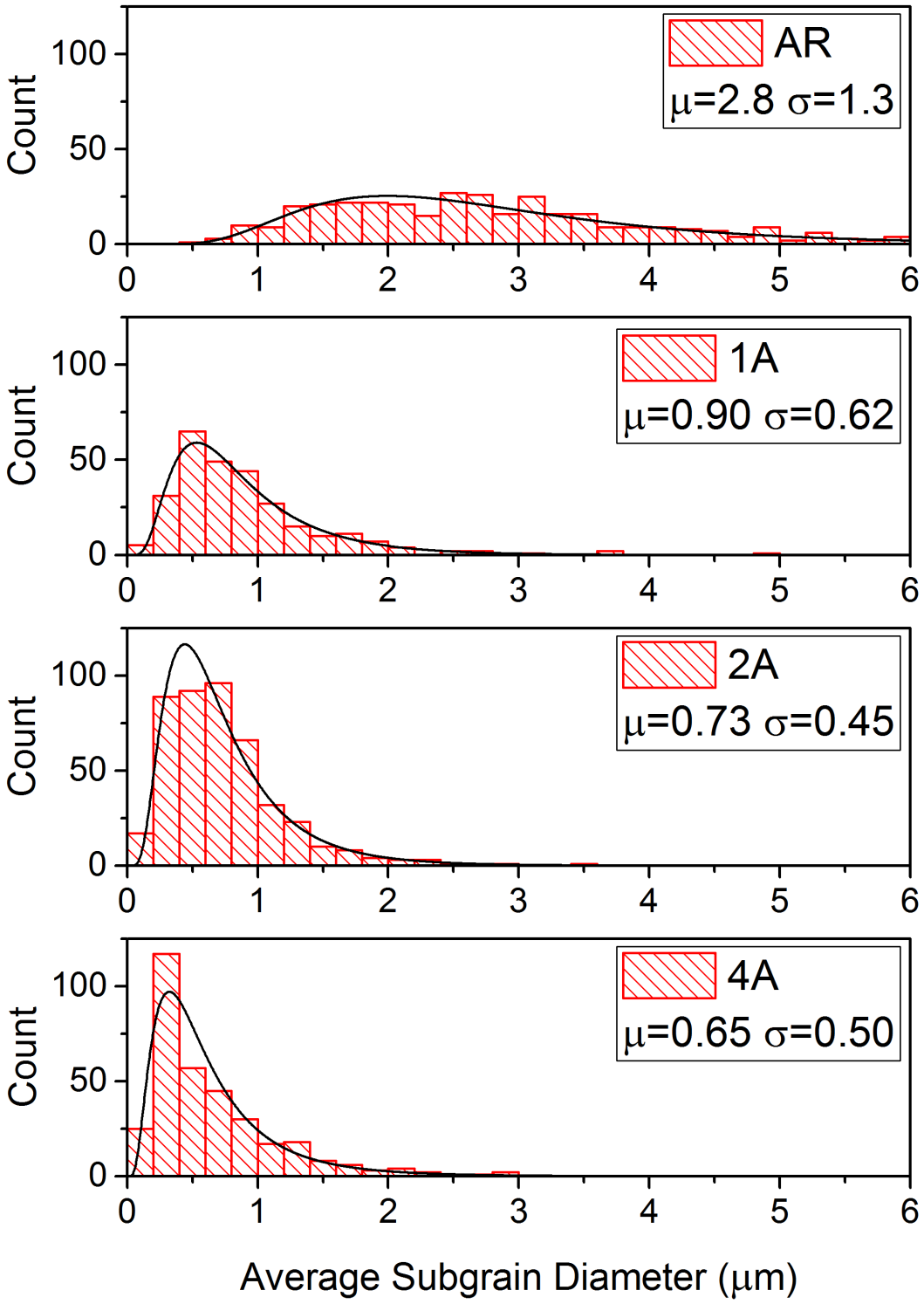

Figure 22. Histograms indicating grain size distribution with mean values and standard deviation indicated.

Table 4. Summary of microstructure results for as received and ECAE processed tungsten.

Processing	Strain	Grain Width (μm)	Subgrain Diameter (μm)	95% CI Subgrain Diameter (μm)	Subgrain Aspect Ratio (l/w)
AR	0	22±10	2.83±1.3	2.69-2.97	2.0±0.9
1A	1.15	15±9	0.90±0.6	0.83-0.98	3.6±2.1
2A	2.3	8±4	0.73±0.5	0.69-0.78	3.3±1.9
4A	4.6	5±3	0.65±0.5	0.60-0.70	2.5±1.4
Wire	---	5±3	1.9±1.4	---	4±2

Texture

Pole figures for the {100}, {110}, and {111} planes of tungsten materials are shown in Figure 23. The x y and z-axis correspond to the extrusion direction (ED), longitudinal direction (LD), and flow direction (FD) of ECAE processing. The AR material has strong {100} peaks along the x, y and z axis, while the {110} and {111} planes are distributed more uniformly but appear to have some preferential orientation around 45^{o} to the x and y axes. The 1A material has the weakest texture of all tested materials. The {100} planes have the strongest orientation along the y-axis, while the {110}, and {111} appear to be oriented in the z direction. The strongest {100} texture in the 2A material, is rotated ~16^{o} from x-axes, while the {110} texture has a similar rotation but from the y-axis, and {111} planes are rotated ~52^{o} from the y-axis. In the 4A material the {100} and {110} planes are well aligned with the x and y-axes, and the {111} planes appear to have three peak orientations. One of these is aligned along the y-axis and the other 2 are rotated ±34^{o} from the same.

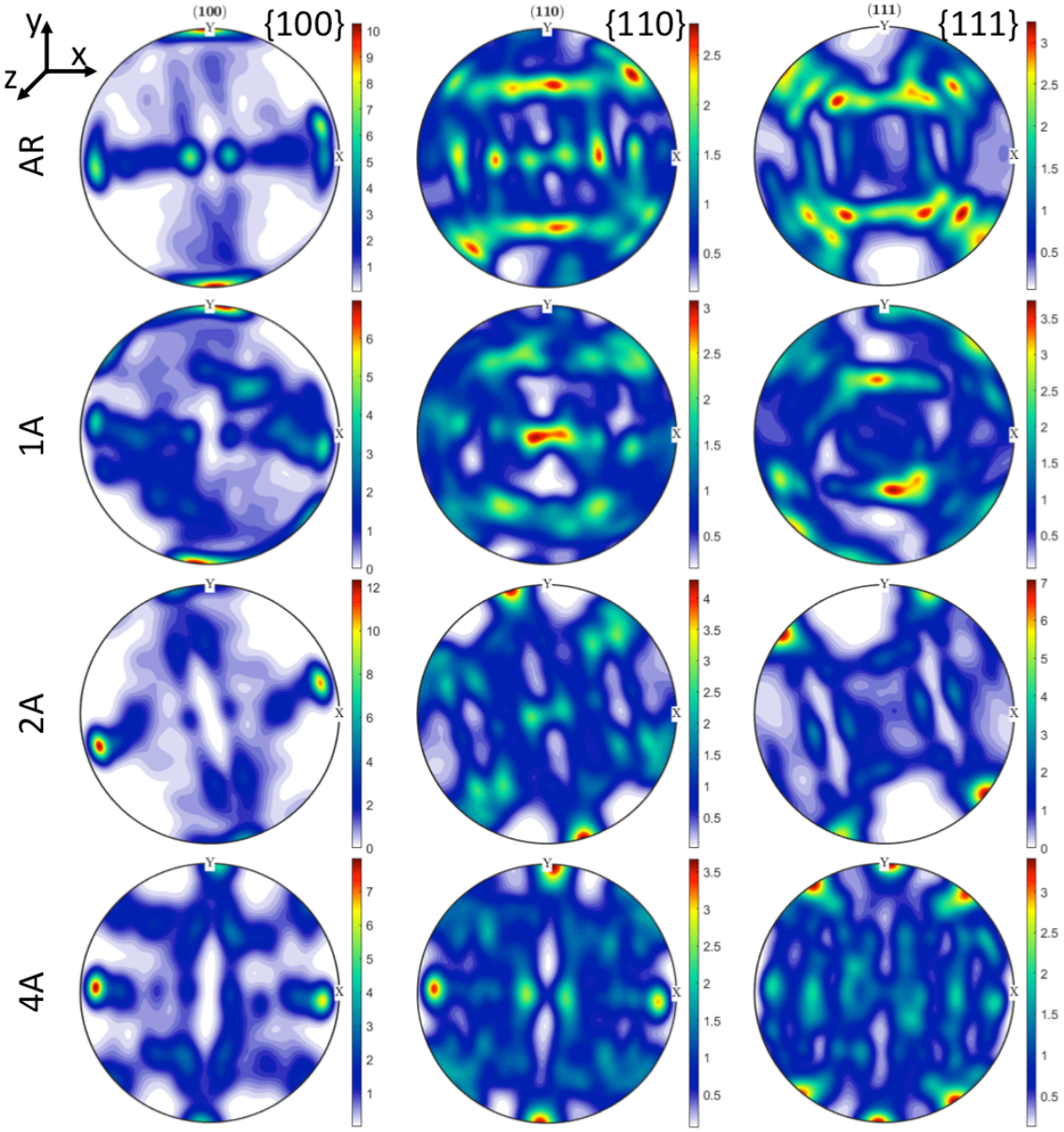

Figure 23. XRD pole figures for {100}, {110} and {111} planes measured on the flow plane of as received (AR) , and ECAE processed tungsten. X-axis oriented in the extrusion direction, y-axis longitudinal direction, z-axis flow direction.

Mechanical Behavior

Vickers hardness results along with grain size measurements are summarized in Figure 24. The Vickers hardness of the AR starting material is ~425HV. With each extrusion the hardness increases: after 1 pass 525 HV; after 2 passes, 570 HV; with 4 passes ~620 HV. Error bars for both set of data indicate standard deviation of mean values. Values in black represent Vickers hardness and subgrain size in black.

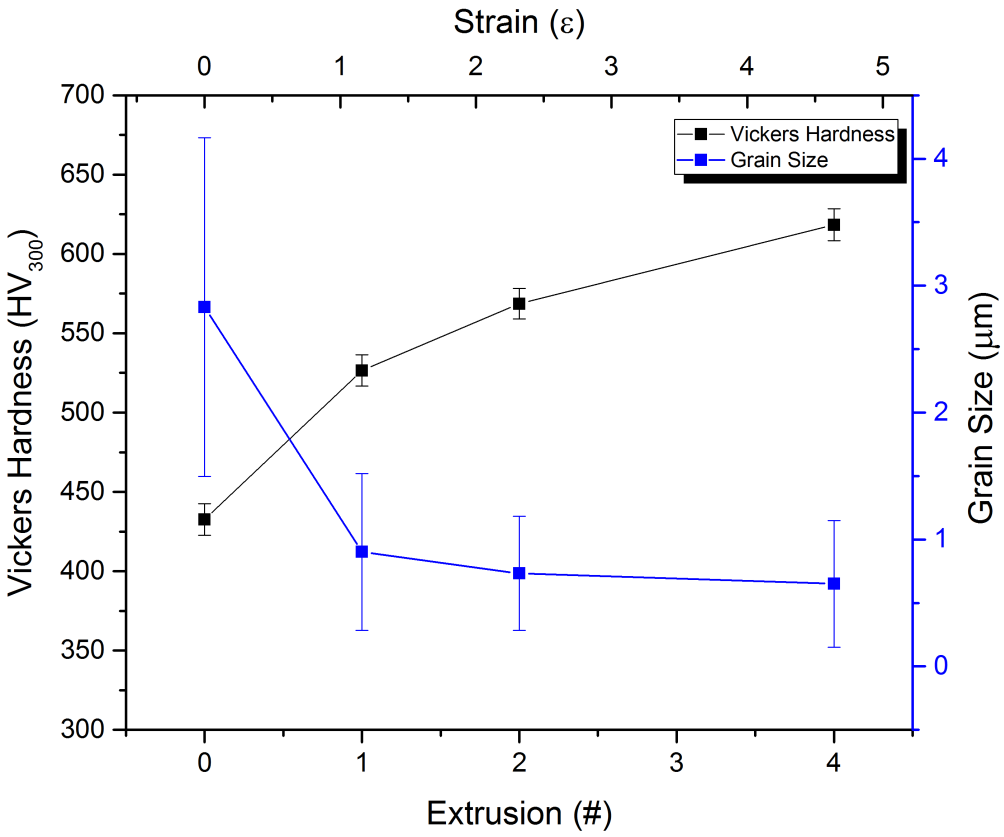

Figure 24. Vickers hardness and average subgrain size values plotted by extrusion number, and plastic strain (top axis)

As shown in Figure 25, the relationship between Vickers hardness and inverse square of average subgrain diameter follow a Hall-Petch type relationship, with error bars indicating the stand deviation of hardness values.

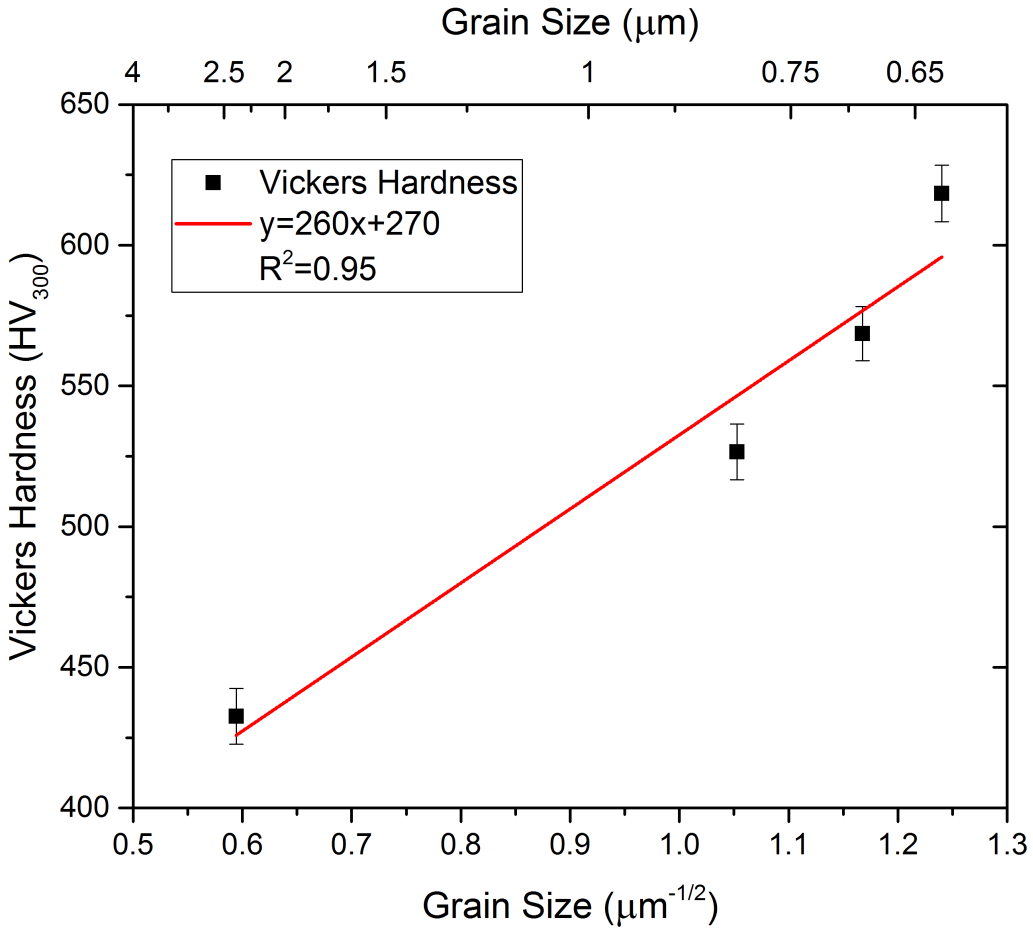

Figure 25 Hall-Petch plot of Vickers hardness data. Vickers hardness measurements made under 300g load on the flow plane.

Examples of the stress-strain curves derived from the three-point bend equations are shown in Figure 26, for each material at temperatures between 24°C and 320°C. In

order to better visualize changes in the stress-strain behavior with temperature, each processing condition is graphed separately and at different scales.

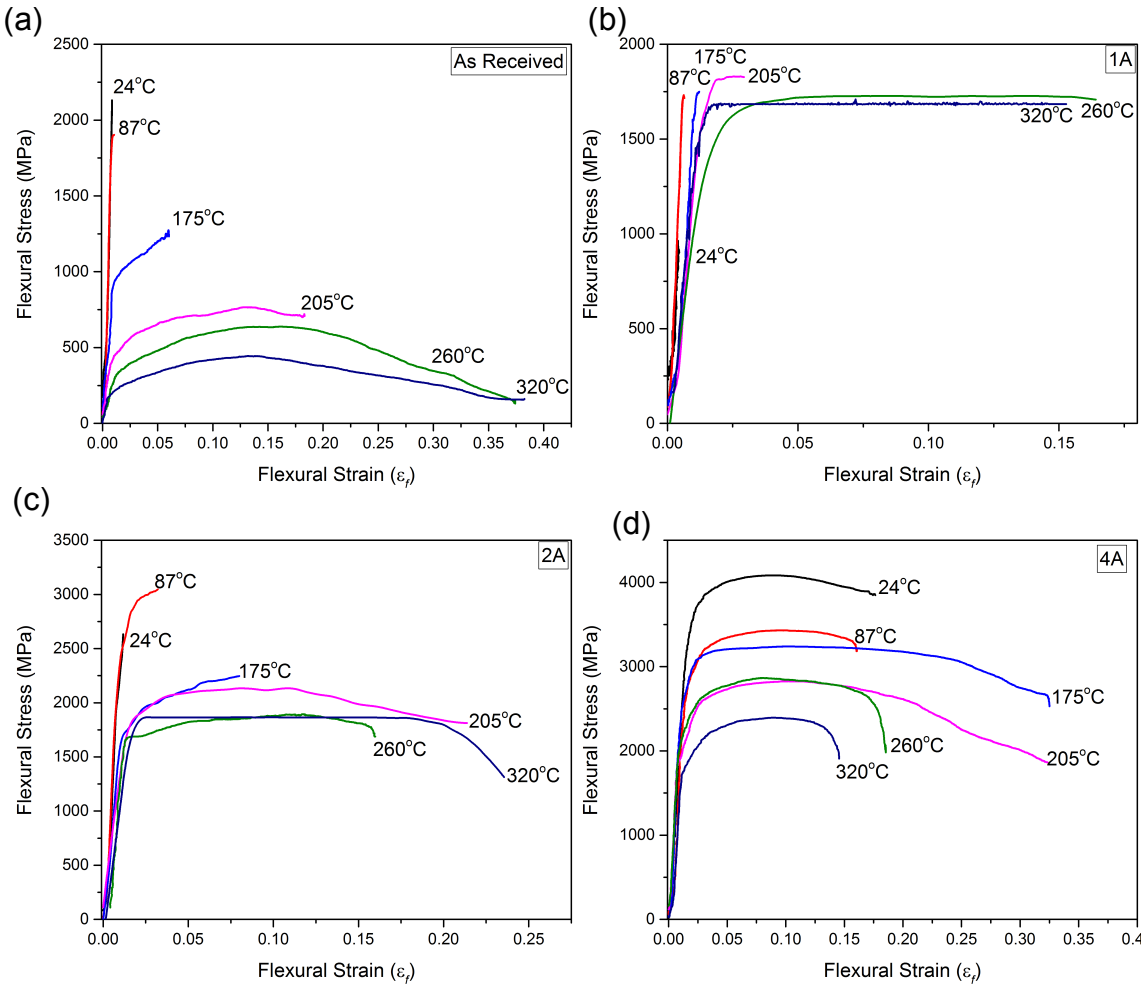

Figure 26. Stress-strain curves for as received and ECAE processed tungsten determined by 3-point bend testing. Estimated strain rate is $0.001s^{-1}$: (a) as received, (b) 1A, (c) 2A, and (d) 4A.

The As received material shown in Figure 26(a) has a dramatic decrease in strength with temperature, from a room temperature UFS of 2000 to 330 MPa at 320°C. This is accompanied by a large increase in ductility, from 0.01El% to ductility greater

than 36%El, over the same temperature range. The YS of AR material decrease more rapidly than the UFS. The ratio between these two values is shown in Figure 27. The Young's modulus of the AR material appears to decrease with temperature but to determine the amount is problematic due to apparatus compliance issues, especially at elevated temperatures. The amount of strain hardening determined by $n=\varepsilon$ at the maximum stress, σmax, also increases with temperature, similar to ductility. Below 205°C determining precise values for *n* is problematic due to premature failure. Above 200°C the value of *n* is approximately 0.13. A complete collection of *n* values for the AR material as well as the 4A material is shown in Figure 28.

In Figure 26(a), the stress-strain curves for 1A material are shown. This 1A material has less ductility than the AR material and fails prior to yielding near ambient temperatures. This results in an increase in UFS from 24°C at 940 MPa, to 2000 MPa, at 205°C. The yield strength at 205°C is 1830 MPa with a ductility of 23%El. The ductility continues to increase up to 24%El at 320°C, while the YS and UFS decrease to1424 MPa and 1680 MPa respectively. While the ductility at 260°C is less than that at 205°C, this result does not appear to be statistically significant with the variation of all data. Determining the strain hardening coefficient for 1A material is problematic due to its brittle nature however, above the DBTT it is similar to the other worked material at approximately ~0.1.

The stress-strain curves of 2A material shown in Figure 26(c) show an increase in ductility over the 1A and AR material at lower temperatures. At 24°C there is no ductility and the UFS is 938 MPa. At 87°C the 2A materials is more ductile with 3%El

and an increase in YS and UFS of 2390 MPa and 3025 MPa respectively. At higher temperatures the ductility of the 2A increases substantially to ~23%El at 320^{o}C, while the YS and UFS drops to 1680 MPa and 1865 MPa. Above 205^{o}C, the strain hardening of the 2A is similar to the other worked materials ~0.1.

In Figure 26(d) stress-strain curves for the 4A material are shown. The 4A material possesses the highest room temperature ductility at 19%El and the highest YS of 3340 MPa, and UFS of 3900 MPa. Like the other processed materials the strength of 4A decreases with temperature and at 320^{o}C the YS and UFS are 1810 MPa and 2430 MPa. Unlike the other materials for this study the ductility increases at 175^{o}C to 33%El but then decreases to 19%EL at 260^{o}C. While the ductility decreases between 205^{o}C and 260^{o}C, the UFSs are similar with 2865 MPa at 205^{o}C and 2880 MPa at 260^{o}C. The YS of 4A material drops at a faster rate than the UFS. This trend can be clearly seen by analyzing the ratio between the two. This ratio of YS: UFS is shown in Figure 27. Work hardening of the 4A material is similar to the other ECAE processed materials and is near 0.1. This data along with the AR results are summarized in Figure 28.

Flat regions seen in stress-strain curves for Figure 26(b) at 260^{o}C and 320^{o}C, Figure 26(c) at 320^{o}C appear to be caused by to calibration settings on the load cell during testing. The loaded calibration file was 55KIP, which was approximately 10x larger than required. This likely caused suppression of recorded data producing a flat line. However it is also possible that this behavior could be caused by a local yielding phenomenon.

The ratio of flexural YS to UFS referred to as the YS ratio is shown in Figure 27, for the AR and 4A materials. In general, this ratio indicates the capacity for plastic deformation. The higher this ratio, the closer the YS and UFS are and the smaller the capacity for plastic deformation. The AR material has as a YS ratio near 1 up to 100°C and then decreases rapidly to 200°C, and the then decreases linearly above this temperature, at a rate of $8E^{-4}$/°C. The 4A material has a constant decrease between 24°C and 420°C, at a rate of $4E^{-4}$/°C, half that of the AR material.

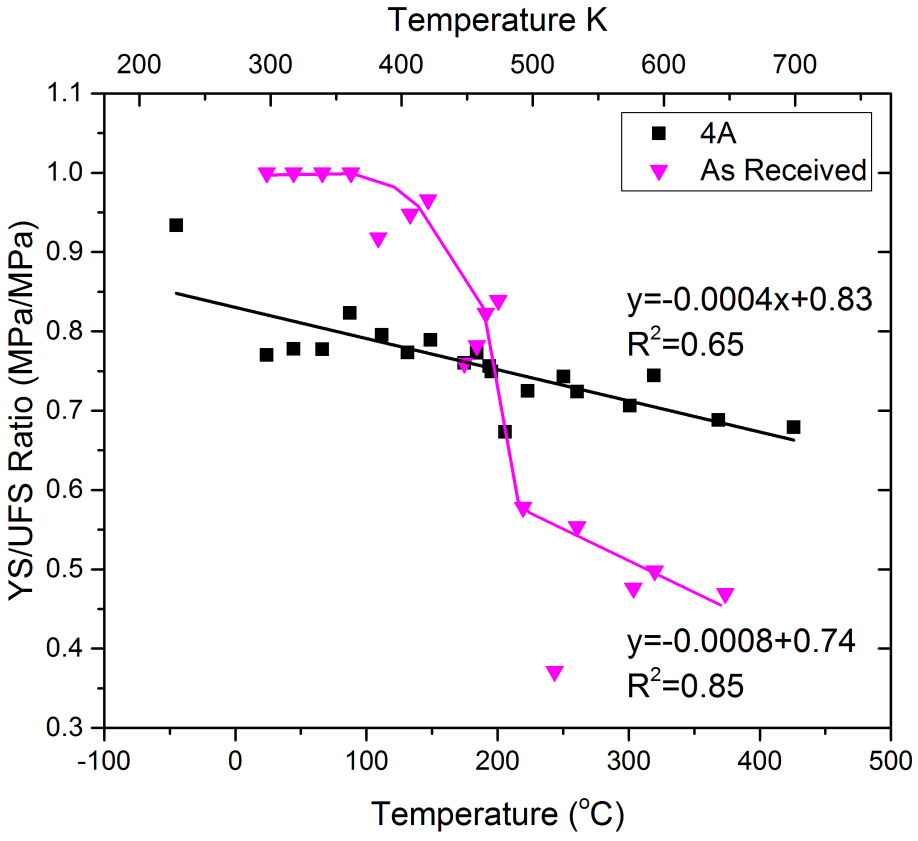

Figure 27. Ratio of YS to UFS of AR and 4A ECAE processed tungsten.

The strain-hardening exponent *n* determined at the point of maximum stress, is shown in Figure 28. These results indicate that the stain hardening of 4A material varies little over the entire test range and is near ~0.1. The AR material has little capacity for strain hardening below the DBTT, but is ~0.13 above the DBTT. The increase in *n* from less than 0.02 below 150°C to 0.13 occurs in a temperature span of 50°C.

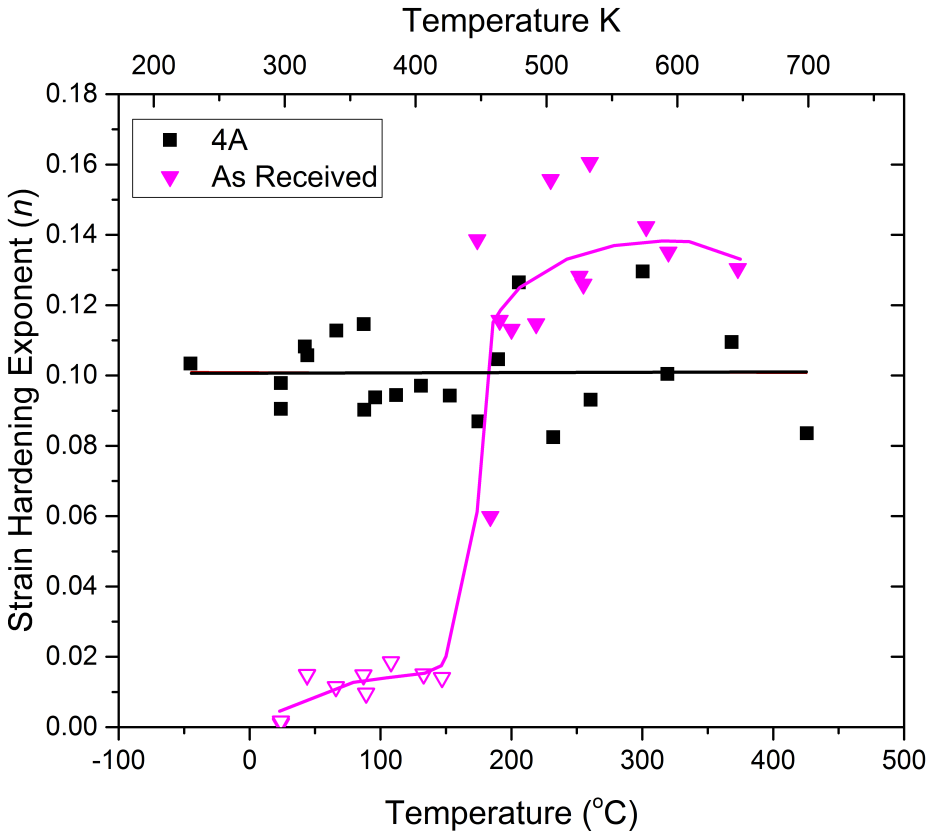

Figure 28. Strain hardening exponent *n* determined at ε of σ_{max} for AR and 4A material. Open as received points indicates brittle failure.

Changes in deformation behavior with temperature can be seen in the optical images of post-tested samples shown in Figure 29. Images were taken on the extrusion flow plane. The crack path is highlighted in white for samples that failed without significant deformation. In the severely bent samples, the deformed areas appear lighter. This is caused by the contraction of material on the side in tension and expansion of material in compression, which alters the surface and causes light to be reflected into the field of view. This region is larger in the AR material than the ECAE processed material due to greater strain hardening, which causes more material to be deformed during testing.

The red dashed line between samples indicates the onset of ductile behavior. Until the onset of ductility, the samples failed in a brittle manner. This occurs in the AR material around 150^{o}C, while it occurs at 225^{o}C for 1A, 75^{o}C for 2A, and less than -45^{o}C for 4A. Above 250^{o}C the AR material deforms plastically and does not fracture within the limits of the test frame. Each of the ECAE processed materials failed in some manner throughout the testing temperature range. Blank entries are due to missing specimens, which could not be recovered after testing.

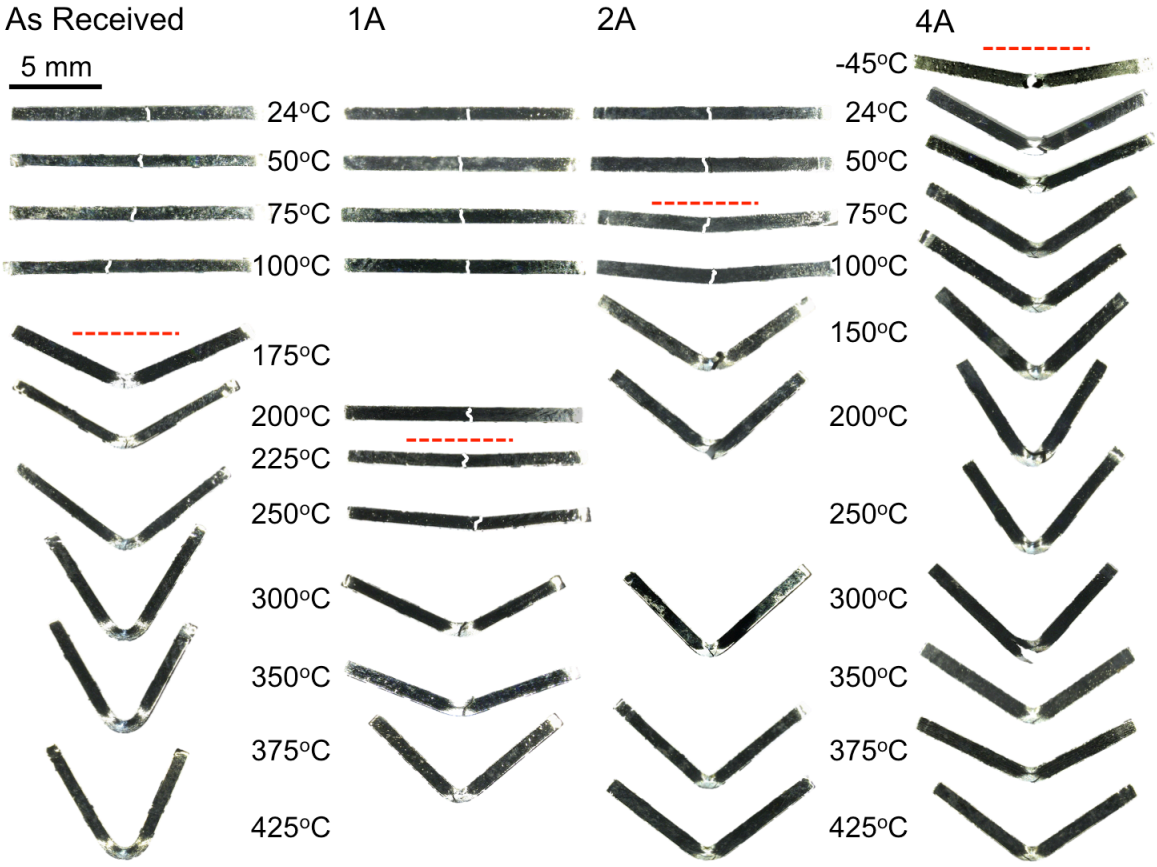

Figure 29. Optical micrographs of 3-point bend test specimens after testing on the longitudinal plane. The red dashed lines indicate the onset of ductility.

Ductility

The total elongations at fracture results for each test specimen are summarized in Figure 30. Values with error bars indicate the average value and standard deviation of multiple data points, otherwise, the data points are from single measurement. The brittle-to-ductile transition for the AR material occurs between 150°C to 250°C. In this 100°C range, the ductility of the AR material changes from less than 2%El, to completely ductile and capable of elongation greater than 35% El. The ductility of 1A material is lower than the AR material over the entire test range, and the onset of its transition occurs 50°C higher than the AR. The highest elongation observed in the 1A material, near 20%El, occurred at the highest test temperature ~375°C. The onset of the brittle-to-ductile transition for 2A occurs below the AR material at ~75°C. The ductility of sample 2A is also higher than the AR material at temperatures up to 150°C. Above this temperature, the ductility of the AR material is greater. The highest ductility observed in the 2A material is similar to that of the 1A sample ~20%El, above 350°C.

The ductility at room temperature of the 4A material was the highest seen ~19%El. Even at -45°C, the 4A material had significant ductility >10%El. These results indicate that the onset of brittle-to-ductile behavior for 4A material is below -45°C. Between 24°C and 100°C, the ductility of 4A appears to remain constant near 18%. The ductility increases between 100°C and 150°C, reaching approximately 28%El between 100°C and 200°C. Some observations of ductility are in excess of 32%El, in this

temperature range. Above 200°C the ductility decreases, crossing below the AR material at 225°C, and the 2A and 1A materials near 300°C with ductility near 15%El at 420°C.

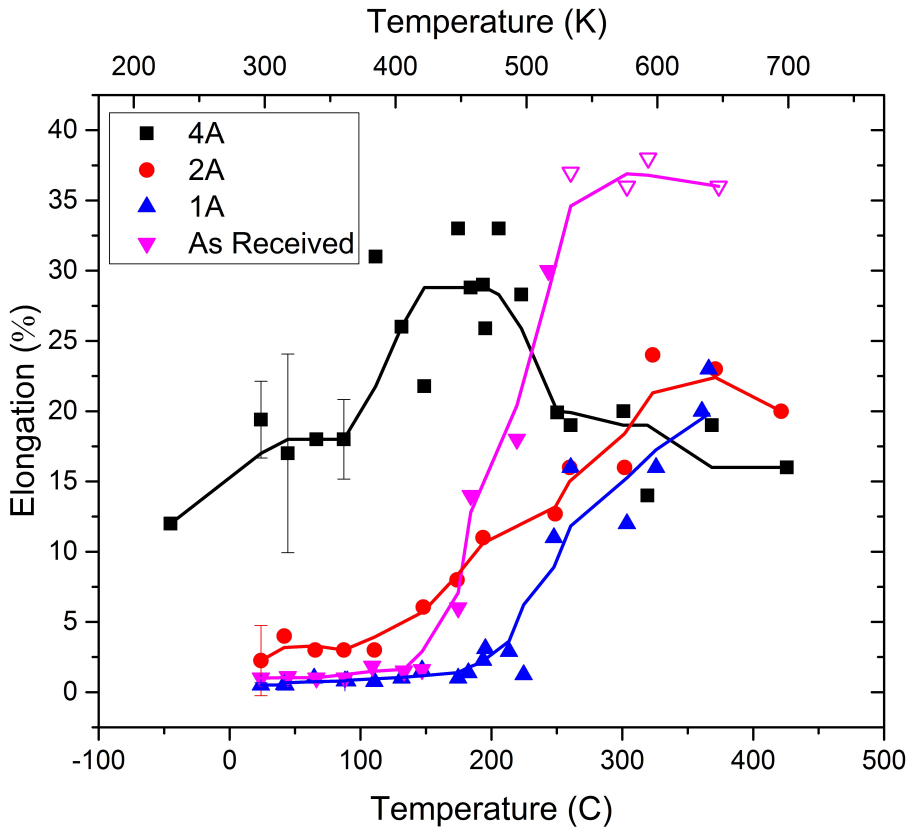

Figure 30. Elongation to failure results of tungsten specimens under 3-point bend testing. Open symbols indicate ductile behavior with no failure.

Yield Strength

The flexural yield stress (YS) for each processing condition is shown in Figure 31. Values with error bars indicate the mean and standard deviation of multiple data point measurements. The 4A material possesses the highest strength over the entire temperature range, with a room temperature YS greater than 3000 MPa. The 2A material possessed the next highest room temperature YS ~2250 MPa, followed by the AR material at 2000 MPa. The 1A case had the lowest YS of less than 1000 MPa. The highest observed YS of 3300 MPa was observed in the 4A specimen at -45^{o}C. The YS of the 4A and 2A decreased approximately 2000 MPa between room temperature and 400^{o}C. Below 150^{o}C the YS of the AR material was approximately 1700 MPa, but then decreased to 1200 MPa over a 100^{o}C temperature increase. Above 250^{o}C the YS decreased at a slower rate and was less than 250 MPa above 400^{o}C. The 1A material differed from the others as the yield strength increased between 24-150^{o}C, approaching the strength of 2A at 150^{o}C. Beyond 150^{o}C the material behaved similarly to the 2A sample. There also appears to be a noticeable decline in the 4A YS near 200^{o}C. However, due to the relatively small size of this decrease, and the lack of repeated tests in this region, this apparent relatively steep decrease with temperature increase should be verified by additional tests.

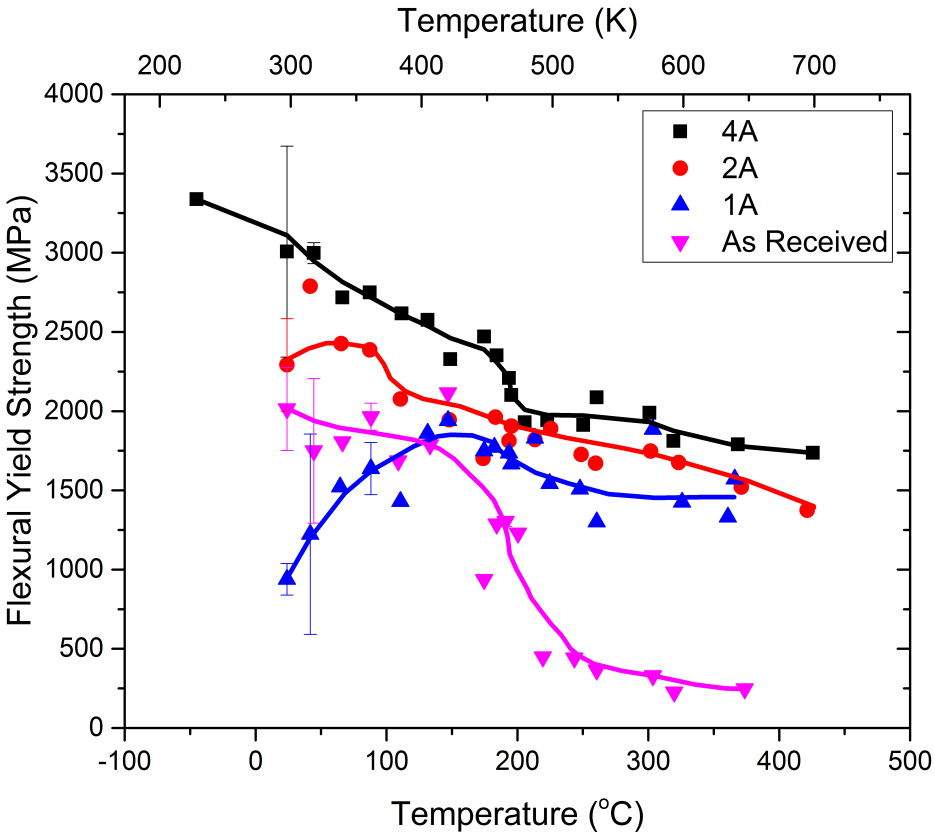

Figure 31. Yield stress results of tungsten determined by 3-point bend testing. The yield stress was determined with an offset of 0.2% strain. Error bars indicate standard deviation of multiple sample measurements at a given temperature.

Ultimate Flexural Strength

The ultimate flexural strength (UFS) data plotted with temperature for each tungsten processing condition is shown in Figure 32. The UFS of the AR material varies little between 24°C and 150°C with an average value ~1900 MPa. Within 100°C of 150°C the UFS drops to ~750 MPa, a rate of nearly 11 MPa/°C. At higher temperatures the rate slows, and by 400°C the UFS is just 500 MPa. Unlike the AR material the UFS

of the 1A material initially increases over the 24°C to 175°C temperature range from 940 MPa to 2000 MPa. Above 175°C the UFS decreases at a rate of just over 1 MPa/°C to 1640 MPa at 365°C. Like the 1A material the UFS of the 2A material initially increases. Except in the 2A material, this only occurs between 24°C and 50°C, increasing from 2550 MPa at 24°C to 3160 at 50°C. Above 50°C the UFS decreases at a rate of nearly 5 MPa/°C to 1580 MPa at 370°C. The 4A material has the greatest UFS of any processing condition with a room temperature UFS of 3905 MPa. The UFS decreases nearly linearly between 24°C and 250°C to 2570 MPa at a rate of 5.5 MPa/°C. At higher temperatures the UFS varies slightly and at 425°C it is 2560 MPa.

The LFS of each material increases with slight elevation in temperature from 24°C to 50°C in AR, 1A, and 2A materials, and from -45°C to 24°C in 4A. This is due to the increase in ductility and decrease in probability of premature failure. While the decrease in UFS of the AR material occurs over a narrow temperature range ~100°C, for the 2A and 4A material this range is much larger, ~300°C for 2A, and ~200°C for 4A. The rate at which the strength decreases is also similar for these worked materials at ~ 5 MPa/°C. Above 250°C, decrease in UFS slows for the AR, 1A and 4A material to ~1 MPa/°C. However determining precise values for these are difficult due to the variation in data.

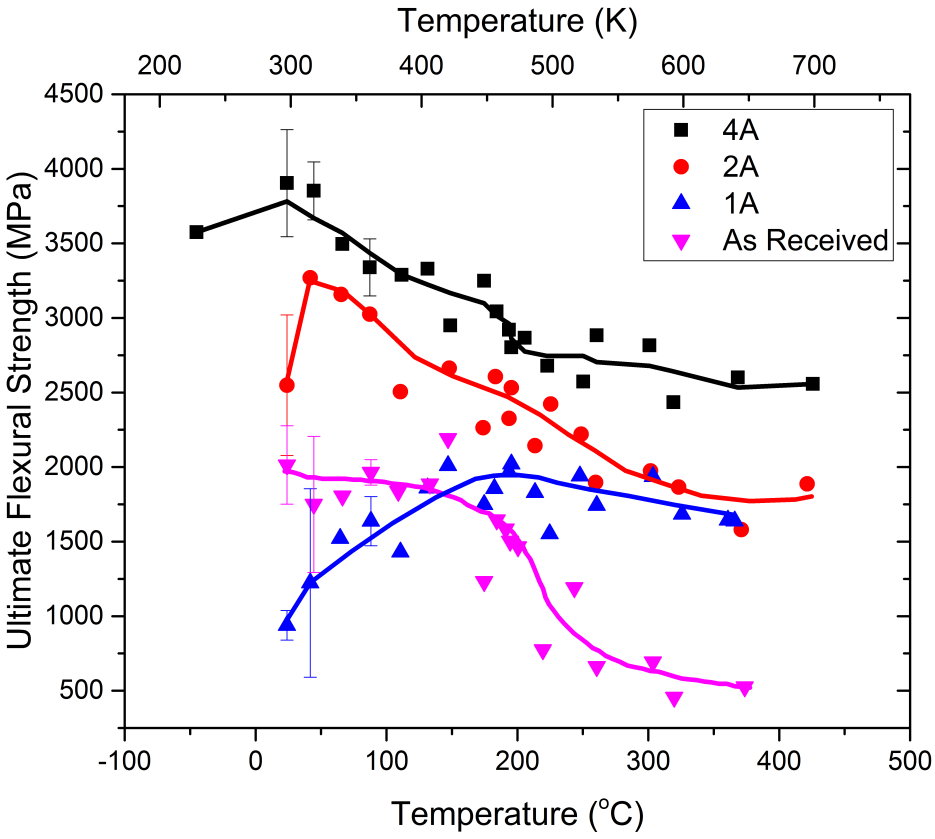

Figure 32. Ultimate flexural strength results of as received, 1A, 2A and 4A ECAE processed specimens. Ultimate flexural strength results are assumed to be the maximum stress values of each stress strain curve.

Manual Strain Measurement

The high ductility observed in the 4A material raised concerns about the validity of the 3-point bend equations for the estimation of strain. In order to investigate this, several samples were recorded during testing and analyzed manually in order to determine actual strain. This was done by measuring the length along the top (compression) and bottom (tension) surfaces, at multiple levels of deformation during

testing. Some of the images used to evaluate the 4A sample are shown in Figure 33, along with stress-stain curves for calculated and measured data, as well as the progression of strain with time for both sets of tensile and measured compression data.

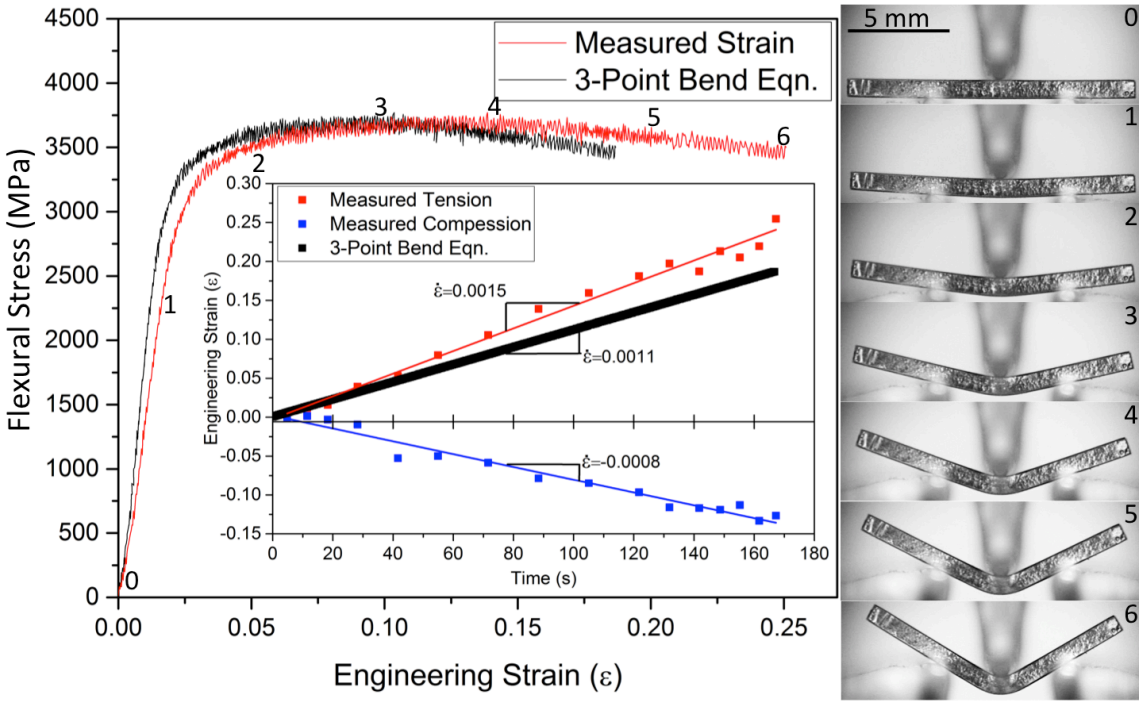

Figure 33. Calculated and measured strain results for 4A processed tungsten at room temperature. Inset depicts the calculated tensile strain and measured tensile and compressive strain with time. Numbered images correspond to numbers along the measured stress strain curve.

At small displacements the difference between the measured and calculated strains is small, and the YS determined by the calculated values is 2930 MPa while the measured data is 2780 MPa, a difference of ~5%. The measured tensile strain rate of $0.0011s^{-1}$ is slightly less than the calculated value of $0.0015s^{-1}$, and the strain rate in compression is half at $0.0008s^{-1}$. The largest difference between calculated and measured values occurs in the total elongation, with 25%El for the measured data while the calculated values are closer to 17%El. The difference between measured compression and tensile values indicates that the zero stress midpoint assumption is not valid, and that the true zero stress point in closer to one third of the height from the upper surface. Ideally all samples would be measured manually in order to calculate the total elongation, however at elevated temperatures this is not possible, as the furnace does not possess a viewing window.

Fracture Energy

Besides ductility, the miscalculation in strain from 3-point bend equations also affects toughness measurements, which are a measure of energy absorbed to failure per unit volume of material. While it in known that toughness values determined by 3-point bend equation stress strain curves are inaccurate, a similar value can be measured directly from the load and displacement data used to determine stress-strain curve, as the total area under the load-displacement curve is equivalent to total energy expended to deform the material. This total energy value can be determined through integration of the

load-displacement curves. The total energy can then be normalized by testing volume. In the case of 3-point bend samples that is the cross sectional area × the span length. However, from the optical micrographs, seen in Figure 29 and the comparison of manual measured and calculated strain values seen in Figure 33, it is clear that the amount of deformation is not uniform throughout the sample. Because of this, the total energy is normalized by just the cross sectional area, producing a facture energy (FE) value with units of Energy/Area.

The fracture energy (FE) results of tungsten 3-point bend tests are summarized in Figure 34. Units for the FE data are in mJ/mm^2. The open AR symbols indicate the sample did not fail within the limits of the test frame. These values represent the deformation energy instead of the fracture energy.

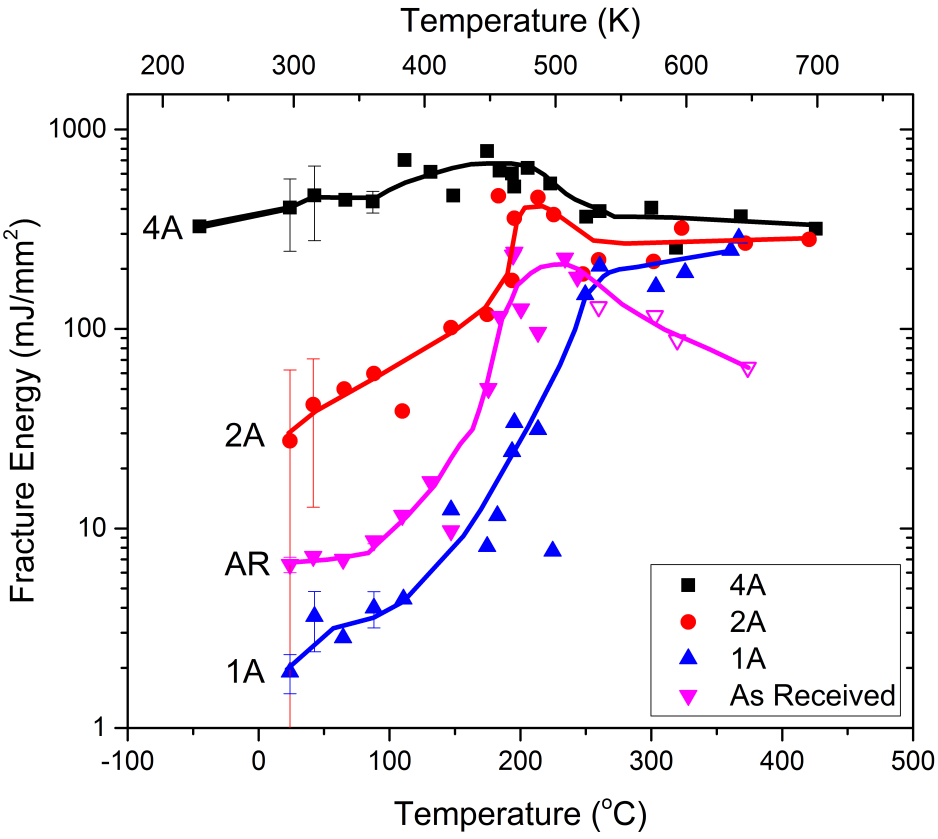

Figure 34. Fracture energy versus temperature of tungsten 3-point bend specimens tested at a displacement rate of 0.01mm*s^{-1}.

The initial FE of AR material at room temperature is ~6 mJ/mm^2, and remains stable to 90^{o}C. The FE then increases rapidly with temperature above 90^{o}C, and reaches a peak value of~240 mJ/mm^2 around 200^{o}C, before dropping to 64 mJ/mm^2 at 370^{o}C. At room temperature the FE of 1A material is less than 2 mJ/mm^2. Initially the increase in FE of 1A with temperature is gradual, reaching ~4.5 mJ/mm^2 at 110^{o}C. Above 110^{o}C FE increases rapidly to 205 mJ/mm^2 at 260^{o}C. At higher temperatures the FEof 1A increases marginally and at 370^{o}C it is 285 mJ/mm2.

The room temperature FE of 2A material is 27.5 mJ/mm^2 nearly 4 times that of AR material. Initially the FE increases linearly with temperature up to approximant 190^{o}C to ~175 mJ/mm^2. Above 190^{o}C the FE increases rapidly reaching a peak value near 455 mJ/mm^2 at 220^{o}C. Above 220^{o}C the FE initially decreases to ~190 mJ/mm^2 to 250^{o}C, and then increases gradually to 280 mJ/mm^2 at 420^{o}C.

Material processed by 4 passes of ECAE, has the highest FE of any of the tungsten materials. At -45^{o}C, the FE of 4A material is 340 mJ/mm^2, and at room temperature it is 405 mJ/mm^2. The FE of 4A material increases with temperature up to a peak of ~780 mJ/mm^2 at 175^{o}C, and then decreases to 364 mJ/mm^2 at 250^{o}C. Above 250^{o}C the FE for 4A material varies slightly but remains relatively unchanged to 420^{o}C with a FE of 320 mJ/mm^2.

Notched Bend Tests

The stress strain curves of notched and un-notched 4A specimens are shown in Figure 35. The specimen was notched by done by scoring a line across the width of a tension specimen with a diamond scribe. Notching lowered the ductility of the 4A specimen by more than half. However, the amount of tensile strain in the notched specimen was approximately 8%. Notched specimens were tested for each processing condition and a similar decrease in elongation was noted for all materials. Differences in the stress-strain curves for the notched un un-notched specimens can also be seen in this figure. The Un-notched specimen indicates a typical stress-strain curve with greater noise that the slightly a typical notched specimen, which appears to have a linear extension after yielding. These differences as well different apparent moduli are most likely stem from changes in the calibration setting between tests. For the notched specimen a 55 KIP load setting was used, which flattened the data, while a 5 KIP setting was used on un-notched specimens, producing the increase in noise seen in Figure 35. This may cause some error in the calculation of stress, however the strain data is unaffected because it is determined by cross head displacement and sample geometry. Despite the differences in calibration settings the YS of both samples is within the normal variation for the rest of the room temperature 4A material tests. Both curves also overlap below 1250 MPa, indicating notching does not impact the flexural modulus. The different calibration setting as well as natural variation seen in other specimens also likely cause divergence of the stress-strain curves above 1250 MPa.

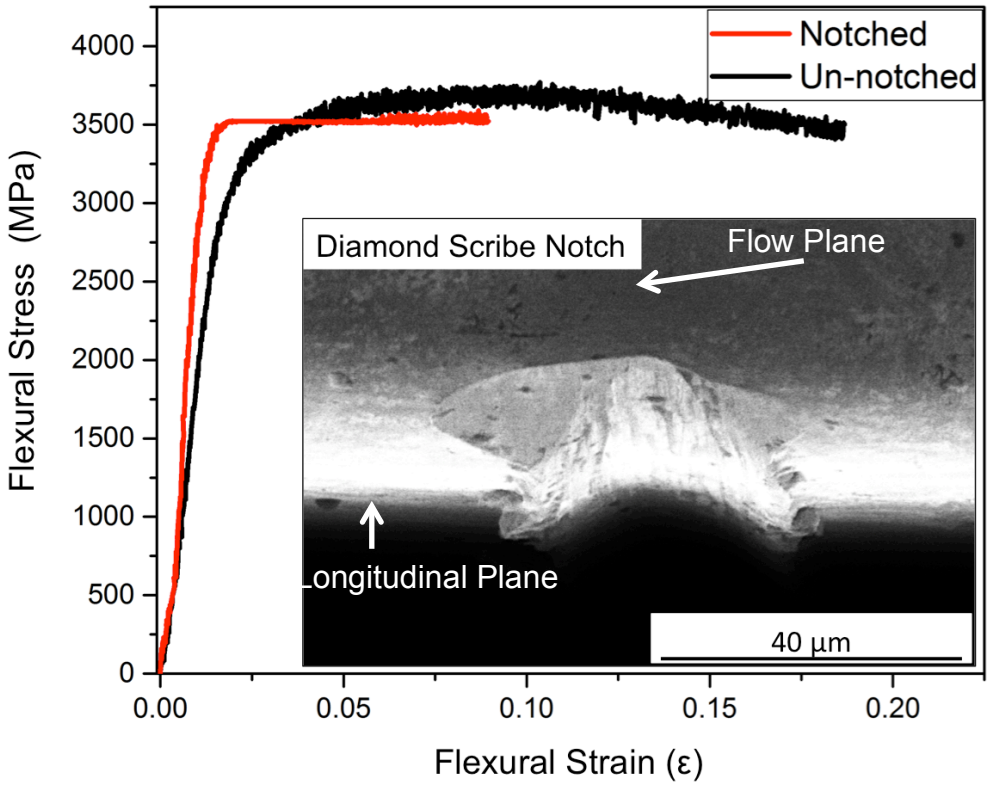

Figure 35. Calculated stress-strain curves of notched and un-notched 4A bulk tungsten specimens tested by 3-point bending at room temperature. Inset image displays typical notch created by diamond scribe used for this test.

Fracture

Fracture Surface

The fracture surfaces of each tungsten, 3-point bend sample (tested at ambient temperature) are shown in Figure 36. The primary failure in the AR sample was intergranular separation of the sub-grain boundaries. This failure is illustrated in the smooth, faceted faces on the left side of the AR image. In order to illustrate the difference between intergranular and transgranular failure, the region selected for this figure also contains some transgranular failure (arrow at the top center of the upper right image of Figure 36).

Following one ECAE pass, shown in Figure 36(1A), the cleavage becomes almost entirely transgranular, with some intergranular separation. This intergranular separation, indicated by arrows, appears as a stepped surface along the fracture path. The size, shape, and orientation of these surfaces indicate that this feature coincides with the original deformed grain boundaries seen in the optical micrograph in Figure 36. After a second ECAE extrusion, the cleavage behavior remains largely transgranular however; the crack propagation path is less linear than seen for the one extrusion case. Examples of intergranular separation are also visible after a second ECAE extrusion, but do not have the uniform, step-like character (see arrow) seen after one extrusion. Radiating fins, thus indicating some necking occurred prior to failure, surrounds the center region.

Figure 36(4A) illustrates how the fracture surface is altered dramatically with two additional extrusions. Following this level of working, the tungsten resembles a laminated-type structure in both form and failure. Crack propagation occurs by both transgranular cleavage of each tungsten layer as well as intergranular separation similar to delamination. The length of the delamination can extend orders of magnitude further than the height of each layer.

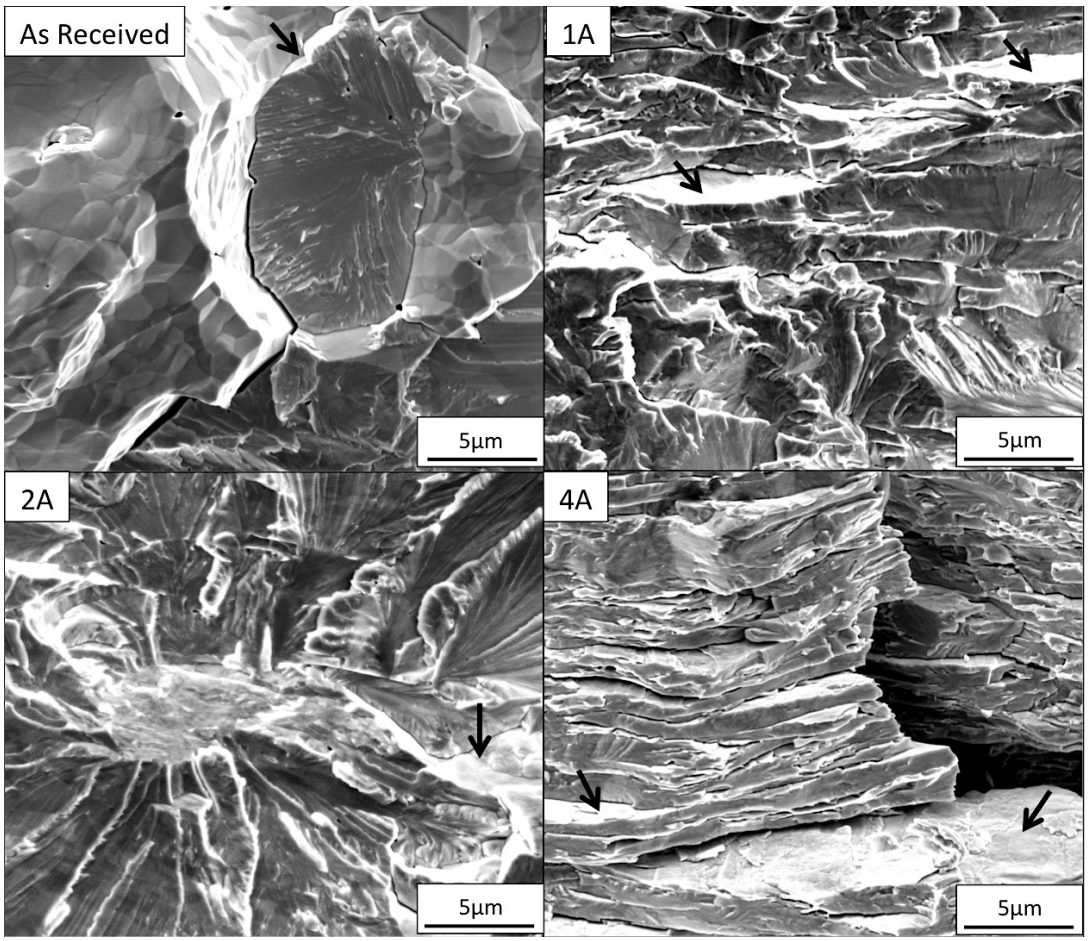

Figure 36. SEM micrographs of 3-point bend fracture surfaces of As received, 1A, 2A and 4A tungsten specimens, tested at 24°C, to failure. Arrow indicates regions of non-dominant cleavage: transgranular in as received, and intergranular in ECAE processed.

Fracture Path

By examining the side of the specimen after testing, the fracture path can be clearly seen through optical microscopy. This plane, which is orthogonal to the loading direction, will be referred to as the fracture plane. For the worked material this plane nearly coincides with the flow plane of extrusions. The orientation of the fracture plane and fracture surface are illustrated in Figure 37.

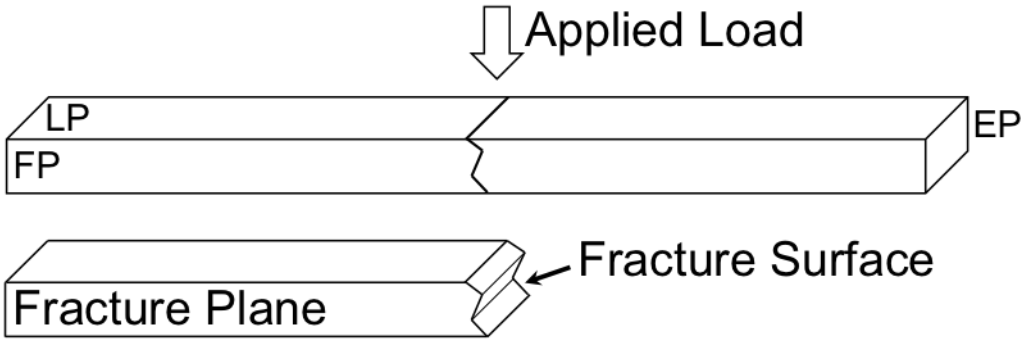

Figure 37. Illustration of post 3-point bend test sample, showing the orientation of extrusion reference planes to the fracture plane and fracture surface.

As Received Fracture

The fracture behavior of the primary crack propagation in the AR material tested at 24^{o}C is shown in Figure 38. No plastic deformation is observed in the specimen prior to failure. A significant amount of crack related deflection is observed, indicating a substantial amount of transgranular cleavage. While the stress state varies with position within a 3-point bend specimen, some insight into the nature of crack propagation can be gained by examining side cracks, where complete failure has not occurred. One such crack is examined at higher magnification in Figure 38(b)-(d). In Figure 38(b). Intergranular separation along the grain and subgrain boundaries can be clearly seen with the use of SEM in backscatter mode, where individual tungsten subgrains are clearly visible. Fracture along the grain boundaries can be identified by the long, relatively straight cracks propagating along the x direction. Intergranular subgrain separation is located in the non-linear region of the main crack, which propagates in the y-direction. Further investigation of the highlighted region in secondary electron mode (Figure 38(b)), illustrates the intergranular separation of subgrains that occurs, as well as some transgranular cleavage. The presence of a preserved crack tip can also be seen in the highlighted area. With the use of the backscatter detector, this crack tip is shown under higher magnification in Figure 38(d). This crack propagates through several tungsten grains before arresting in its current position. The most notable feature of this figure is the deformation surrounding the crack tip. This deformation is caused by the high stress surrounding the crack tip. The stress state surrounding the crack tip along the

surface differs from that of the material interior simply by the presence of a free surface. This is an example of crack tip arrest within the material. However, this image does provide some qualitative information about deformation near the crack tip and a visual representation of the resistance of un-worked tungsten grains to transgranular cleavage.

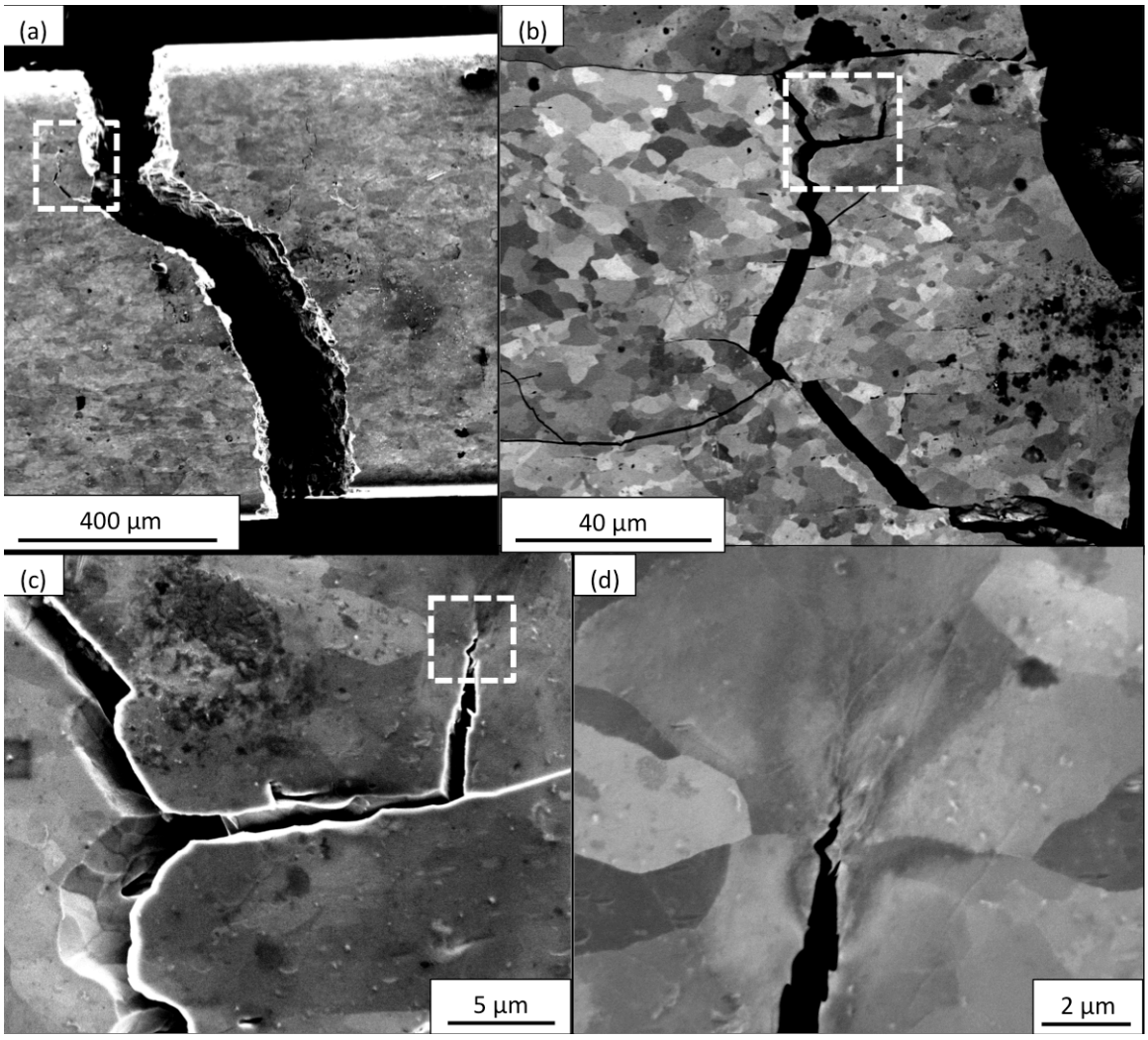

Figure 38. SEM micrographs of an AR specimen tested at 24°C to failure. Figure (a) and (c) are SED images, while figures (b) and (d) are BSED. The areas inscribed by dashed white lines are shown enlarged in subsequent images.

1A Fracture

As previously noted, failure in the 1A material at room temperature occurs predominantly by transgranular cleavage. The fracture plane of one of these 1A specimens is shown in Figure 39. At room temperature, there appears to be no deformation in the sample prior to failure. The angle of crack deflection is also less than in the AR material. This transgranular cleavage is demonstrated in the backscatter image (Figure 39(b)). This image shows a crack path through multiple grains and also crack propagation though multiple worked grains. The lower crack appears to travel between regions of differing grain size. The boundary between small grains and large grain regimes may be an original grain boundary.

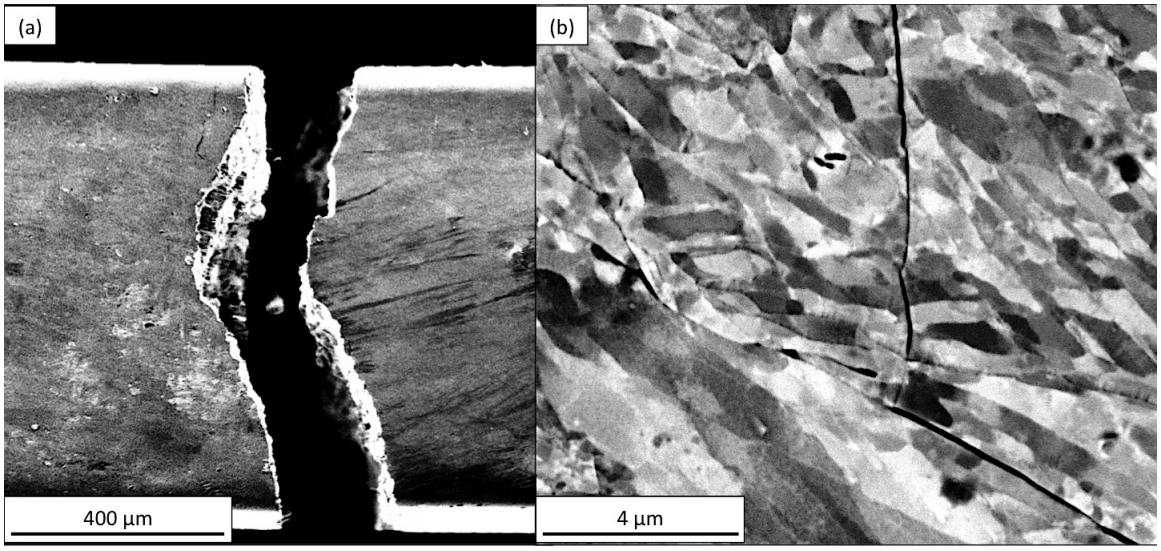

Figure 39. SEM micrograph of 1A specimen tested at 24°C to failure, (a) SED (b) BSED.

2A Fracture

The fracture plane of a 2A-processed tungsten sample tested at room temperature is shown in Figure 40. No plastic deformation was observed prior to failure. The fracture mode is primarily through transgranular cleavage. This transgranular cleavage can be seen at higher magnification in Figure 40(b), with the use of a backscatter detector. The crack can be clearly seen in this figure, where it transects tungsten grains. Another notable feature observed in this figure is the formation of a perpendicular crack ahead of the primary crack tip.

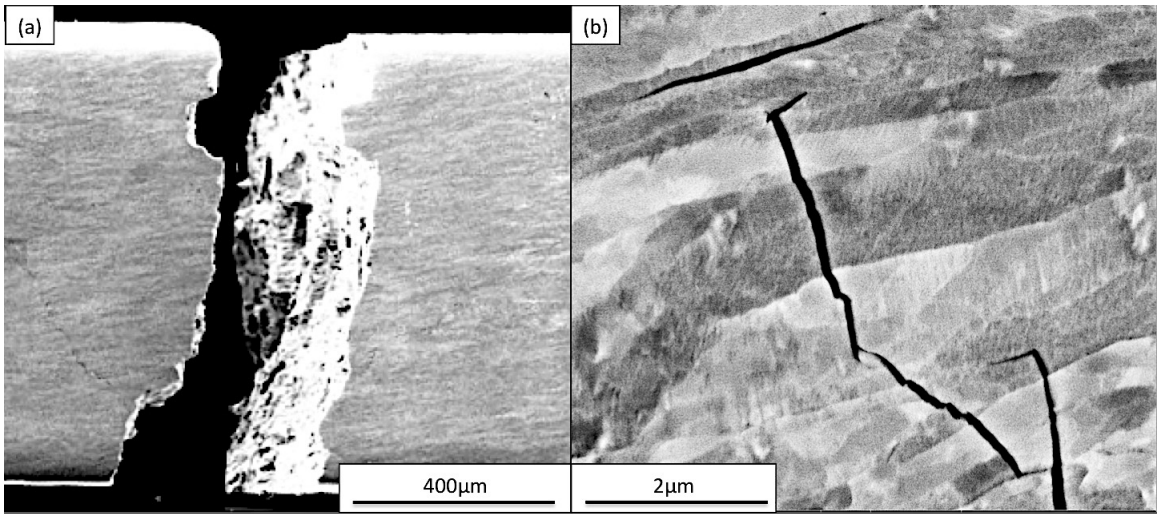

Figure 40. SEM micrograph of 2A tungsten sample tested at 24°C to failure. Secondary electron detector used in figure (a), backscatter electron detector used in figure (b).

4A Fracture

The high degree of deformation observed in 4A specimens at ambient temperature is illustrated in Figure 41. A substantial amount of deformation can be seen, along with the crack path along the fracture plane shown in Figure 41(a). Unlike the other tungsten specimens at room temperature, fracture in the 4A specimen changed direction multiple times. Multiple side cracks are also visible. Some of these cracks are similar to the main fracture path that consists of both delamination and cleavage. Other fracture paths occur by almost entirely by delamination. The delamination-type failure that propagates between tungsten "layers" can extend millimeters in length. In Figure 41(b) and (c), the combined delamination and cleavage modes similar to that of the primary crack path can be seen in greater detail. This alternating cleavage- and delamination-type failure causes the crack path to propagate at an angle near 45^{o} to the loading direction. The longer delamination-type failure is shown at higher magnification in Figure 41(d). In this image, the intersection between two crack systems can be seen. Along the crack surface, several heavily deformed tungsten fibers are also present.

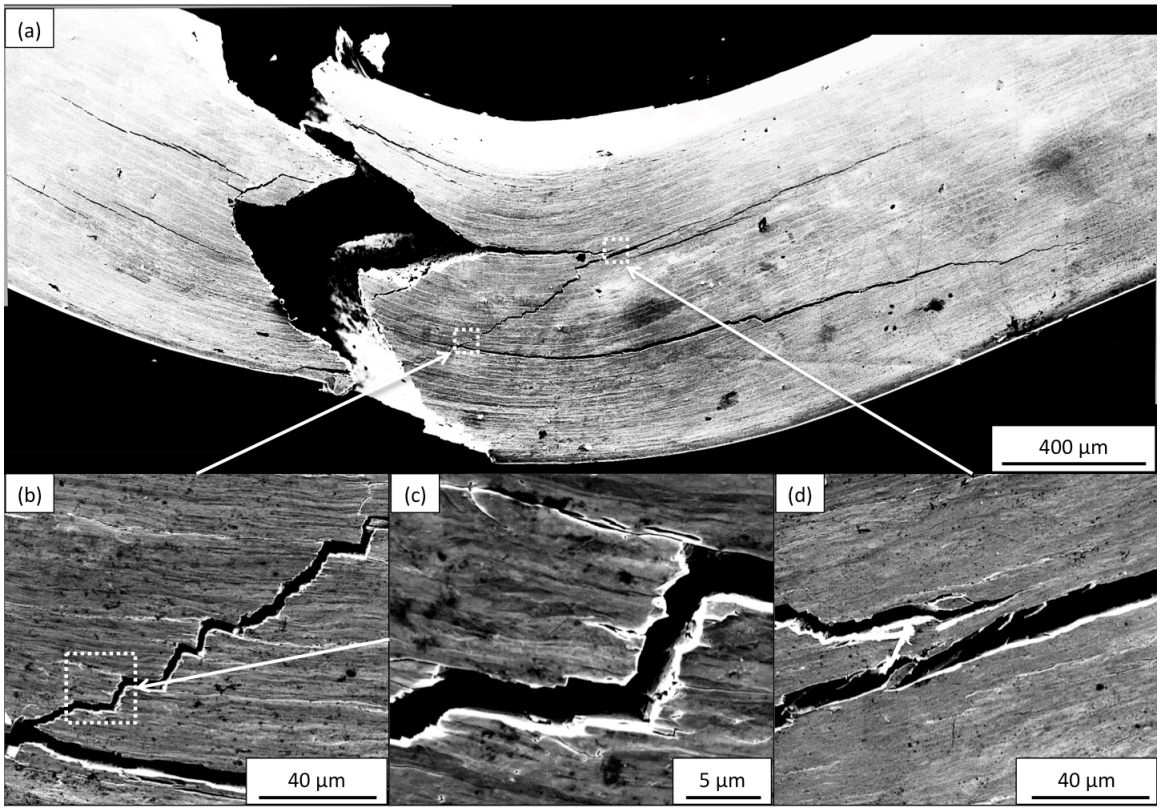

Figure 41. SEM micrograph of 4A specimen tested at 24°C. Figures (b), (c) and (d) are located as indicated. Figure(c) is the only image captured with BSED mode.

In order to determine the mechanism that precipitated failure in the 4A material, a sample was evaluated prior to failure, by performing a 3-point bend test with the displacement limited to approximately 90% of failure. The side of this unbroken test specimen is shown in Figure 42. In this figure, a substantial amount of deformation without catastrophic failure is visible. Regions of plastic deformation are visible in the compression (Figure 42(b)) and tension (Figure 42(c)) regions of the sample. Signs of plastic deformation within the tungsten layers are evident by the presence of tiny shear bands. In compression the formation of a void can be seen through buckling of the

tungsten “layers”. In tension, numerous microscopic separation voids are also present. Larger voids near the bottom surface appear to form between the tungsten layers. Some voids are greater than 4μm in length. Nanometer sized voids are also present and persist in higher numbers at the top of Figure 42(c). These tiny voids also form at the boundary of tungsten grains, and are likely precursors of cracks.

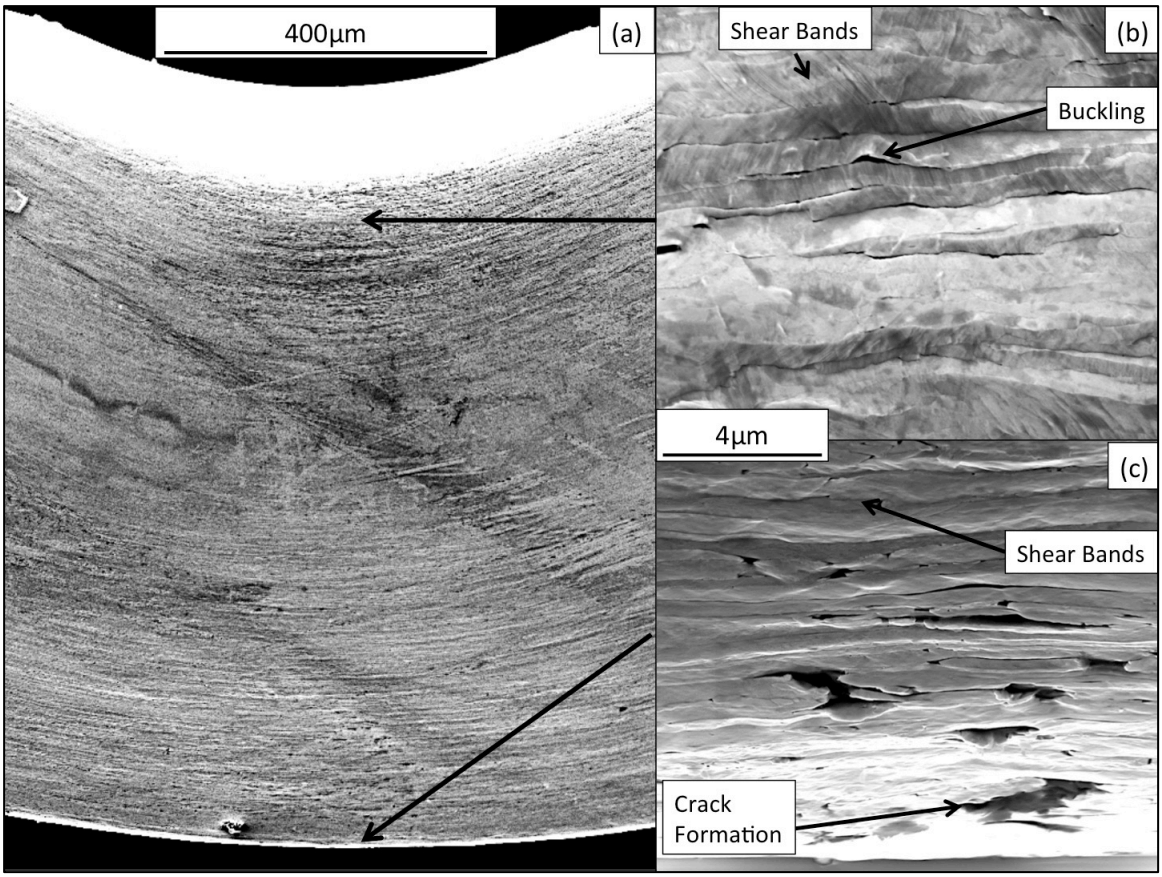

Figure 42. SEM micrograph of 4A specimen deformed to 90% of failure at 24°C. Location of (a) and (b) indicated by arrows.

Ductile to Brittle Transition

As noted previously, the transition from ductile to brittle behavior in polycrystalline tungsten is affected by processing conditions. Differences in the fracture behavior can also be observed through electron microscopy along the fracture surface.

As Received (AR)

The fracture of AR material near the onset of the ductile-to-brittle transition (DBT) ~175^{o}C, is shown in Figure 43. Subtle changes in the failure, can be seen, when compared to material tested at 24^{o}C, indicating the material is becoming increasingly ductile. First, in Figure 43(a), the crack deflection angle, which increases with greater proportion of intergranular fracture, is smaller than the specimen tested at 24^{o}C. Second, in Figure 43(b), failure along the side crack appears to be transgranular. Bridging of the crack path in this figure is also suggestive that the tungsten grains are becoming increasing ductile.

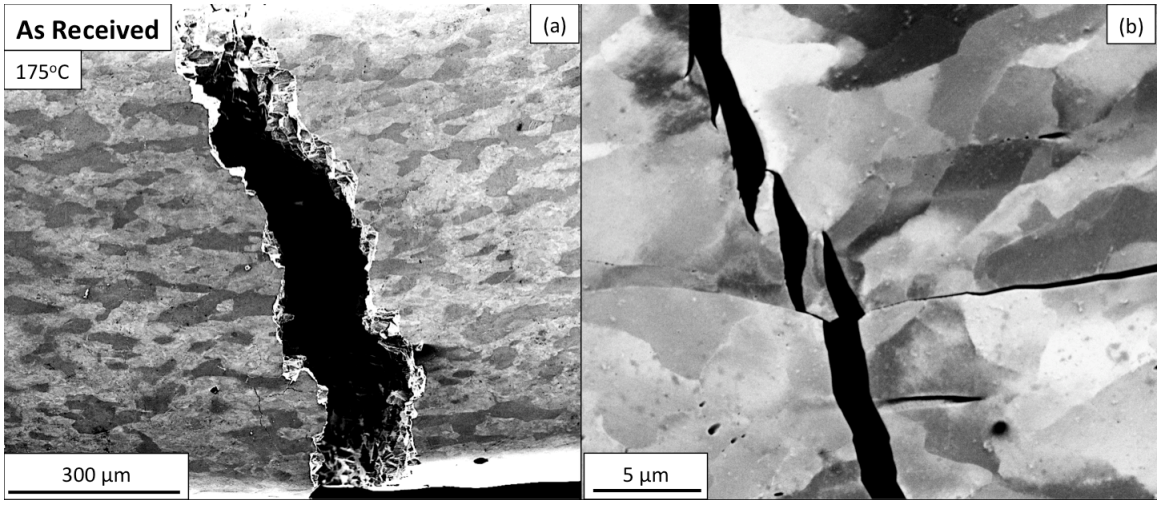

Figure 43. SEM micrograph as received specimens tested at 175°C. SED is used for Figure (a), while BSED is used for figure (b).

Figure 44 illustrates the fracture behavior in the midst of the DBT at ~210°C. At this temperature the specimen deforms significantly prior to failure, and the crack does not propagate completely though the specimen. Highly deformed regions near the top and bottom surface are also observable, along with little crack deflection. Transgranular cleavage on the primary crack system and side cracks is shown in Figure 44(b). Shear band can also be seen in this image.

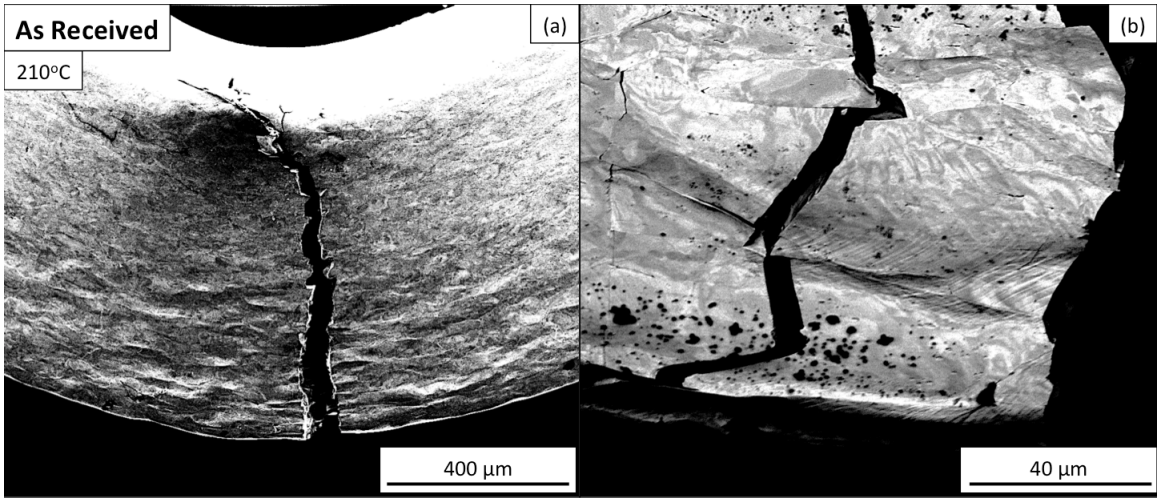

Figure 44. SEM micrographs of as received material tested at 210°C. (a) SED, and (b) BSED.

Above the DBTT, the AR material deforms without failure within the limits of the test apparatus. A sample tested around ~260°C is shown in Figure 45. The high degree of bending is clear, as well as the presence of shear bands along the bottom surface in Figure 45(a). These shear bands are shown in greater detail in Figure 45(b). In Figure 45(c), the formation of a void at grain boundaries is seen.

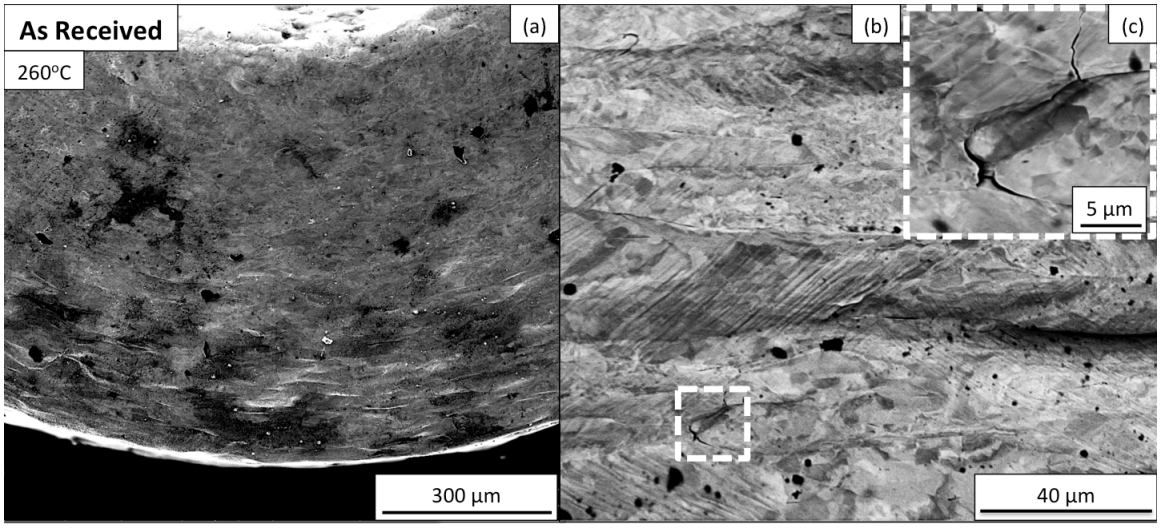

Figure 45. SEM micrographs of as received material tested at 260°C. SED was used for Figure (a), while BSED was used in figures (b), and (c). High magnification figure (c) is located within the white dashed box in Figure (b).

1A

Differences in the fracture behavior of 1A material at various temperatures are shown in Figure 46. Each of the 1A samples failed in a catastrophic manner during testing. At 175^{o}C, the fracture looks similar to that at 24^{o}C. While at 210^{o}C the crack path appears to be less jagged than at 175^{o}C. Midway through the specimen, the crack changes course suddenly at an obtuse angle, appearing to coincide with the alignment of the tungsten grains. This characteristic indicates a delamination-type failure of the tungsten grains. Signs of deformation prior to failure are indicated by the presence of shear bands and bending, which are seen in the specimen tested at 260^{o}C. The 1A material near 325^{o}C fails catastrophically. However, the specimen undergoes a substantial amount of plastic deformation prior to this. A sharp secondary crack deflection occurs midway up this specimen. The location of this deflection appears to coincide with the region in compression.

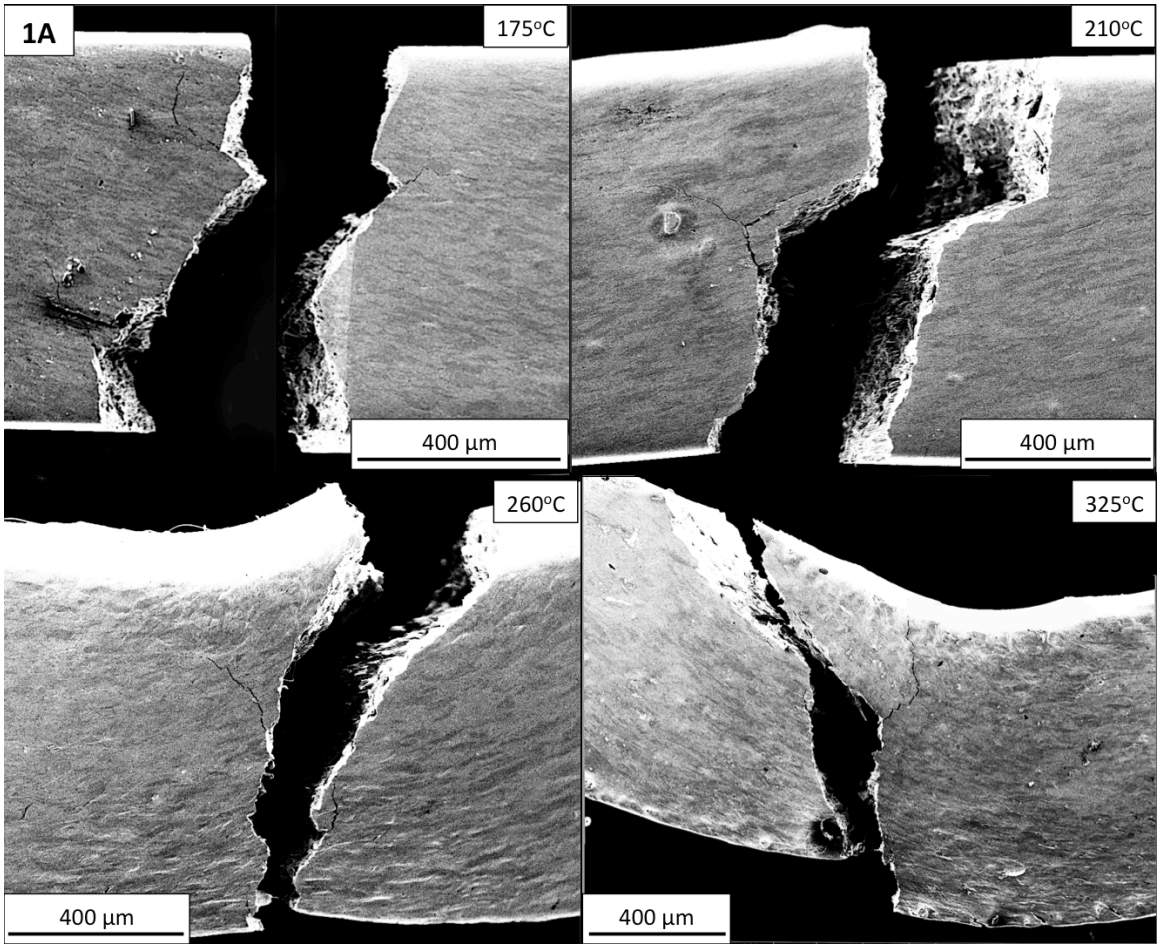

Figure 46. SEM micrographs of 1A material tested at 175 °C, 210 °C, 260 °C, and 325°C.

2A

Figure 47 captures images of 2A processed tungsten samples tested at elevated temperatures. At 175^{o}C some deformation prior to failure is seen in the slight bend at the top of the specimen and the curvature along the bottom. However, no significant shear banding is visible. A delamination-type failure is also present midway up the specimen. Along this delamination failure, several highly-deformed tungsten grains are visible. At 210^{o}C the 2A material did not completely fail, as the crack arrested in the compression region. Two main crack systems can be seen along with multiple branching side cracks. The presence of shear bands can also be seen along the bottom and top of the specimen, indicating dislocation mobility. The fracture geometry at 260^{o}C appears similar to the main crack system at 210^{o}C, without a secondary large crack system and less side cracks. Above the DBTT of AR material, the 2A sample deforms significantly prior to failure by bending. The nonlinear crack path indicates that the mode of failure differs from those at lower temperatures.

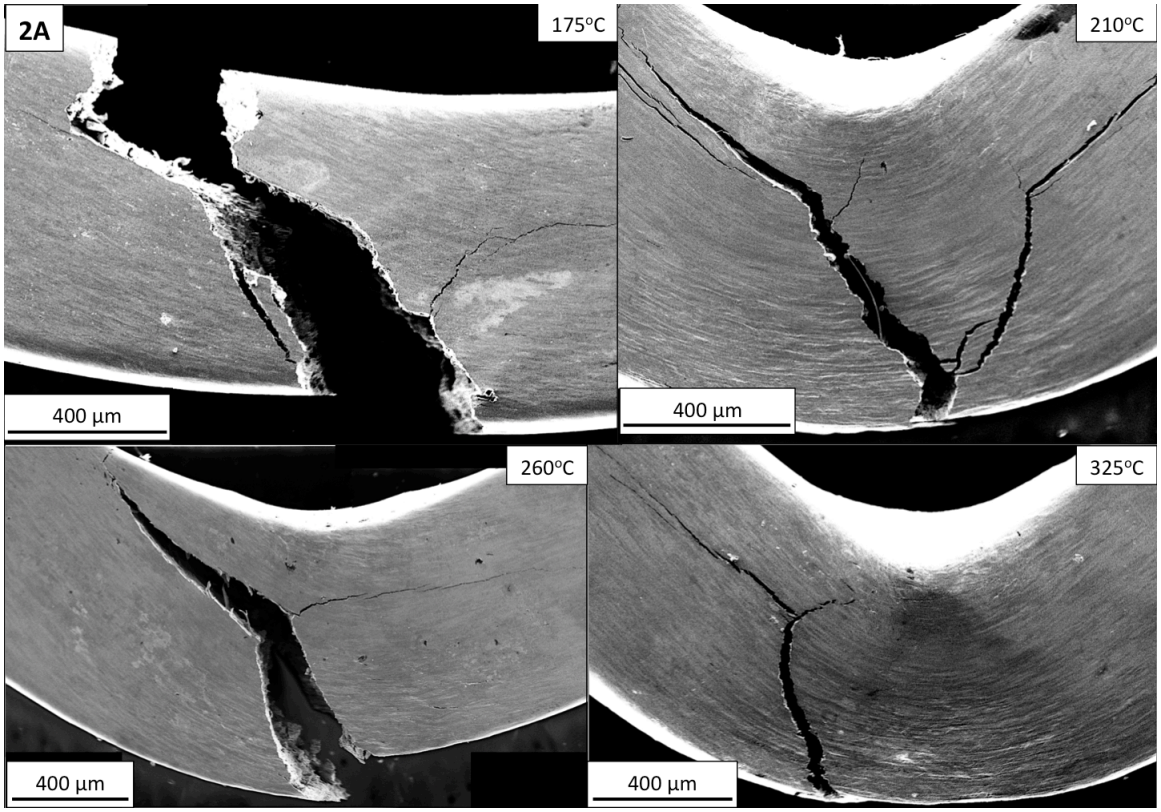

Figure 47. SEM micrographs of 2A specimens tested at 175°C, 210°C, 260°C and 325°C.

4A

The results of bend testing a 4A specimen to failure at 175°C are shown in Figure 48. At this temperature, the 4A material no longer fails catastrophically. Numerous shear bands are visable along both the bottom and the top, between the crack and the upper surface. The main crack propagation deflects far from the loading axis and, unlike the other worked materials, reverses direction midway up the sample before propagating by delamination. Multiple side cracks are also present. These cracks appear to be delamination-type failures. Several of these side cracks also branch out and extend to great distances along the sample.

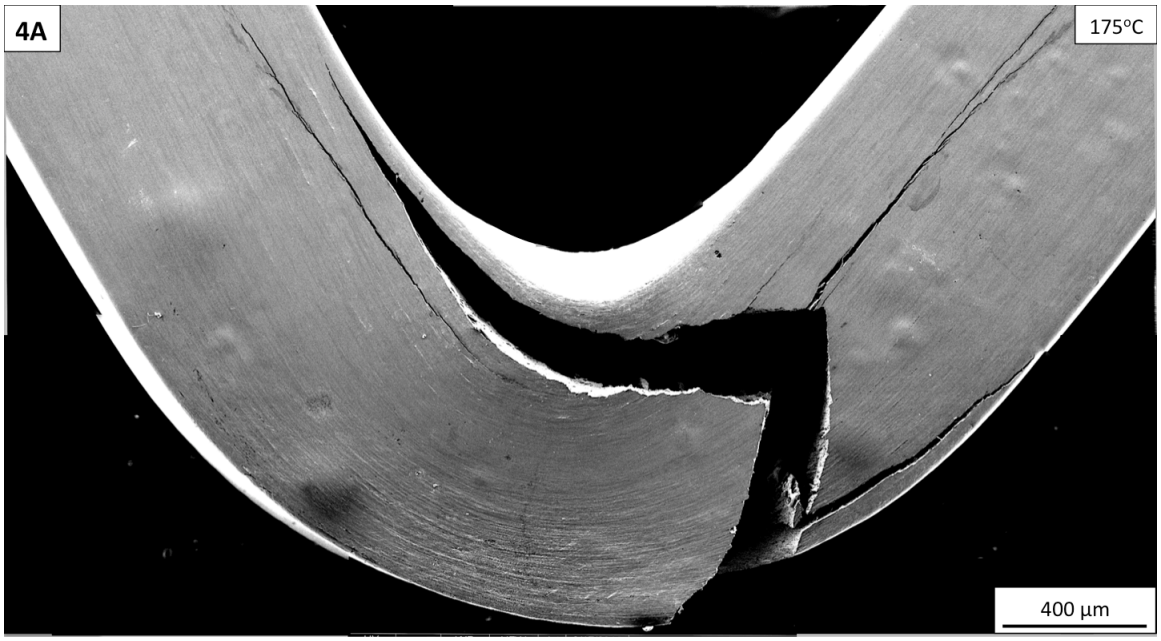

Figure 48. SEM micrograph of 4A material tested at 175°C.

The fracture behavior at 210°C is shown in Figure 49. The shear-banded region at this temperature appears larger than at 175°C. Also, there are fewer side cracks and these extend away from the crack surface. The crack path alternately deflects away and then towards the loading axis before causing a large delamination failure. At the edge of this delimitation failure several highly deformed tungsten fibers can be seen bridging the gap.

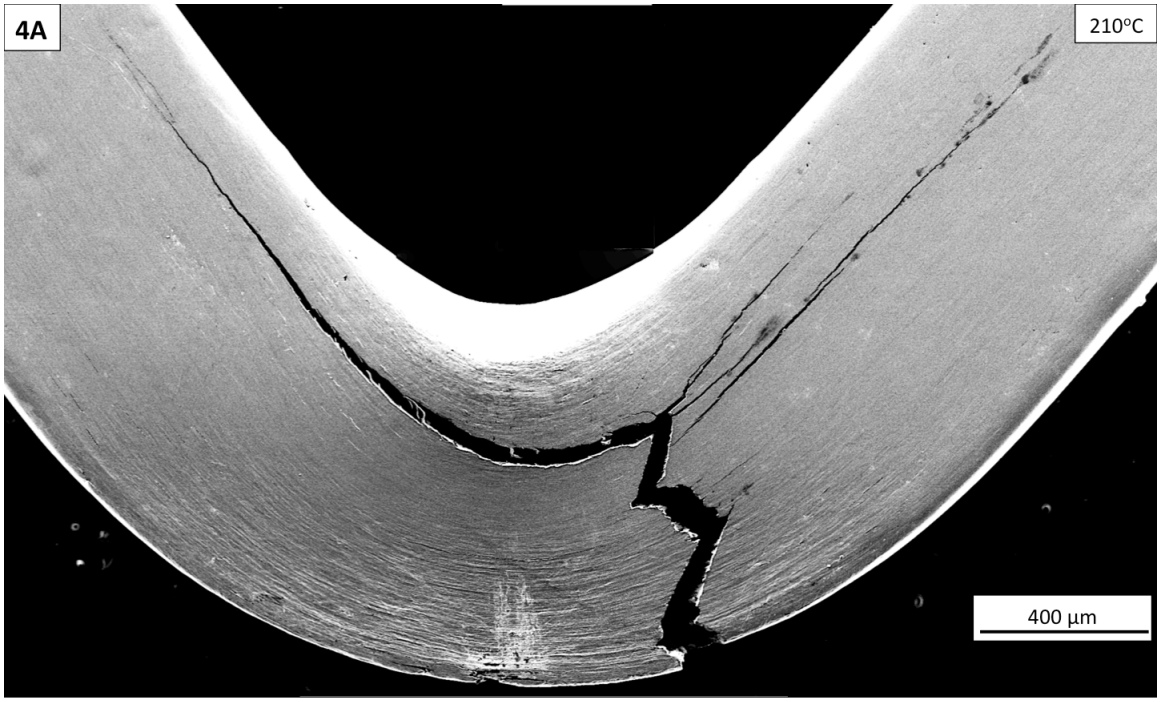

Figure 49. SEM micrograph of 4A material tested at 210°C.

After failure at 260°C, a substantial amount of material remains without evidence of fracturing. This fracture plane is displayed in Figure 50. At this temperature crack propagation no longer changes direction, and the transition into pure delamination failure is gradual. Several tungsten filaments can be seen bridging the crack path. Along the bottom, the fracture surface is also visible. Along this surface and the corresponding edge it appears that the tungsten layers failed after necking. Continued testing after initial failure caused the large gap between the bottom fracture surfaces. This was done unintentionally and was caused by the unbroken section at the top. The top region retained enough strength that the failure detection parameters were unable to detect failure.

Figure 50. SEM micrograph of 4A specimen tested at 260°C.

The fracture plane of a 4A tested sample at 325°C is shown in Figure 51. Shear bands are noticeable in both the compression and tension regions of this sample. The amount of bending prior to failure has decreased, along with the length of pure delamination failure. Instead, the crack appears to alternately propagate by delamination and then through yielding of multiple tungsten layers at once. These tungsten layers also appear to have failed by yielding and necking, rather than transgranular cleavage.

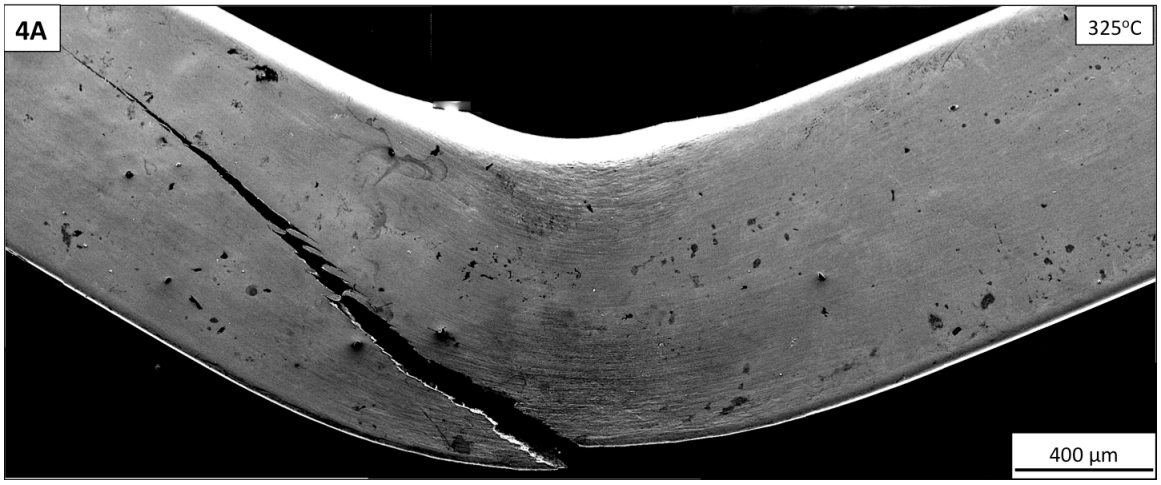

Figure 51. SEM micrograph of 4A specimen tested at 325°C.

In Figure 52, close to the highest temperatures tested in this study ~360°C, the yielding behavior of tungsten grains is clear. The amount of deformation prior to fracture has decreased and there are no obvious shear bands near the top or bottom surface. Most of the crack path is caused by delamination and intergranular separation. In the locations where the crack path crosses tungsten grains, it appears to do so by plastic deformation and not through tansgranular cleavage. The plastic deformation failure of the tungsten layers is clear at high magnification in Figure 52(b). In this image necking of several tungsten layers is apparent.

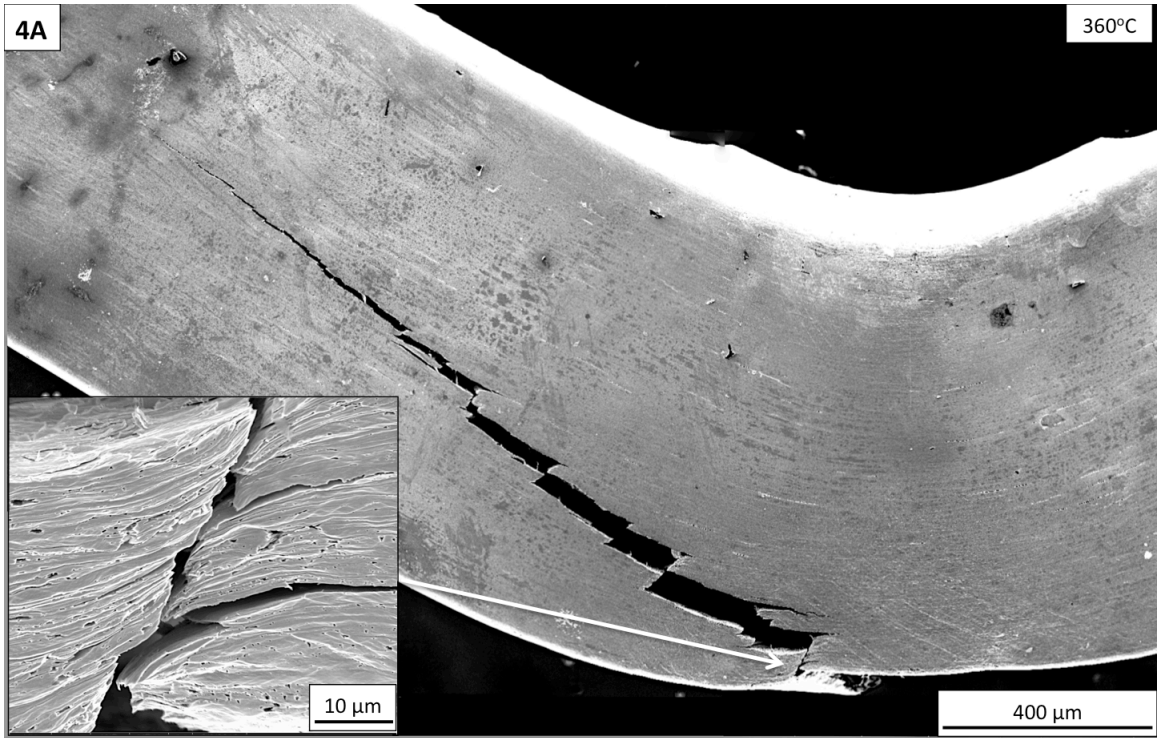

Figure 52. SEM micrograph of 4A specimen tested at 360°C. Location of (b) indicated by arrow.

Crack Deflection Angle

In Figure 53, the crack deflection angles as a function of testing temperature for the AR and 4A materials are summarized.

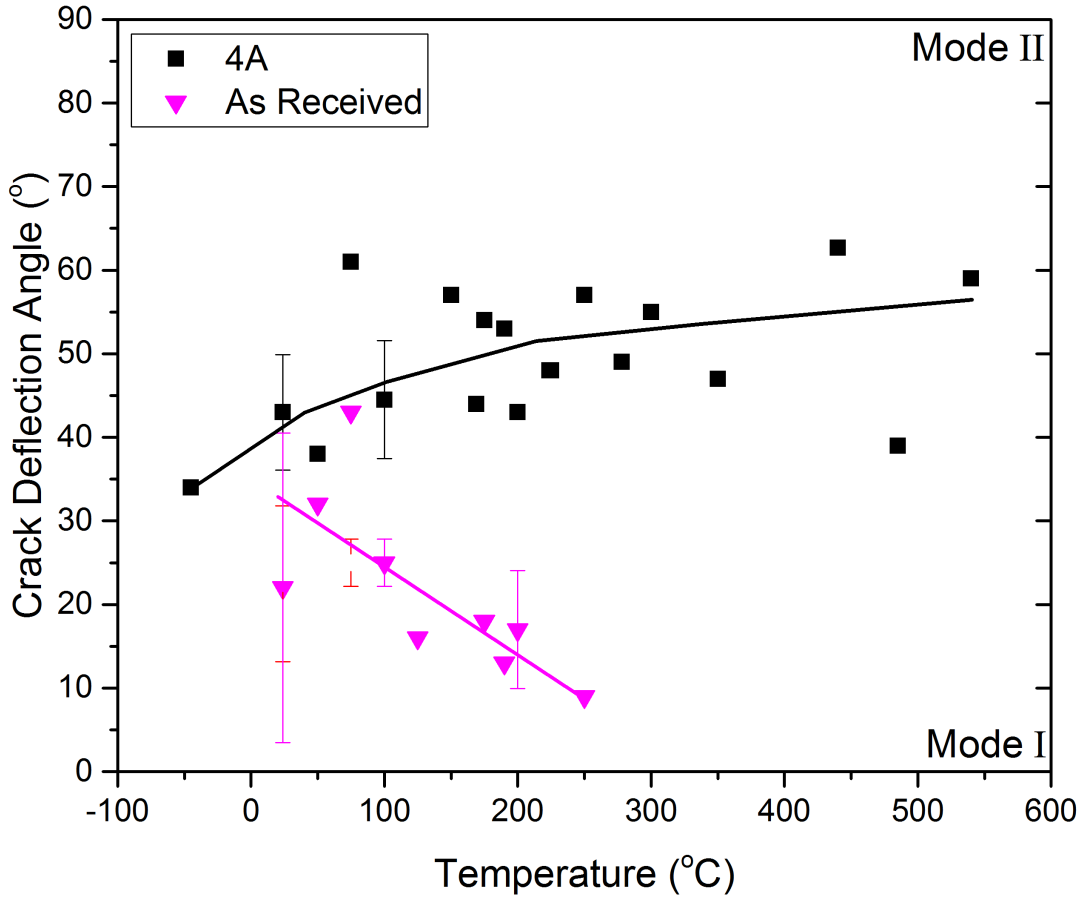

Figure 53. Crack deflection angle versus temperature or As Received and 4A materials versus temperature.

The amount of crack deflection is related to the proportion of intergranular failure to transgranular failure. Higher crack deflection angles indicate greater amount of intergranular failure. The crack deflection angle of the AR material decreases with temperature from ~30^{o} at 50^{o}C to 8^{o} at 250^{o}C, indicating an increasingly amount of transgranular cleavage. While the 4A material shows the opposite behavior. The crack deflection increases with temperature up to ~300^{o}C. Above 300^{o}C the deflection data is too scattered to make definite conclusion but the values appear to be reaching an asymptote near 60^{o}.

CHAPTER VI

DISCUSSION

Processing

Through ECAE processing, bulk polycrystalline tungsten was severely plastically deformed to greater amounts of strain at lower temperatures than previously reported. The processing complete in this work can be seen compared against previous work in Figure 54. Most notable, the tungsten processing reported here was conducted at 300^{o}C below all other methods at similar amounts of stain, and the only tungsten processed at similar temperatures had accumulated stain greater than 8.

The success of this processing approach is likely due to the influence of strain rate, deformation mechanics, and stress state during processing. The strain rate behavior of tungsten has been examined previously [19, 123, 138-140], especially the alteration of the DBTT with strain rate [138, 141-143]. Based on this, it can be assumed that the very slow strain rate used for processing here reduced the DBTT sufficiently to permit this plastic deformation without fracture, possibly through a creep like deformation behavior, where dislocations had sufficient time to reorganize during processing. The simple shear processing utilized by ECAE may have also enabled this successful processing because tensile strain is minimized with this method. The hydrostatic stress imparted to the tungsten by the stainless steel can is another possible explanation of the successful

processing. The can imparts a compressive stress, to the tungsten and decreases the opportunity for the formation of cracks during processing.

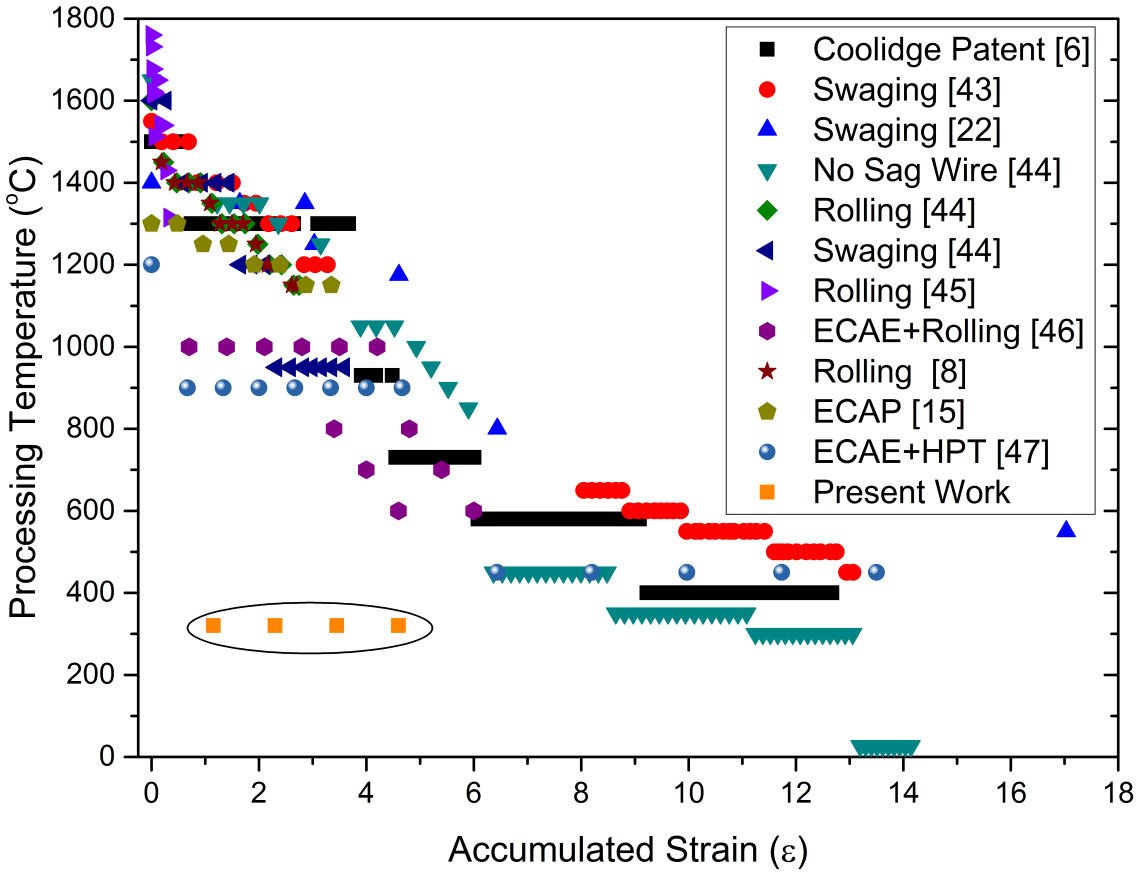

Figure 54. Tungsten processing data from the literature and this work, decomposed into accumulated strain at each processing temperature.

Besides producing high ductility at room temperature, the 4A ECAE processed tungsten also shows a substantial increase in strength and fracture energy when compared to the as received material. The improved mechanical behavior is attributed to the microstructure and texture features produced by the ECAE processing. These

features include higher dislocation density, refined sugbrains, elongation/orientation of grain boundaries and orientation of the {100} and {110} planes.

Dislocation Density

The severe plastic deformation incurred through low temperature ECAE processing reported here undoubtedly induces very high dislocation densities within the tungsten. The initial material appears to have relatively low dislocation density. The recrystallized appearance of the microstructure as well as texture and mechanical behavior though hardness and strength values all support this assertion.

The presence of higher dislocation densities in the ECAE processed material contributes to the change in failure mode from intergranular separation in AR to transgranular cleavage in worked material. The cause of this change has been studied extensively and is attributed to limited dislocation mobility in the presence of preexisting dislocations [10, 124, 144-146]. These preexisting dislocations create barriers for the migration of dislocations away from the high stress field surrounding a crack tip, limiting their ability to absorb and dissipate energy. With fewer energy dissipation mechanisms, the material becomes more less ductile, and the DBTT increases [59]. This behavior has been reported in both single [9] and polycrystalline materials [147]. Similar behavior was observed in the 1A material presented here, but was not the case in the 2A and 4A materials. It follows that while preexisting dislocation may influence the fracture

behavior other factors like elongation and texture compensate for this so that they have little impart on mechanical properties for the largest amount of strain.

Subgrain Size

The distinction between grains and subgrains is typically determined by the angle of misorentation. Single crystal grains with grain orientations less than 15 degrees are considered subgrains. However, without the aid of TEM or EBSD capable of resolving dislocation structures, it is difficult to determine the exact nature of the grains and subgrains for our ECAE processed materials. However the optical and electron micrographs do provide some insight. The geometric shapes of the grains in the AR optical micrographs indicate that these are recrystallized grains. The presence of etched grain boundaries also suggest these are in fact grains, as this was accomplished through electrolytic etching, which preferentially attacks these areas. The absence of etching differences within the grain interiors suggests that the smaller grains observed in electron micrographs are in fact subgrains. The same holds true for the worked material, with the caveat that working may have produced enough grain boundary misorientation to classify the refined subgrains as grains. However, as these are being compared to the subgrains of the AR tungsten, and the larger grain boundaries are influential in the worked material, smaller grains, will be referred to as subgrains.

The hardness and strength of both AR and ECAE processed polycrystalline tungsten are primarily dictated by the subgrain size. Vickers hardness results clearly

indicate a dependence on subgrain size, through a Hall-Petch type relationship. The yield and ultimate strength at room temperature do not as clearly reflect the contribution of subgrain size, due in part to the brittle nature of tungsten at room temperature, especially the 1A material. The drop in strength for the 1A material can be attributed to its brittle failure prior to yielding seen in stress-strain curves in Figure 26.

The differences in subgrain morphology between the AR and worked materials may also contribute to the differences in fracture mode. In the AR material it was noted that intergranular fracture occurred along the subgrain boundaries. In ECAE processed material these original subgrain boundaries are no longer and have likely been eliminated, as the microstructure was refined. With the elimination of these grain boundaries the low energy intergranular fracture path is no longer available, and transgranular failure dominates. When intergranular failure does occur in worked material, it appears to travel along the deformed grain boundaries, seen in optical microscopy, and propagates through a delamination type failure.

Grain Boundaries

Grain boundaries are another influential feature to the mechanical behavior of polycrystalline tungsten [126, 128, 148]. They have been identified as a cause of mixed mode I/II failure [137, 149]. The increase in fracture energy and ductility of the ECAE processed tungsten can be partially attributed to the elongation and orientation of the grain boundaries. Elongation of the grains improves the grain-to-grain bonding by physically and chemically interlocking the surfaces. Elongation of grains also increases the total grain boundary area up to an estimated 335% with 4A processing [61]. This increase in grain boundary area decreases the concentration of interstitial impurities at the boundaries, which has been cited as a major contributor to brittle failure in tungsten [53, 130-132].

The alignment of these grains also contributes to improved mechanical behavior, by forming a laminated type structure. The formation of these lamella especially along the long axis of the specimen, is the case with the 4A material, and re especially helpful in increasing overall strength, ductility, and fracture energy. The benefit is similar to the behavior of laminated composite structures, where the alignment of the rigid phase is along the principal stress direction. Alignment of the grains also increases the amount of stress required to generate critical voids between lamella that precipitate failure. These voids shown in Figure 42 of the 4A sample tested to ~90% of failure, are formed in-between the tungsten grains and oriented along their length. This arrangement decreases the stress concentration at these voids, as they do not posses a sharp tip aligned

perpendicular to the tensile stress direction. With a smaller stress concentration more energy and deformation is required for these voids to reach a critical size to cause failure. Unlike the 1A material, which has smaller total grain boundary area and a significant portion of the grain boundary oriented normal to the tensile stress direction, allowing for lower energy "opening" between grains. Resulting in lower strength, ductility and fracture energy of the 1A material below the DBTT of the AR material.

This lamellar structure also interferes with crack propagation transverse to this lamella, which can be seen in the numerous micrographs of the fracture plane and surfaces. Figure 55 illustrates how crack propagation is affected by these lamella boundaries. As the crack intersects the lamella boundary it course can be diverted, through either changing crack propagation systems, or through delamination. As each grain boundary may require additional energy to be overcome increases the number of grain boundary crossings may also increase the total energy required for fracture.

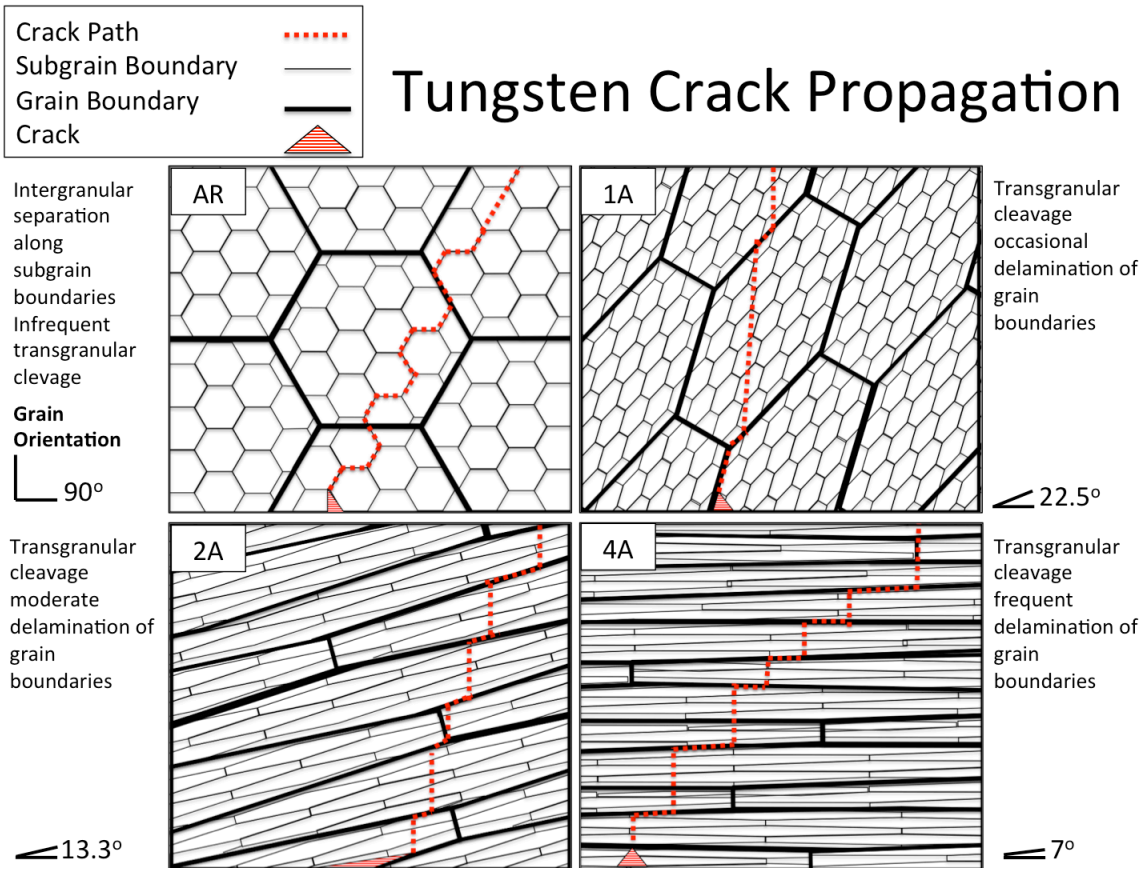

Figure 55. Illustration of crack propagation in as received and ECAE processed polycrystalline tungsten. Plastic strain imparted with each extrusion is ~1.15. Total strain for each material is; AR ~0, 1A 1.15, 2A 2.3, and 4A 4.6. Orientation of tungsten grains in illustration is not to scale. Estimated orientation shown with each illustration.

Texture

The orientation of the tungsten crystals is perhaps the most influential feature of ECAE processing on mechanical behavior [150]. While numerous studies have been conducted on modeling of dislocation interactions in tungsten [146, 151], drawing conclusions from these studies that is easily related to the observed AR and worked tungsten mechanical behavior is difficult. A more useful comparison can be drawn from fracture toughness experiments on tungsten single crystals, which indicate not only the preferred cleavage planes {100} and {110} but also the primary cleavage directions <100> and <110>. Of these, it was shown that the {100} family of cleavage systems has the lowest energy. The difference in fracture toughness between these cleavage systems is attributed to mobility of dislocations in the high stress field near the crack tip, indicating that dislocations have less mobility on the preferred {100} cleavage systems, and greater mobility on less favorable {110} systems [9].

A direct comparison between the single crystal fracture toughness values and fracture energy observations made on ECAE processed tungsten are difficult to make due to the differences in testing methods. However, by normalizing both sets of data by the highest value a comparison can be made based on the relative changes with temperature. The validity of this comparison is based on the same deformation mechanisms for both measurements. In single fracture toughness tests it is blunting of the crack tip though dislocation motion in the high stress field, which can be interpreted as plastic deformation, which is the same mechanism that increases fracture energy.

AS Received (AR) Tungsten Material

Normalized single crystal fracture toughness and as received (AR) fracture energy data are displayed in Figure 56, indicating that the deformation mechanism of the AR material is more similar to that on the {100} family of planes than the {110} family of planes. This result seems logical because AR material is composed of numerous single crystals. The modest mismatch is most likely due to the presence of grain boundaries, and a difference in dislocation density, both of which impede dislocation motion. The relatively lower FE around 24^{o}C-150^{o}C, is due in part to the presence of intergranular fracture, which has a lower energy for crack propagation that is not present in single crystals. The similarity of the AR and single crystal {100} cleavage plane systems above 150^{o}C, can be attributed to the preferred texture of the AR material. Pole figures of the AR material indicate {100} planes are aligned along the x and y-axis, which are oriented with and normal to the tensile stress direction, while the {110} planes have a strong orientation at 45^{o} to these axes. This renders slip or dislocation motion along the {110} planes immobile, as the material fails or deforms along the {100} planes, before the critical resolved shear stress can move dislocations on the {110} planes. This is supported by the similarity between the AR FE and both the {100} and {110} fracture toughness after the DBTT where dislocations are more active, reducing the impact of orientation.

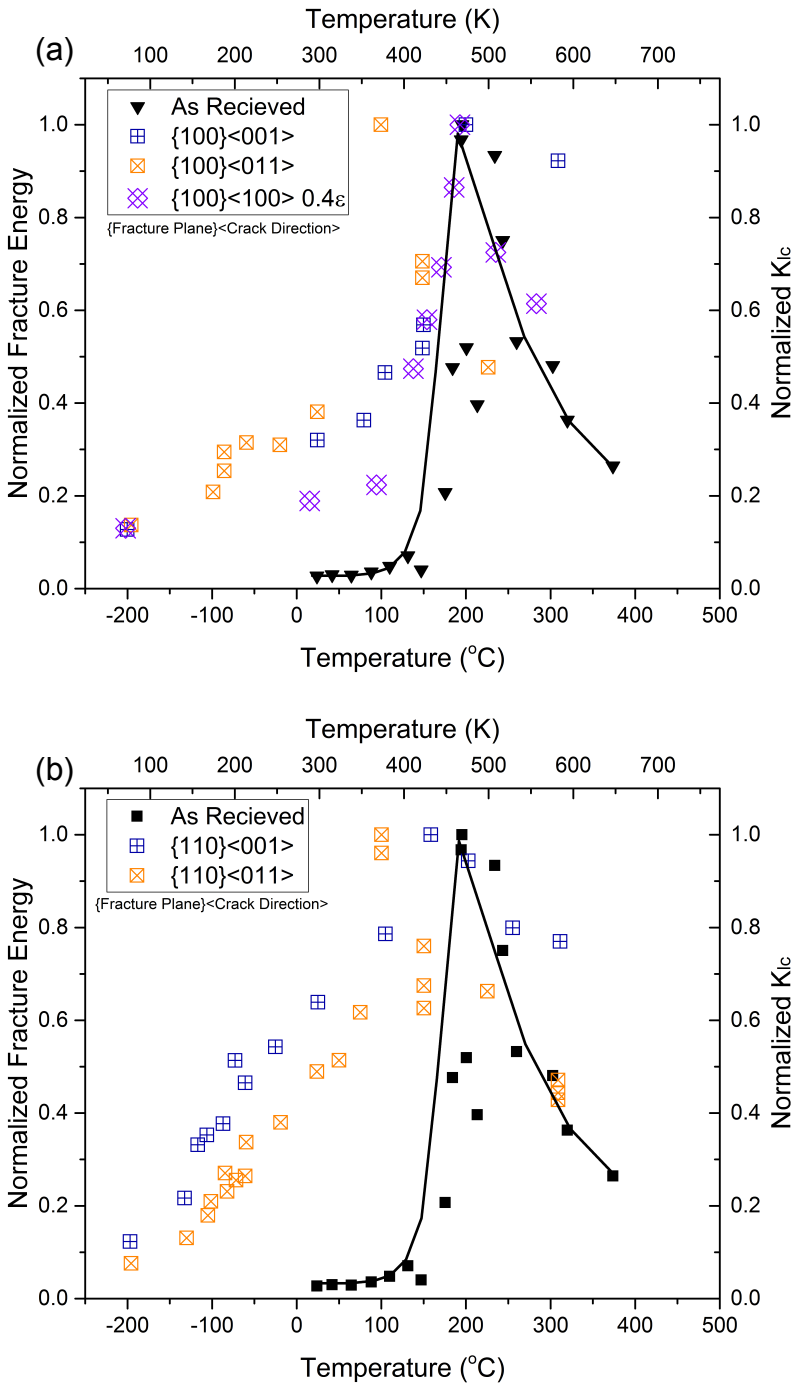

Figure 56. Normalized fracture energy (FE) results (black) as received material and normalized fracture toughness data (other) from single crystal experiments [9]. (a) {100} family crack systems, (b) {110} crack systems. All data normalized by maximum value for each data set.

1A Tungsten Material

The same comparison between normalized FE and fracture toughness for the 1A material is shown in Figure 57. Like the AR material, FE of 1A appears similar to fracture toughness behavior of the {100} planes. The primary difference is the 1A FE curve is shifted to higher temperatures. This shift has been attributed to the presence of a higher dislocation density in worked single crystal [9], and polycrystalline tungsten [147], which decreases dislocation mobility near the high stress field at the crack tip. The similarity between the deformed single crystal results and the 1A material supports this assertion. The presence of grain boundaries may contribute to some of the temperature shift, but texture is possibly the dominating factor. As pole figures of 1A material indicate, the {100} planes are oriented in the y-axis normal the tensile stress, and the {110} planes are aligned in the z direction. This results in a very limited number of slip systems and likely decreases the ductility and FE of 1A material substantially.

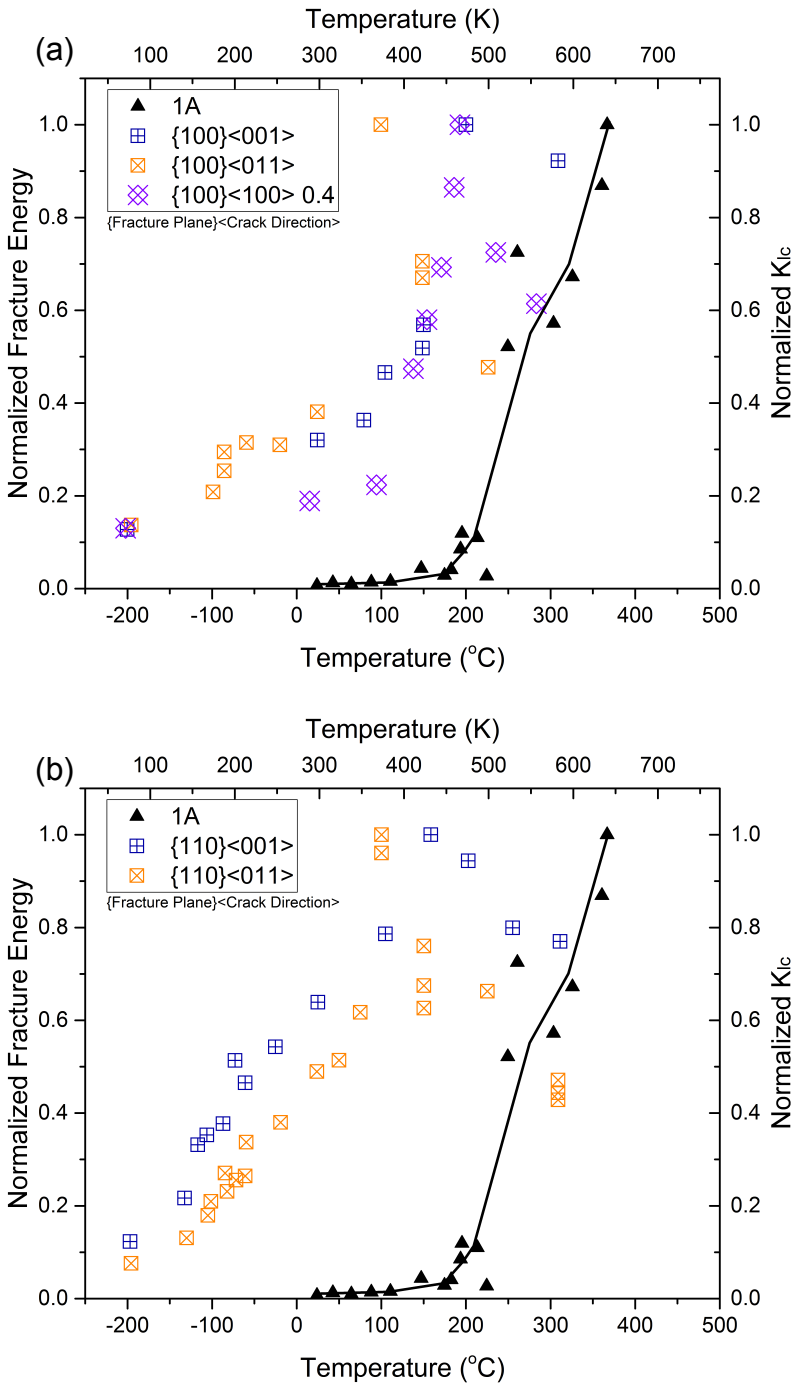

Figure 57. Normalized fracture energy (FE) results (black) for 1A material and normalized fracture toughness data (other) from single crystal experiments [9]. (a) {100} family crack systems, (b) {110} crack systems. All data normalized by maximum value for each data set.

2A Tungsten

The fracture energy of the 2A material also favors the {100} family of cleavage systems as shown, displayed in Figure 58, and is more similar to the normalized {100} fracture toughness values than either the 1A or AR material. This comparison is especially convincing by the overlap in the peak FE of 2A material and single crystal fracture toughness near 200^{o}C. Like the AR and 1A texture results indicate, this behavior is due to the orientation of the {100} and {110} planes. For the 2A material the {100} planes are only slightly misaligned with the x-axis by ~13^{o}, while the {110} planes are oriented by approximately the same amount from the y-axis. This texture promotes slip on the {100} planes and limits it on the {110}.

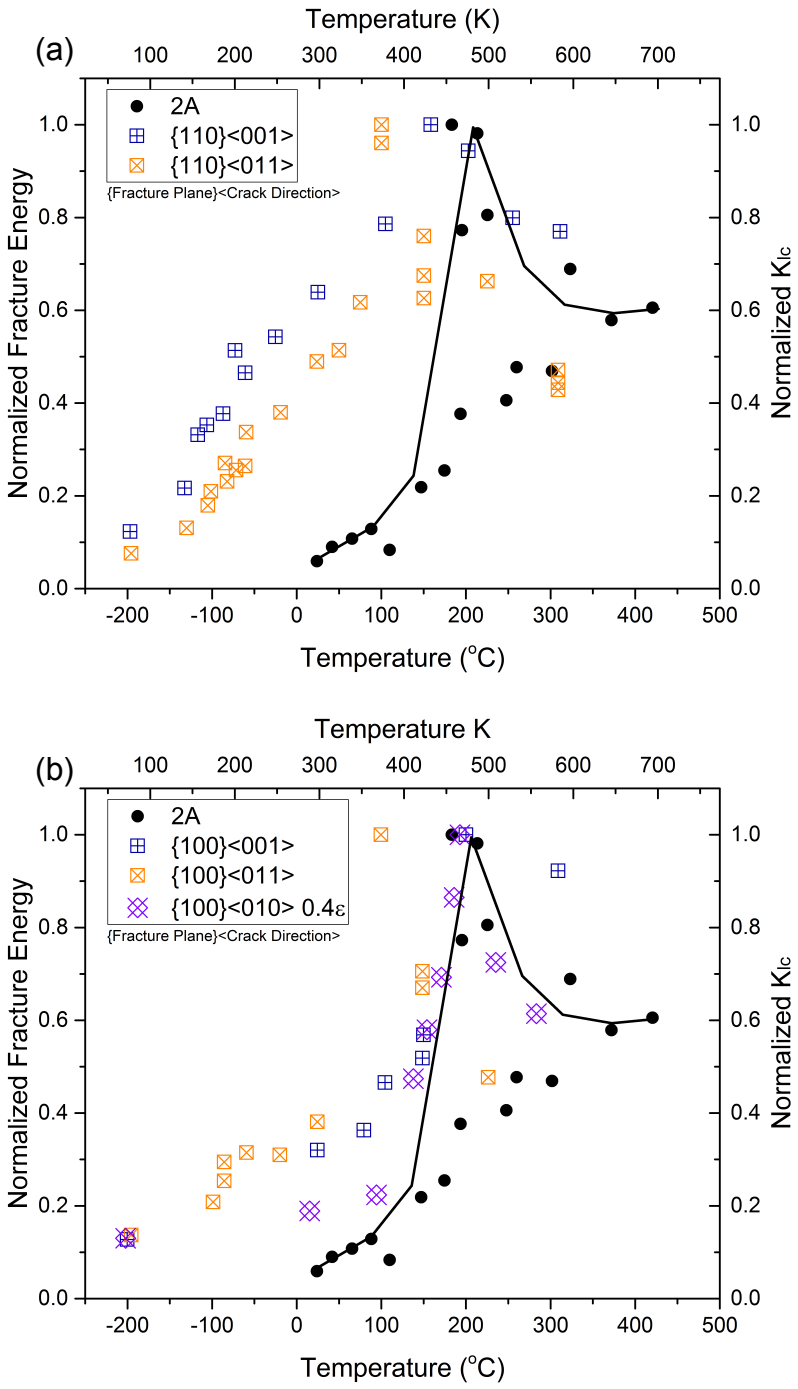

Figure 58. Normalized fracture energy (FE) results (black) on 2A material and normalized fracture toughness data (other) from single crystal experiments [9]. (a) {100} family crack systems, (b) {110} crack systems. All data normalized by maximum value for each data set.

4A Tungsten

Unlike the other test cases, the FE of 4A tungsten behaves like the {110} cleavage systems. This can be attributed to the strong x and y-axis orientation of the {110} planes. The {100} planes are nearly aligned with the x-axis, however, it appears that they are inactive when the {110} slip systems are available. These results agree with numerous investigations on tungsten wires and sheets, which show a high degree of {110} -fiber, texture orientation along the principal axis [42, 136]. The ductility of the 4A material, even at -45^{o}C, can be attributed to a constant increase in fracture toughness seen in the {110} cleavage plane systems, and therefore dislocation mobility on those planes. Some of the increase in FE with 4A processing may also be due to this texture as it was shown that these crack system had nearly twice the room temperature fracture toughness than the {100} systems in single crystals [9].

The fact that dislocations only become active in high stress fields may also cause the work hardening behavior seen in the worked material and especially the 4A material. As the stress was only large enough to induce dislocation motion at the center of the bend specimen, thus causing only localized deformation and thus the smaller bent region.

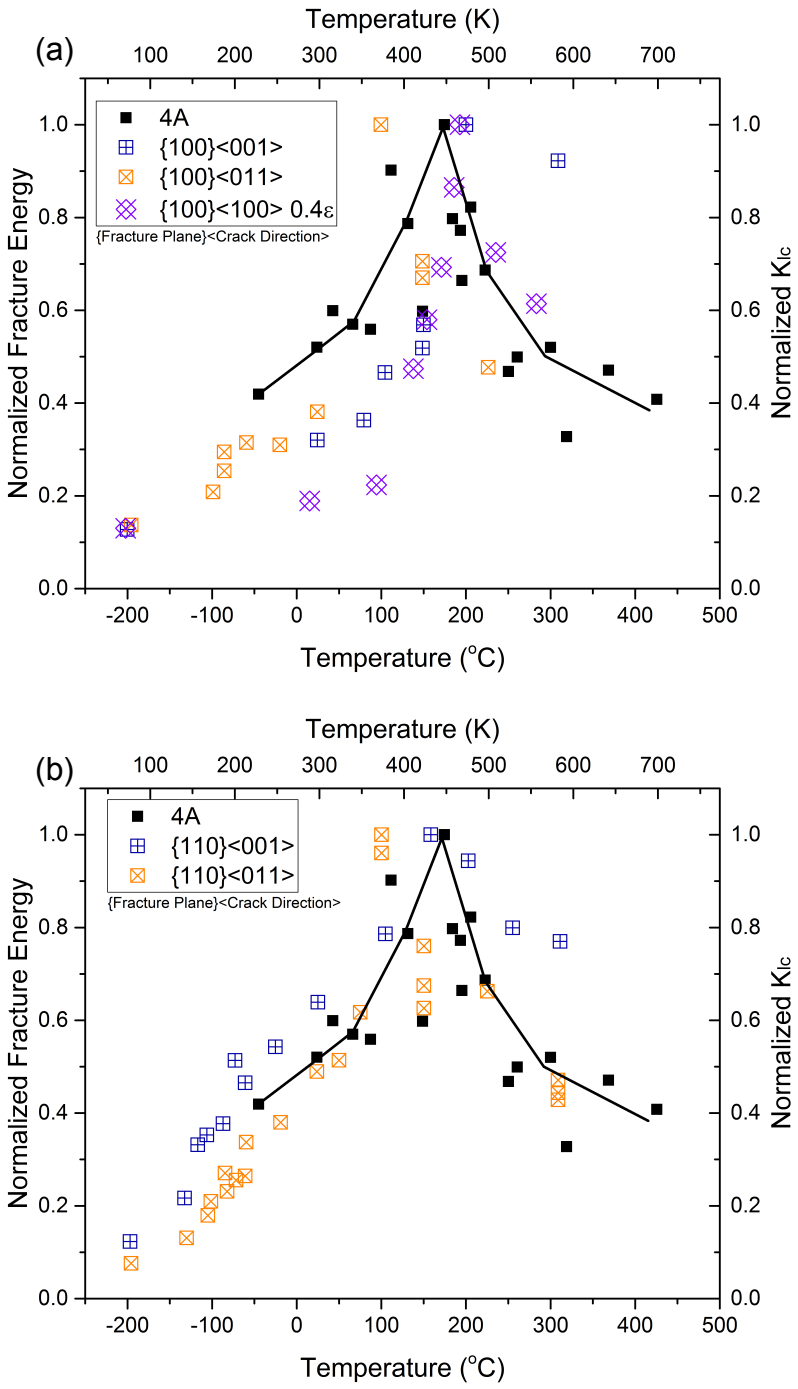

Figure 59. Normalized fracture energy (FE) results (black) 4A material and normalized fracture toughness data (other) from single crystal experiments [9]. (a) {100} family crack systems, (b) {110} crack systems. All data normalized by maximum value for each data set.

Strain Area

A concern when using bend testing to evaluate mechanical behavior is the small volume of material subjected to the maximum stress. Unlike a tensile specimen where the stress is distributed across the entire cross section only a thin layer on the bottom edge of the bend specimen is subjected to the highest stress. This makes translating results to bulk material problematic, as a size effect where large defects present in the bulk material are excluded from the tested region, artificially improving the results, may be partially responsible for the mechanical behavior.

The greatest concerns about possible size effects are for the 4A material near ambient temperatures, due to its high ductility, and the smaller deformed region visible in Figure 29 of optical micrographs. The other test cases are too brittle at ambient temperature for this to be an issue, and at higher temperature all materials are sufficiently ductile that defects are less critical.

In order to evaluate this, a simple iterative nearest neighbor averaging scheme was used to attain a first order estimation of the strain field. For this method a representative grid of the bend specimens was created where each cell was determined by the average values of its top, bottom left and right neighbors. Boundary conditions were chosen to be the highest tensile strain and compressive strain measured by hand located at the bottom and top cell in the middle of the grid, and zero strain values at half the span length from the center. The model was then solved in an iterative manner until the values converged. The results of this are shown in Figure 60.

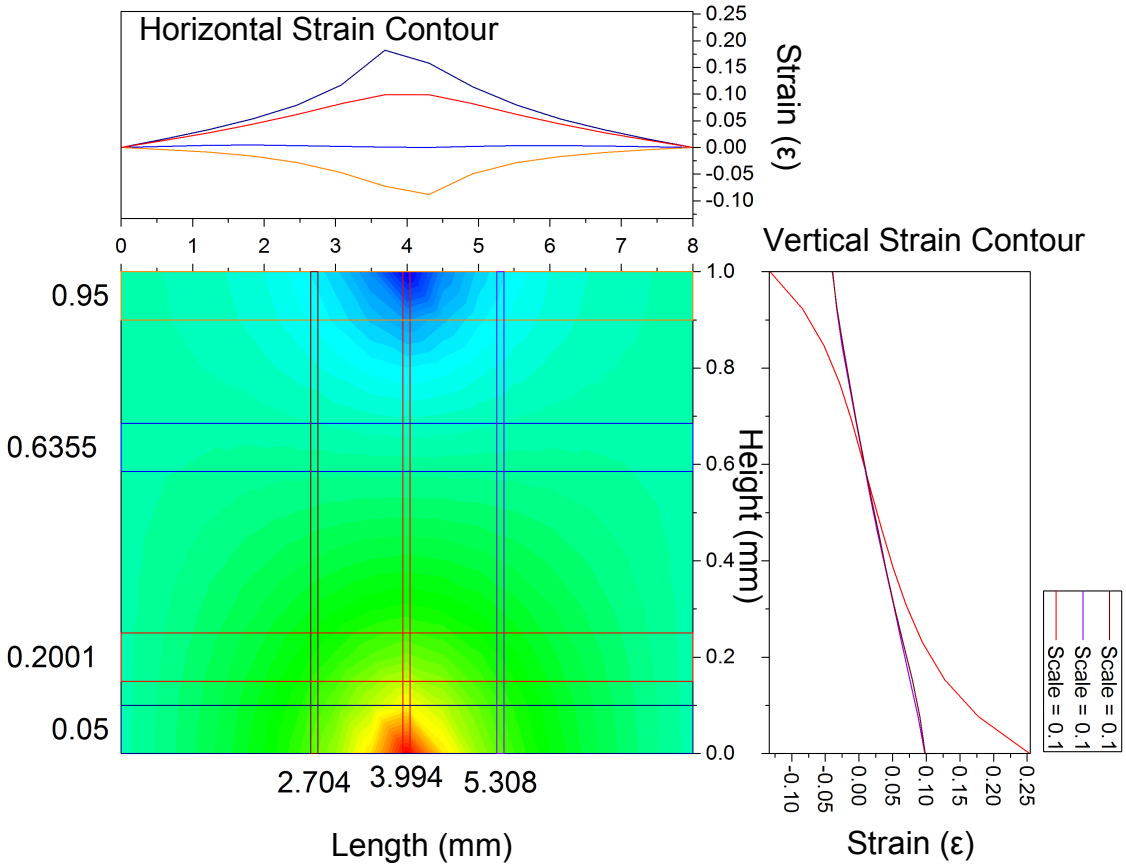

Figure 60. Estimated strain profile of 4A test specimen evaluated by 3-point bending at 24°C. Values calculated by iterative calculation based on nearest neighbor average. The boundary conditions used in this estimation are zero strain at right and left boundary (-3.5,y) and (3.5,y), and the manual measured tension and compress strain values of, 0.2560ε at (0,0) and -0.134 ε at (0,1). This estimation was only used for a first order approximation of the strained area and is not necessarily an accurate representation of the strain profile.

In this figure the estimated strain field is visualized for the region stressed by bend testing. Vertical lines at x=2.7 and 5.3 mm and the horizontal line at y=0.2mm indicate the boundary of the region with 10% strain. The strain contour of horizontal lines at y=0.05, 0.2, 0.64, and 0.95mm are shown above the main contour map in the

figure labeled horizontal strain contour. The strain contour of the vertical line at x=2.7, 4, and 5.3 mm are shown to the right of the main contour map, labeled vertical strain contour. The x=2.7 and 5.3mm contours overlap in this figure and appear linear, while the vertical line at the center is curved. From this graph it is estimated that the zero strain occurs at approximately 0.64mm from the bottom surface. These results also indicate that the region with strain in excess of 10% is approximately 0.82mm^2, and occupying a semicircular region centered at the bottom of the specimen extending 0.22 mm high and 2.6mm in length.

While this region is small, the notched 4A specimen, shown in Figure 35 indicates little, notch sensitivity and size effect, as the notched sample retained significant ductility ~8% despite the presence of a large surface stress concentration. The presence of this notch indicates that even with a defect, the 4A material still possesses significant ductility.

Error

The quantification and minimization of error is of great importance in thorough experimental scientific research, especially when dealing with materials where properties are sensitive to small variations in composition and microstructure. The complex and extensive nature of this work provided many opportunities to deal with the issues surrounding error analysis. The two most predominate areas were temperature and

grain size measurements. Issues regarding the error for these two quantities are discussed at length here.

Temperature

The process for temperature measurement of the three-point bend testing was described previously in the procedure section of this manuscript. A great deal of effort was taken in order to accurately determine the specimen temperature. To do this a correlation between the furnace air temperature near the three-point bend apparatus and a sacrificial test specimen was established. As mechanical behavior changes the most dramatically below the transition temperature, establishing this correlation was focused on the 24^{o}C-300^{o}C-temperature range. The correlation was then extrapolated to higher temperatures where mechanical behavior varies less. Because this approach estimates values outside of the measured data, the amount of uncertainty increases with temperature above this range, and is noted by the 95% confidence and prediction bands in Figure 61.

Near the DBTT the uncertainty in temperature is very small falling within the 95% confidence interval, which at these temperatures as approximately 10^{o}C. Near 300^{o}C the data points fall outside the Confidence interval but still within the 95% prediction band, with an uncertainty closer to 30^{o}C. However above the DBTT the uncertainty in temperature is less important as the changes in mechanical behavior are less dramatic.

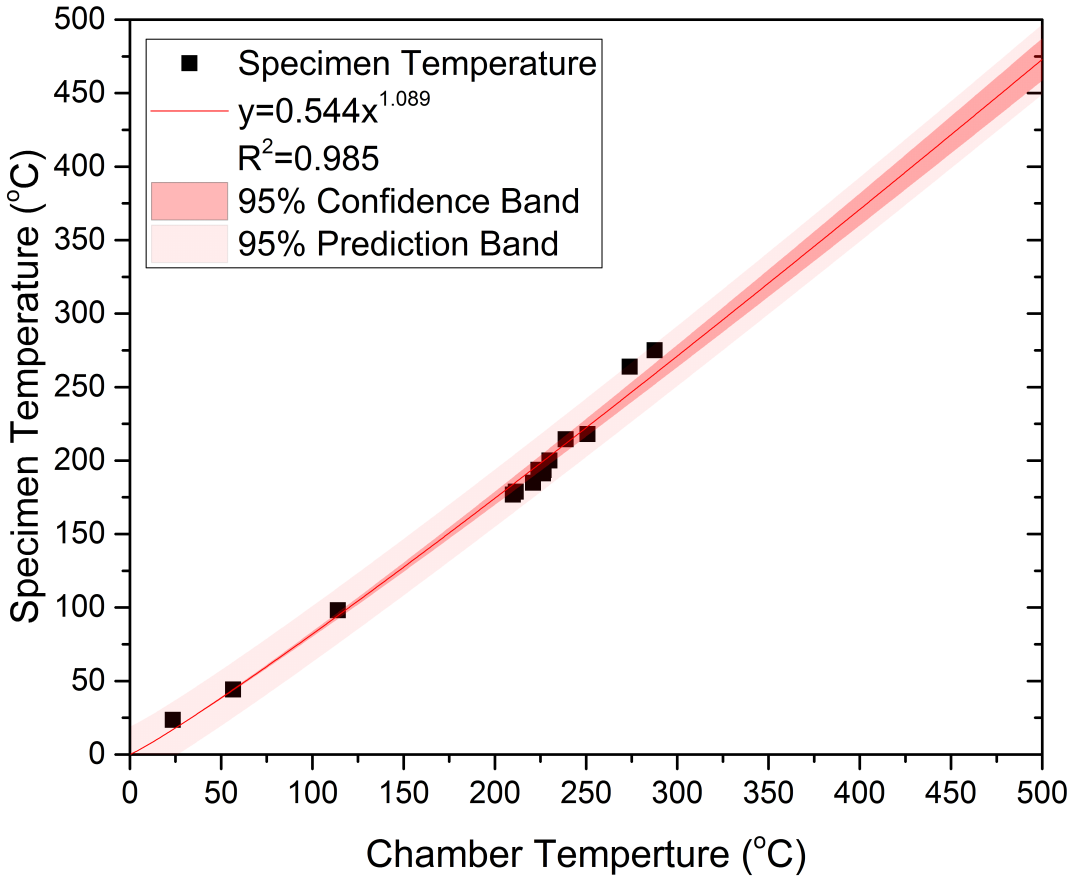

Figure 61 Specimen and chamber temperature data with exponential fit of data indicating 95% confidence band and 95% prediction bands, indicating uncertainty in temperature calibration.

Grain Size

Determining grain size is a complicated task. Grain size can be estimated directly through the use of X-ray diffraction but the values are only valid for very small grain sizes. However, methods based on microscopy have the fundamental flaw of being based on a random cross section of grains. The flaw stems from the fact that micrographs depict a random cross section of grains, which when measured and analyzed will produce smaller average values and larger standard deviations than the actual values. This is due to the fact that through random cross sectioning, grains are viewed as truncated and not at their widest points. The possible underestimation in grain size and overestimation of standard deviation can be seen in an example of random truncation of spheres. For this example assume that a material is composed of spherical grains with a radius of 1. Each grain would be randomly cross-sectioned on this micrograph. The distance from the grain surface, which can be thought of as the depth of truncation, h, determines the radius of each grain measured. This radius can be found through the use of Equation 14 which can be derived with the Pythagorean theorem derived from Figure 62.

Equation 14 $\boldsymbol{a = \sqrt{h(2R - h)}}$

Where *a* is the radius of the circular cross section, *R* is the radius of the sphere, and *h* is the distance from the surface.

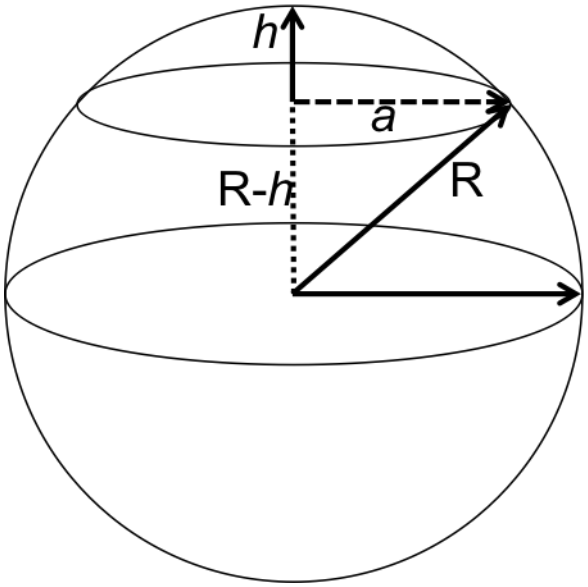

Figure 62. Radius determinations of cross sectional area for sphere with radius R at depth *h* from surface.

Using this formula the effect of random cross section can be demonstrated. Assuming the grains are composed of these spherical grains with a radius of 1 and *h* values are randomly distributed between 0-1. A series of 10,000 *h* values produces an average radius of μ_r=0.79 and a standard deviation σ=0.22, a 20% difference from the actual mean. In actual material this difference will be more difficult to quantify, as the grains will not be uniform. While this flaw in characterization is known, this method for evaluation is common thus a comparison can be made between investigations.

Subgrain Measurements

Measuring grain size with micrographs can be done in several ways. The average subgrain diameter is reported in this work. This value was determined by first measuring each subgrain at its longest point, followed by measuring the largest width normal to first measurement. Each subrain diameter is then determined by averaging those values together, and the average subgrain diameter is determined by the mean value off all measured diameters. One advantage of this method is the smaller standard deviation and ability to calculate individual grain aspect ratios. The disadvantage of this method is it is very time consuming and laborious. Therefore a major concern for the researcher should be human error and unintentional bias of results. A good check for any bias or human error is to examine data in the order in which it is collected. Examples of the average subgrain diameter for AR and 4A materials are shown in Figure 63.

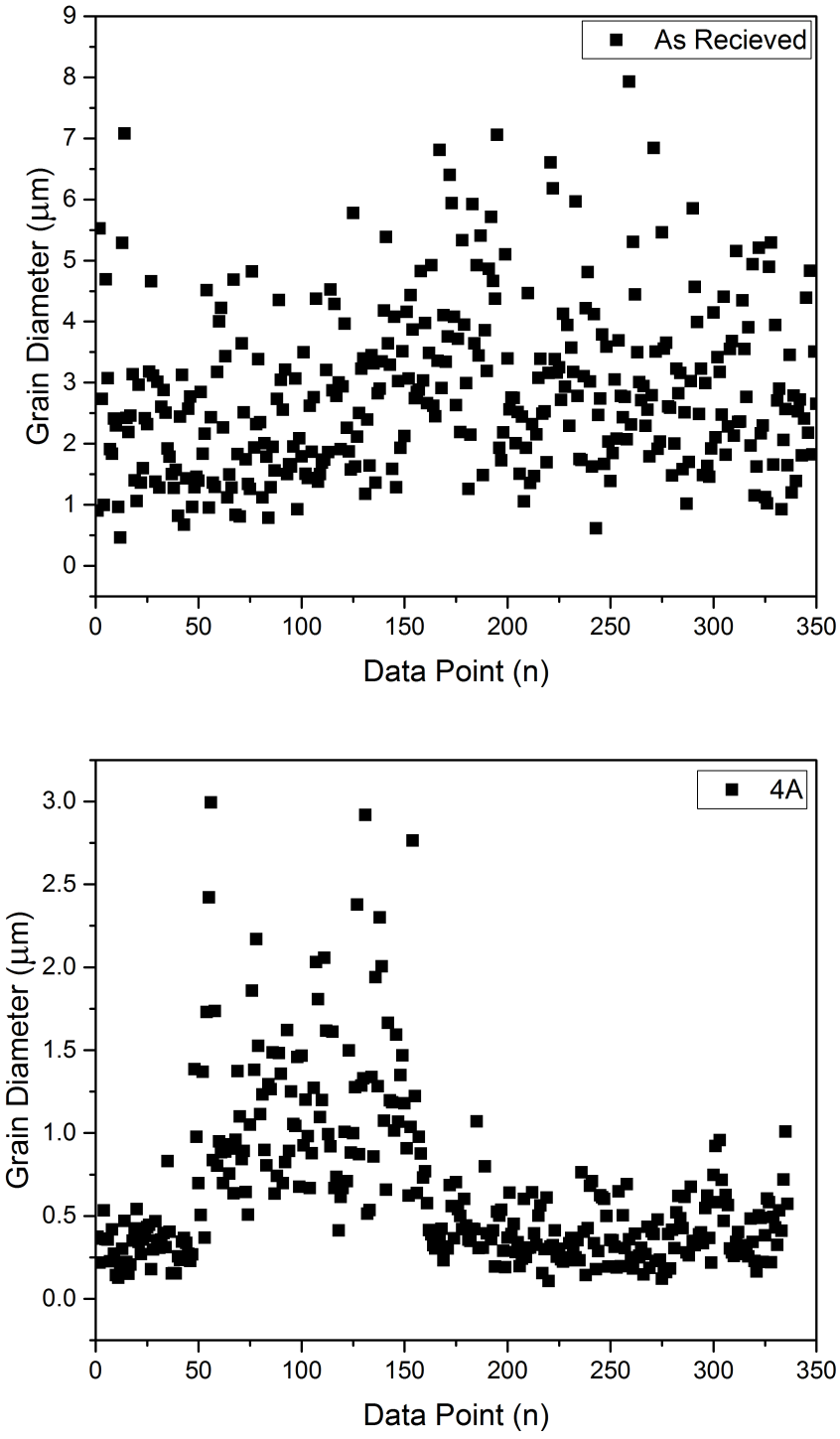

Figure 63. Average subgrain diameter data for AR and 4A materials. Data displayed in the order of measurement.

As can be seen in Figure 63, the AR data appears to center between 1-3 μm, while in the 4A data most of the data is between 0-0.5μm, while some of the data between points 50 and 150 centers around 1 μm. This difference can be attributed to the differences in magnification between micrographs. At higher magnification larger subgrains tend to be excluded while at lower magnification smaller grains cannot be clearly distinguished. This difference in magnification levels is not present in AR material, because the subgrains are relatively large and easy to distinguish at high and low magnification. If some bias were present a general trend in the data might be expected. For instance, if the values continually increase of decrease with each data point.

As this measurement method is time consuming and a human bias can occur sample size should not be arbitrarily determined. For this work, the sample size was determined by the following criteria: the standard error Equation 15, should be less than 5% of the mean grain size μ. In equation form it appears as Equation 16.

Equation 15 $\mathbf{SE} = \frac{\boldsymbol{\sigma}}{\sqrt{\boldsymbol{n}}}$

Equation 16 $\frac{\boldsymbol{\sigma}}{\sqrt{\boldsymbol{n}}} \leq \mathbf{0.05} \times \boldsymbol{\mu}$

Where n in the sample size, σ is the standard deviation, and μ is the arithmetic mean. The basis for this criteria is that while the mean value will fluctuate, after a certain point its value is relatively stable, and the same is true for the standard deviation. However it is typically more sensitive to sample size. Using the standard error provides a means to estimate sample size in terms of mean and standard deviation, so a sufficient amount of data can be collected. The response of average grain diameter and standard error with increasing sample size can be seen in Figure 64, for AR and 4A materials.

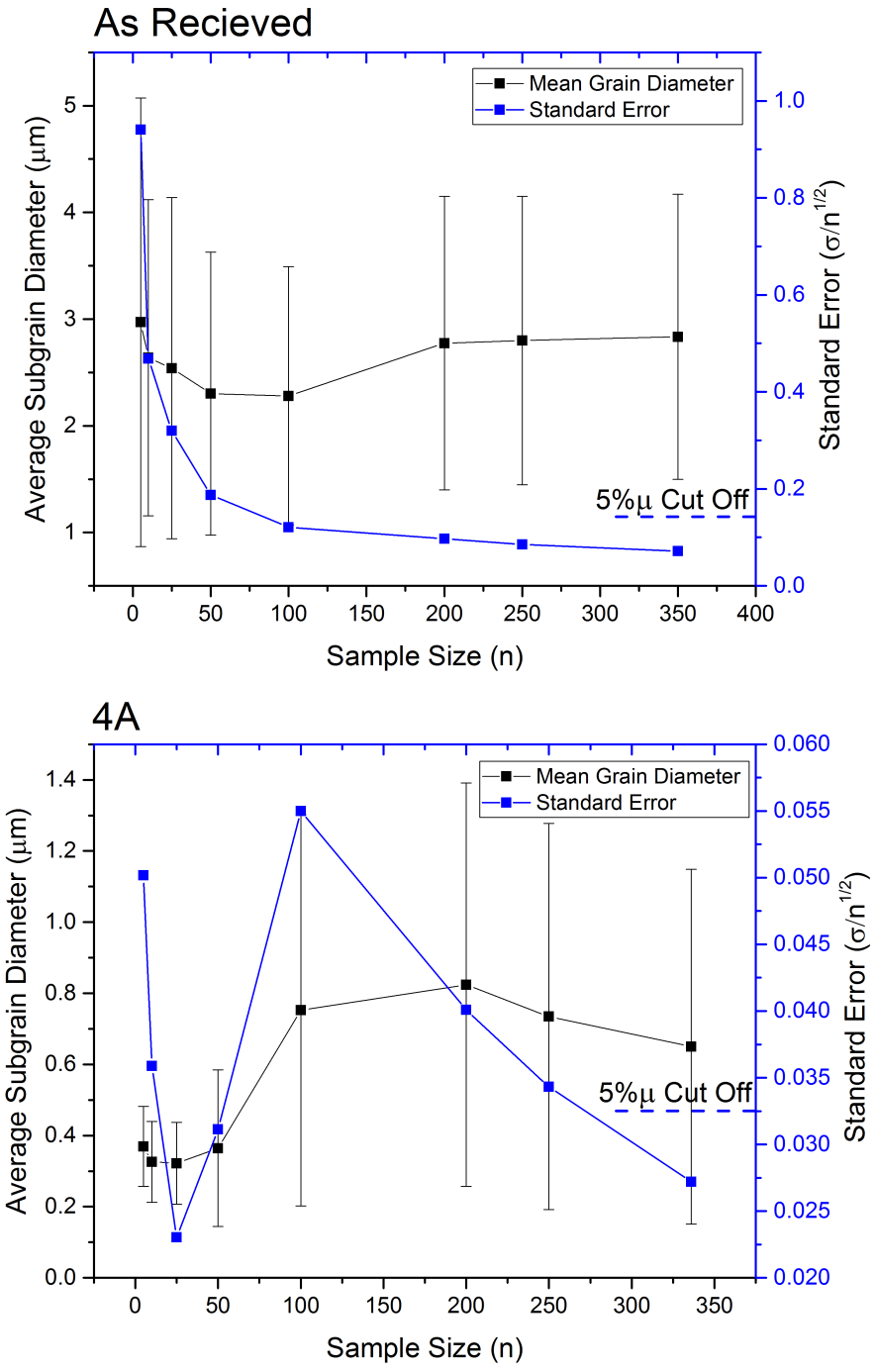

Figure 64. Average subgrain diameter and standard error values of increasing sample sizes for AR and 4A material. Black points represent average subgrain diameter and error bars indicate standard deviation. Blue points indicate standard error, 5% of μ shown by dashed line.

In the AR material the mean grain size is relatively stable while the standard error decreases rapidly up to a sample size of 100. This is due in part to the uniform size, and shape of the AR subgrains. The average subgrain diameter for the 4A material is small ~0.3 μm, for n<100, but doubles at larger sample sizes. This increase can be directly attributed to the differences in visible grain sizes caused by changes in magnification level. The difference in magnification causes the standard deviation to increase and with it, the standard error. It is only when the sample size is greater than 300 does the standard error meet the aforementioned criteria. At this point the average values are relatively stable indicating the validity of this method.

Grain Size

Another problem with determining grain size is the use of the arithmetic mean to calculate its value. This is based on the assumption that the data is normally distributed, and for material with large grains the assumption is fairly valid. However as grain sizes approach 1 μm, a normal distribution can no longer be assumed, as grains sizes cannot be negative. As noted in the tungsten grain size results, the average subgrain diameters have a more lognormal distribution, than normal distribution, which is to say they posses a normal distribution in the log scale. A problem with using a lognormal distribution to characterize microstructure is that determining and representing the standard deviation is difficult as it is a log scale. In Table 5 the differences between the average subgrain size measurements is summarized for the different tungsten processing conditions.

Table 5 Comparison between mean values calculation methods for average subgrain diameter measurements.

Material	Normal mean	Lognormal mean	% Difference
AR	2.83	2.53	11
1A	0.902	0.75	16
2A	0.73	0.62	15
4A	0.65	0.51	21

While the differences between the normal and lognormal means are relatively small for larger subgrains, for smaller subgrains it becomes substantial. This is important as microstructure is often attributed to changes in mechanical behavior. A prime example would be the Hall-Petch relationship. Seen in Figure 65, is the Hall-Petch relationship for the normal and lognormal grain sizes with Vickers hardness.

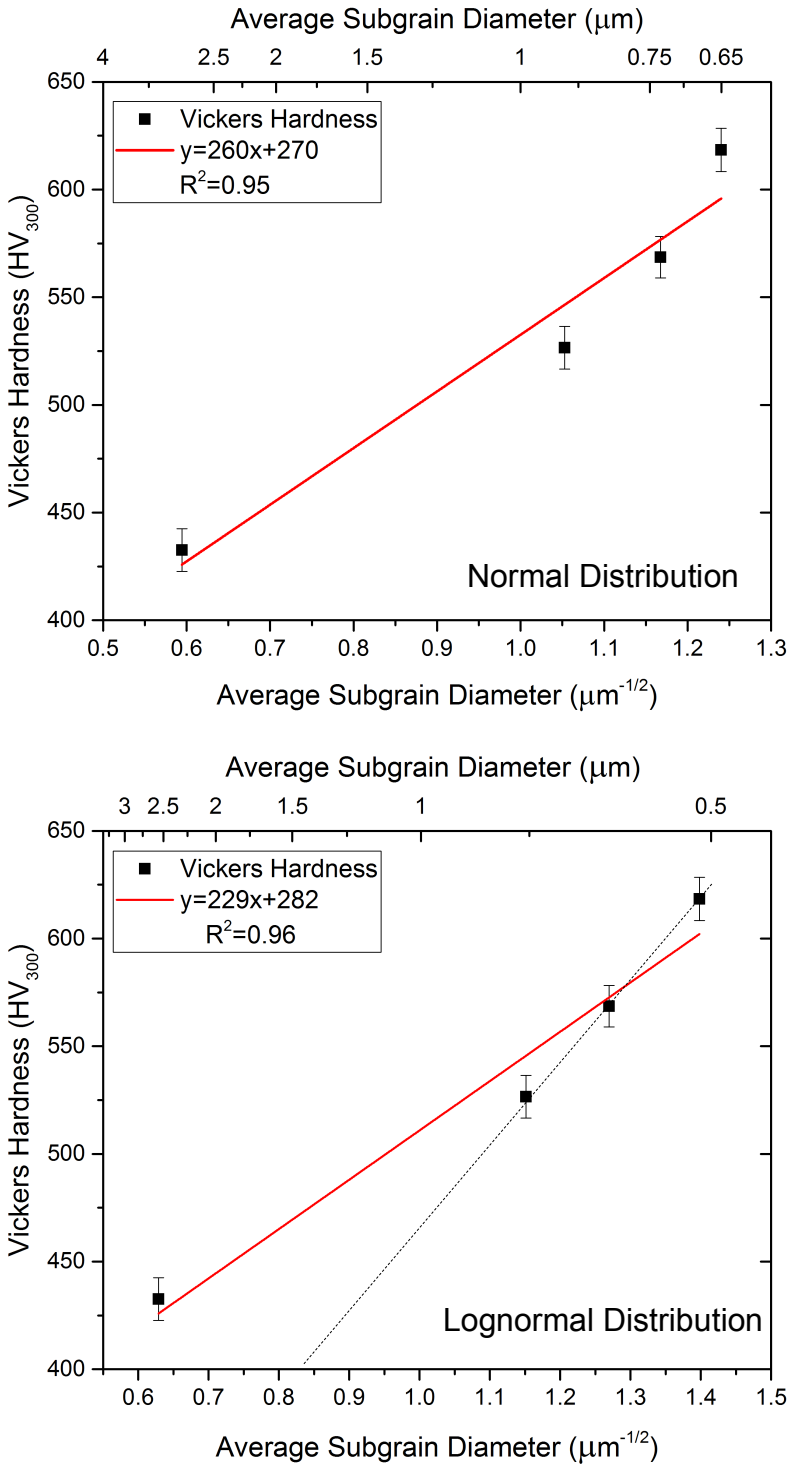

Figure 65. Hall-Petch plots for subgrain size determined by normal and lognormal distributions and Vickers hardness measurements.

The differences between these Hall-Petch equations are relativity small with the normal values being VH_{300}=260x+270 and the lognormal are VH_{300}=229x+282. More interestingly, the lognormal values of the worked tungsten appear to be very linear, but do not coincide with the AR data point at the bottom left of the graph. . This could indicate a fundamental difference in deformation in either heavily dislocated or very fine-grained tungsten, or possible problems using with the Hall-Petch equation as discussed in the work [152]. However, due to the scarcity of data no clear conclusion can be determined.

CHAPTER VII

SUMMARY AND CONCLUSION

Summary

The goal of this work was to increase tensile ductility of bulk polycrystalline tungsten to over 10% at ambient temperature. In doing this, a better understanding of mechanisms and microstructure features that influence changes in mechanical behavior was developed, producing greater knowledge for improved tungsten processing efforts and materials with improved ductility.

Processing was conducted on 12 mm diameter commercially pure tungsten rods encased in 25.4mm square 304 stainless steel cans ECAE extruded at 320^{o}C through a 90^{o} die angle with sliding walls. All samples were prepared by sectioning with electrical discharge machining, followed by mechanical and the electrolytic-polishing. Optical and scanning electron microscopy (SEM) were used to evaluate the effects of ECAE processing on microstructure and failure mechanisms. Texture of the as received (AR) and ECAE processed tungsten was completed through x-ray diffraction analysis. Mechanical behavior was analyzed through 3-point bend tests using a 7mm bottom support span, on 1x2x14mm^3 test specimens oriented along the extrusion direction. The load displacement data from these tests were converted into stress versus strain through 3-point bend test equations; the yield strength (YS), ultimate flexural strength (UFS), and ductility were determined from these stress-strain curves. The fracture energy (FE)

was determined by integrating the load displacement data and dividing by the cross sectional area of the respective samples. The ductile-to-brittle transition temperature (DBTT) was determined by evaluation of the location of the peak in fracture energy-temperature curve. The hardness of the tungsten samples along the flow plane of extrusion, was measured by a Vickers hardness apparatus using a 300g load.

Microscopy revealed a reduction in subgrain size with each successive ECAE operation. After four extrusions the initial 2.8μm diameter subgrains were refined to ~0.65μm, a 77% size reduction. The same processing produced tungsten with 19% ductility at room temperature, an enormous increase from the AR material. This was accompanied by a 50% increase in yield strength, a 94% increase in ultimate flexural strength, and a 44% increase in hardness. The energy required to fracture route 4A material increased over 50x compared to the AR tungsten rod. The increases in strength, ductility, and fracture energy were accompanied by a decrease in the DBTT, from ~210^{o}C in AR material to ~170^{o}C in 4A.

The 24^{o}C observations of tungsten materials evaluated in this work are summarized in Table 6. Vickers hardness results indicate a Hall-Petch type dependence on grain size in polycrystalline tungsten. The 1A material was 50% less ductile than AR material at 24^{o}C. This lack of ductility caused premature fracture, a 50% decrease in strength, and a 71% decrease in fracture energy. The brittle nature of the 1A also caused the DBTT to increase to over 370^{o}C.

Working improved the mechanical behavior of the 2A material. At room temperature 2A material possessed 130% greater ductility than the as received along

with 14% greater yield strength, 27% greater ultimate flexural strength, and required 286% more energy per square millimeter to fracture all of this with a similar ductile to brittle transition temperature.

The ductility of all materials increased as the temperature approached the ductile-to-brittle transition temperature. Above the DBTT the as received material became notably more ductile; the increase in ductility of the 1A and 2A material slowed or became constant, while the 4A material became less ductile. This behavior was reflected by a similar increase in fracture energy for each material.

Temperature also altered the failure mechanisms in each tungsten material. In the as received material increasing temperature increased the proportion of transgranular failure to intergranular failure, seen in micrographs as well as the decrease in crack deflection angle. In worked material and especially the 4A material, a higher temperature caused an increase in delamination type failure, which increased the crack deflection angle.

Table 6. Summary of room temperature measurements of as received and ECAE processed pure tungsten.

Process	Subgrain Diameter µm	Ductility %	VH 300	YS MPa	UFS MPa	FE mJ/mm^2	DBTT ^oC
AR	2.83±1.3	1±0.9	430±10	N/A	2010±260	7±1	210
1A	0.90±0.6	0.5±0.2	530±10	N/A	940±100	2±0.4	370
2A	0.73±0.5	2.3±2.5	570±10	2290±290	2550±470	27±35	200
4A	0.65±0.5	19.4±2.7	620±10	3000±670	3900±360	400±160	170

Conclusions

From the results obtained it is concluded:

1. The lack of fracture during processing is likely due to the slow processing speed, the hydrostatic stress exerted by the stainless steel encapsulated, the use of route A, and the ECAE processing method design (sliding walls). The use of sliding walls and sample encapsulation limited tensile stress exerted on the material and helped prevent a fracture during processing.
2. Texture and specifically the orientation of the {110} planes, is largely responsible for the increase in ductility observed in the 4A material.
3. Microscopy and texture results indicate that Route A ECAE processing most likely produces significant mechanical anisotropy in the material.
4. Reducing anisotropy may be possible through alternate ECAE processing routes or through combinations of other processing techniques such as swaging, area reduction extrusion, and rolling.
5. Procedures that impart a {100} texture in the tensile stress direction will improve ductility.
6. The activity of dislocations near the crack tip causing blunting in single crystal tungsten is likely similar to that responsible for plastic deformation in heavily worked polycrystalline tungsten.

7. Strain hardening at elevated temperatures in polycrystalline tungsten is decreased through severe plastic deformation processing because of grain size refinement, and the presence of numerous dislocations.
8. Hardness of heavily worked polycrystalline tungsten can be primarily attributed to the refinement of subgrains, but the presence of dislocation may provide some increase from the as received material.
9. The fracture energy is not significantly impacted by the fracturing and crack propagation events. These occur very rapidly and therefore do not have the opportunity to absorb significant amounts of energy during failure.
10. Grain boundary elongation provides some resistance to fracture though the formation of an elongated lamella type structure which prevents the formation and growth of cracks that cause failure.
11. Subgrain size does not have a significant impact on ductility.
12. Cold working though ECAE route A of tungsten eliminates intergranular separation of subgrain boundaries as a failure mode in tungsten.
13. The capacity for ductile behavior of the 4A material is most likely due to a combination of microstructural changes with processing. Microstructural changes like refinement of subgrains and the elongation of grain boundaries increased the robustness of the tungsten so that failure did not occur prior plastic deformation, and the stress required for plastic deformation was reduced by the {110} texturing.

CHAPTER VII

FUTURE WORK

Key areas of future work are to refine the processing techniques and investigate material anisotropy. A primary topic to focus on will be to investigate the annealing and recrystallization behavior, as improved understanding of these may provide greater flexibility in processing and improved mechanical behavior.

REFERENCES

1. Lassner, E. and W.-D. Schubert, *Tungsten: properties, chemistry, technology of the elements, alloys, and chemical compounds*. 1999, New York, New York, Springer Science & Business Media.

2. Hirai, T., et al., *ITER tungsten divertor design development and qualification program.* Fusion Engineering and Design, 2013. **88**(9–10): p. 1798-1801.

3. Cai, W.D., et al., *A review of tungsten-based alloys as kinetic energy penetrator materials.* Reviews in Particulate Materials, 1995. **3**: p. 71-131.

4. Pappu, S., et al., *Deformation twins in oriented, columnar-grained tungsten rod ballistic penetrators.* Materials Science and Engineering: A, 2001. **298**(1–2): p. 144-157.

5. Upadhyaya, A., *Processing strategy for consolidating tungsten heavy alloys for ordnance applications.* Materials Chemistry and Physics, 2001. **67**(1–3): p. 101-110.

6. Coolidge, W.D., *Tungsten and method of making the same for use as filaments of incandescent electric lamps and for other purposes*. 1913, Google Patents.

7. Jeffries, Z., *Metallography of tungsten.* Transactions of the American Institute of Mining and Metallurgical Engineers, 1919. **60**: p. 588-643.

8. Schoenfeld, W. J., *Tungsten sheet rolling program.* Universal Cyclops Steel Corp, Bridgeville, PA, 1963.

9. Riedle, J., et al., *Fracture studies of tungsten single-crystals.* Materials Letters, 1994. **20**(5-6): p. 311-317.

10. Gumbsch, P., et al., *Controlling factors for the brittle-to-ductile transition in tungsten single crystals.* Science, 1998. **282**(5392): p. 1293-1295.

11. Riedle, J., P. Gumbsch, and H.F. Fischmeister, *Cleavage anisotropy in tungsten single crystals.* Physical Review Letters, 1996. **76**(19): p. 3594-3597.

12. Zhang, Y., et al., *Influence of HPT deformation temperature on microstructures and thermal stability of ultrafine-grained tungsten*, in *Nanomaterials by Severe Plastic Deformation Iv, Pts 1 and 2*, Y. Estrin and H.J. Maier, Editors. 2008, Trans Tech Publications Ltd: Stafa-Zurich. p. 1000-1005.

13. Wei, Q., et al., *Microstructure and mechanical properties of super-strong nanocrystalline tungsten processed by high-pressure torsion.* Acta Materialia, 2006. **54**(15): p. 4079-4089.

14. Alexandrov, I., et al., *Ultrafine-grained tungsten produced by SPD techniques.* Ultrafine Grained Materials II, 2002: p. 199-208.

15. Yuan, H., et al., *Strengthening and toughening effect on tungsten subjected to multiple ECAP*, in *Nanomaterials by Severe Plastic Deformation: Nanospd5, Pts 1 and 2*, J.T. Wang, R.B. Figueiredo, and T.G. Langdon, Editors. 2011, Trans Tech Publications Ltd: Stafa-Zurich. p. 701-706.

16. Hao, T., et al., *Microstructures and properties of ultrafine-grained tungsten produced by equal-channel angular pressing at low temperatures.* Journal of Nuclear Materials, 2013. **433**(1-3): p. 351-356.

17. Hao, T., et al., *Strength and ductility improvement of ultrafine-grained tungsten produced by equal-channel angular pressing.* Journal of Nuclear Materials, 2014. **455**(1-3): p. 595-599.

18. Mathaudhu, S., K. Hartwig, and L. Kecskes, *Microstructures and recrystallization behavior of severely hot-deformed tungsten.* Materials Science and Engineering: A, 2009. **503**(1): p. 28-31.

19. Wei, Q. and L.J. Kecskes, *Effect of low-temperature rolling on the tensile behavior of commercially pure tungsten.* Materials Science and Engineering a-Structural Materials Properties Microstructure and Processing, 2008. **491**(1-2): p. 62-69.

20. Briant, C.L., *Potassium bubbles in tungsten wire.* Metallurgical Transactions A, 1993. **24**(5): p. 1073-1084.

21. Snow, D.B., *The recrystallization of commercially pure and doped tungsten wire drawn to high strain.* Metallurgical Transactions A, 1979. **10**(7): p. 815-821.

22. Smithells, C.J., *Tungsten its metallurgy, properties, and applications*. New York, New York, Chemical Publishing Company, 1953.

23. Jaffee, R. and C. Sims, *The effect of rhenium on the fabricability and ductility of molybdenum and tungsten*. Battelle Memorial Inst., Columbus, Ohio, 1958.

24. Klopp, W.D., P.L. Raffo, and W.R. Witzke, *Mechanical properties of dilute tungsten-rhenium alloys* (NASA-TN-D-3483). NASA Lewis Research Center, Cleveland, Ohio, 1966.

25. Garfinkle, M., W.R. Witzke, and W.D. Klopp, *Superplasticity in tungsten-rhenium alloys*. NASA Lewis Research Center, Cleveland, Ohio, 1969.

26. Churn, K.S. and R.M. German, *Fracture behavior of W-Ni-Fe heavy alloys.* Metallurgical Transactions A, 1984. **15**(2): p. 331-338.

27. Gero, R., L. Borukhin, and I. Pikus, *Some structural effects of plastic deformation on tungsten heavy metal alloys.* Materials Science and Engineering a-Structural Materials Properties Microstructure and Processing, 2001. **302**(1): p. 162-167.

28. Ekbom, L.B., *Tungsten heavy-metals.* Scandinavian Journal of Metallurgy, 1991. **20**(3): p. 190-197.

29. Zou, H., Y.C. Wang, and S.K. Li, *Effect of composition on microstructure and dynamic mechanical properties of W-Ni-Cu alloys.* Applied Science, Materials Science and Information Technologies in Industry, 2014. **513-517**: p. 121-124.

30. Humail, I.S., et al., *Tensile behavior change depending on the varying tungsten content of W-Ni-Fe alloys.* International Journal of Refractory Metals & Hard Materials, 2007. **25**(5-6): p. 380-385.

31. Bose, A., R. Sadangi, and R.M. German, *A review on alloying in tungsten heavy alloys.* Supplemental Proceedings: Materials Processing and Interfaces, Volume 1, 2012: p. 453-465.

32. Ryu, H. and S. Hong, *Effects of sintering conditions on mechanical properties of mechanically alloyed tungsten heavy alloys.* Metals and Materials International, 2001. **7**(3): p. 221-226.

33. Baek, W.H., et al., *Heat treatment behavior of tungsten heavy alloy*, in *Heat Treatment of Materials*, J.H. Sung, et al., Editors. 2006, Trans Tech Publications Ltd: Stafa-Zurich. p. 35-40.

34. Yu, Y., W.C. Zhang, and E.D. Wang, *Effect of heat treatment on microstructure and mechanical properties of hot-hydrostatically extruded 93W-4.9Ni-2.1Fe alloy.* Journal of Alloys and Compounds, 2015. **622**: p. 880-884.

35. Liu, J.X., et al., *Effect of fibrous orientation on dynamic mechanical properties and susceptibility to adiabatic shear band of tungsten heavy alloy fabricated through hot-hydrostatic extrusion.* Materials Science and Engineering a-Structural Materials Properties Microstructure and Processing, 2008. **487**(1-2): p. 235-242.

36. Das, J., et al., *Thermo-mechanical processing, microstructure and tensile properties of a tungsten heavy alloy.* Materials Science and Engineering: A, 2014. **613**(0): p. 48-59.

37. Gong, X., et al., *Microstructure and highly enhanced mechanical properties of fine-grained tungsten heavy alloy after one-pass rapid hot extrusion.* Materials Science and Engineering: A, 2011. **528**(10-11): p. 3646-3652.

38. Song, W.D. and J.G. Ning, *Dynamic mechanical characterization and optimization of particle-reinforced W-Ni-Fe composites.* Science China-Physics Mechanics & Astronomy, 2011. **54**(9): p. 1651-1658.

39. Huang, J.H., et al., *A study of mechanical properties of heavy tungsten alloys using computer numerical simulation - Influence of tungsten content on the properties of the alloys.* Rare Metal Materials and Engineering, 1998. **27**(6): p. 344-347.

40. Yu, Y., W. Zhang, and E. Wang, *Effect of heat treatment on microstructure and mechanical properties of hot-hydrostatically extruded 93W–4.9Ni–2.1Fe alloy.* Journal of Alloys and Compounds, 2015. **622**(0): p. 880-884.

41. Yan, Q., et al., *Effect of hot working process on the mechanical properties of tungsten materials.* Journal of Nuclear Materials, 2013. **442**(1–3, Supplement 1): p. S233-S236.

42. Leber, S., et al., *Fracture modes in tungsten wire.* Journal of the Less Common Metals, 1976. **48**(1): p. 119-133.

43. Li, K.-c.i., *Tungsten, its history, geology, ore-dressing, metallurgy, chemistry, analysis, applications, and economics*, ed. C.-y. Wang. 1955, New York, New York, Reinhold publishing corporation.

44. Yih, S.W.H. and C.T. Wang, *Tungsten: sources, metallurgy, properties, and applications*. 1979, New York, New York, Plenum Press.

45. Thompson, V. and V. Petersen, *Research on workable refractory alloys of tungsten, tantalum, molybdenum, and columbium*. 1963, DTIC Document.

46. Kecskes, L.J., et al., *Grain size engineering of bcc refractory metals: Top-down and bottom-up—Application to tungsten.* Materials Science and Engineering: A, 2007. **467**(1–2): p. 33-43.

47. Ganeev, A., R. Islamgaliev, and R. Valiev, *Refinement of tungsten microstructure upon severe plastic deformation.* The Physics of Metals and Metallography, 2014. **115**(2): p. 139-145.

48. Wurster, S., B. Gludovatz, and R. Pippan, *High temperature fracture experiments on tungsten–rhenium alloys.* International Journal of Refractory Metals and Hard Materials, 2010. **28**(6): p. 692-697.

49. Bechtold, J.H. and P.G. Shewmon, *Flow and fracture characteristics of annealed tungsten.* Transactions of the American Society for Metals, 1954. **46**: p. 397-408.

50. Gludovatz, B., et al., *Fracture toughness of polycrystalline tungsten alloys.* International Journal of Refractory Metals & Hard Materials, 2010. **28**(6): p. 674-678.

51. Schmidt, F.F. and H.R. Ogden, *The engineering properties of tungsten and tungsten alloys* (No. DMIC191). Battelle Memorial Inst. Defense Metals Information Center, Columbus, OH, 1963.

52. Hiraoka, Y. and H. Kurishita, *Low-temperature strengths and ductility of various tungsten sheets.* Advances in Materials Science and Engineering, 2011. (**2011**): p. 1-7.

53. Allen, B.C., D.J. Mayhuth, and R.I. Jaffee, *The recrystallization and ductile-brittle transition behaviour of tungsten-effect of impurities on polycrystals prepared from single crystals.* Journal of Institute of Metals, 1961. **90**(4): p. 120-128.

54. Sikora, P.F. and R.W. Hall, *High-temperature tensile properties of wrought sintered tungsten* (No. NASA-TN-D-79). NASA Lewis Research Center, Cleveland, Ohio, 1959.

55. Zhang, Y., et al., *Observations on the ductile-to-brittle transition in ultrafine-grained tungsten of commercial purity.* Materials Science and Engineering: A, 2009. **503**(1–2): p. 37-40.

56. Chawla, K., *Metallic Fibers.* Fibrous Materials, 1998: p. 108-131.

57. Bochniak, W., et al., *Mechanical properties of tungsten wires after cycling deformation treatment.* International Journal of Advanced Manufacturing Technology, 2013. **69**(9-12): p. 1955-1959.

58. Hampel, C.A., *Rare metals handbook*. 1954, New York, New York, Reinhold Pub. Corp.

59. Gumbsch, P., *Brittle fracture and the brittle-to-ductile transition of tungsten.* Journal of Nuclear Materials, 2003. **323**(2-3): p. 304-312.

60. Valiev, R.Z. and T.G. Langdon, *Principles of equal-channel angular pressing as a processing tool for grain refinement.* Progress in Materials Science, 2006. **51**(7): p. 881-981.

61. Segal, V.M., *Materials processing by simple shear.* Materials Science and Engineering: A, 1995. **197**(2): p. 157-164.

62. Segal, V.M., *Equal channel angular extrusion: from macromechanics to structure formation.* Materials Science and Engineering: A, 1999. **271**(1–2): p. 322-333.

63. Segal, V.M., *Engineering and commercialization of equal channel angular extrusion (ECAE).* Materials Science and Engineering a-Structural Materials Properties Microstructure and Processing, 2004. **386**(1-2): p. 269-276.

64. Bridgman, P.W., *Studies in large plastic flow and fracture with special emphasis on the effects of hydrostatic pressure*. Metallurgy and Metallurgical Engineering Series. 1952: New York-London, McGraw-Hill.

65. Zhang, Y., et al., *Influence of HPT deformation temperature on microstructures and thermal stability of ultra-fine-grained tungsten.* Materials Science Forum, 2008. **584-586**: p. 1000-1005.

66. Zhilyaev, A.P., et al., *Experimental parameters influencing grain refinement and microstructural evolution during high-pressure torsion.* Acta Materialia, 2003. **51**(3): p. 753-765.

67. Vorhauer, A., & Pippan, R., *On the homogeneity of deformation by high pressure torsion*. Scripta Materialia, 2005. **51**(9): p. 921-925.

68. Zhilyaev, A.P. and T.G. Langdon, *Using high-pressure torsion for metal processing: Fundamentals and applications.* Progress in Materials Science, 2008. **53**(6): p. 893-979.

69. Suryanarayana, C., *Mechanical alloying and milling.* Progress in Materials Science, 2001. **46**(1): p. 1-184.

70. Zhang, L.C., J. Xu, and E. Ma, *Consolidation and properties of ball-milled Ti50Cu18Ni22Al4Sn6 glassy alloy by equal channel angular extrusion.* Materials Science and Engineering: A, 2006. **434**(1–2): p. 280-288.

71. Senthil Saravanan, M.S. and S.P. Kumaresh Babu, *Synthesis, characterization, and ECAP consolidation of carbon nanotube reinforced AA 4032 nanocrystalline composites produced by high energy ball milling.* Journal of Engineering Materials and Technology, 2014. **137**(2): p. 021004.

72. Xu, W., et al., *Nanostructured multi-phase titanium based particulate composites consolidated by severe plastic deformation.* International Journal of Powder Metallurgy, 2014. **50**(1): p. 49-55.

73. Mathaudhu, S.N., et al., *Microstructures and recrystallization behavior of severely hot-deformed tungsten.* Materials Science and Engineering: A, 2009. **503**(1-2): p. 28-31.

74. Yu, Y., et al., *Effect of swaging on microstructure and mechanical properties of liquid-phase sintered 93W-4.9(Ni, Co)-2.1Fe alloy.* International Journal of Refractory Metals and Hard Materials, 2014. **44**(0): p. 103-108.

75. Goloborodko, A., et al., *Effect of pressing temperature on fine-grained structure formation in 7475 aluminum alloy during ECAP.* Materials Science and Engineering A, 2004. **381**(1-2): p. 121-128.

76. Kim, I., et al., *Effects of equal channel angular pressing temperature on deformation structures of pure Ti.* Materials Science and Engineering: A, 2003. **342**(1–2): p. 302-310.

77. Málek, P., M. Cieslar, and R.K. Islamgaliev, *The influence of ECAP temperature on the stability of Al-Zn-Mg-Cu alloy.* Journal of Alloys and Compounds, 2004. **378**(1-2): p. 237-241.

78. Wang, Y.Y., et al., *Effect of deformation temperature on the microstructure developed in commercial purity aluminum processed by equal channel angular extrusion.* Scripta Materialia, 2004. **50**(5): p. 613-617.

79. Semchyshen, M., et al., *Development of high-strength molybdenum-and tungsten-base alloys*. Climax Molybdenum Co of Michigan, Ann Arbor, MI 1966.

80. Raffo, P.L., *Yielding and fracture in tungsten and tungsten-rhenium alloys.* Journal of the Less Common Metals, 1969. **17**(2): p. 133-149.

81. Wurster, S., B. Gludovatz, and R. Pippan, *High temperature fracture experiments on tungsten-rhenium alloys.* International Journal of Refractory Metals & Hard Materials, 2010. **28**(6): p. 692-697.

82. Jan-C, C. and B.D. Bryskin, *Rhenium - A unique rare metal*. Material and Manufacturing Process, 1994. **9**(6): p 1087-1104.

83. Klopp, W.D., *Review of ductilizing of group VIA elements by rhenium and other solutes* (No. NASA-TN-D-4955). NASA Lewis Research Center, Cleveland, OH 1968.

84. Pink, E. and R. Eck, *Refractory metals and their alloys.* Materials Science and Technology, 2006.

85. Sell, H.G., *Advanced processing pechnology and high temperature mechanical properties of tungsten base alloys*, in *Refractory Metal Alloys*, I. Machlin, R.T. Begley, and E.D. Weisert, Editors. 1968, New York, New York, Plenum Press. p. 395-439.

86. Blocher, J.M., *Structure/property/process relationships in chemical vapor deposition CVD.* Journal of Vacuum Science & Amp; Technology, 1974. **11**(4): p. 680-686.

87. Huegel, F.J. and W.R. Holman, *CVD tungsten and tungsten-rhenium alloys for structural applications. 3. Recent developemnts.* Journal of the Electrochemical Society, 1970. **117**(3): p. C103.

88. Federer, J.I. and C.F. Leitten, *Vapor deposition and characterization of tungsten-rhenium alloys.* Nuclear Applications, 1965. **1**(6): p. 575-580.

89. Snow, D.B., *Identification of second phases within bubbles in annealed doped tungsten wire.* Metallurgical Transactions, 1974. **5**(11): p. 2375-2381.

90. Palacios, T., et al., *Microstructural and mechanical characterization of annealed tungsten (W) and potassium-doped tungsten foils.* International Journal of Refractory Metals and Hard Materials, 2015. **48**: p. 145-149.

91. Schade, P., *100years of doped tungsten wire.* International Journal of Refractory Metals and Hard Materials, 2010. **28**(6): p. 648-660.

92. Walter, J. and K. Lou, *Structures and chemistry of tungsten powder from doped and undoped tungsten blue oxide.* Journal of Materials Science, 1989. **24**(10): p. 3577-3587.

93. Trattner, H., *Tungsten-thorium dioxide-aluminum oxide mass for a high-temperature-resistant emission electrode and process for the production thereof.* 1976, Google Patents.

94. Atkinson, R.H., G.H. Keith, and R.C. Koo, *Tungsten and tungsten-base alloys*, in *refractory metals and alloys*, M. Semchyshen and J.J. Harwood, Editors. 1960, Interscience Publishers, INC: New York, New York. p. 319-355.

95. Langmuir, I., *Chandler Lecture - "Electrochemical Interactions of Tungsten, Thorium Caesium, and Oxygen".* Industrial & Engineering Chemistry, 1930. **22**(4): p. 390-393.

96. Srikanth, V. and G.S. Upadhyaya, *Contiguity variation in tungsten spheroids of sintered heavy alloys.* Metallography, 1986. **19**(4): p. 437-445.

97. Fu, C.C., et al., *Microstructure and mechanical properties of solid-phase sintered heavy tungsten alloy*, in *Thermec 2006 Supplement: 5th International Conference on Processing and Manufacturing of Advanced Materials*, T. Chandra, et al., Editors. 2007, Trans Tech Publications Ltd: Stafa-Zurich. p. 575-580.

98. Das, J., et al., *Hardness and tensile properties of tungsten based heavy alloys prepared by liquid phase sintering technique.* International Journal of Refractory Metals & Hard Materials, 2009. **27**(3): p. 577-583.

99. Zhang, Z.-W., et al., *Phase transformation and thermal stability of mechanically alloyed W–Ni–Fe composite materials.* Materials Science and Engineering: A, 2004. **379**(1–2): p. 148-153.

100. Upadhyaya, A., S.K. Tiwari, and P. Mishra, *Microwave sintering of W-Ni-Fe alloy.* Scripta Materialia, 2007. **56**(1): p. 5-8.

101. Ryu, H.J. and S.H. Hong, *Effects of sintering conditions on mechanical properties of mechanically alloyed tungsten heavy alloys.* Metals and Materials-Korea, 2001. **7**(3): p. 221-226.

102. Jang, J.S.C., et al., *Study on the solid-phase sintering of the nano-structured heavy tungsten alloy powder.* Journal of Alloys and Compounds, 2007. **434–435**(0): p. 367-370.

103. Rabin, B.H. and R.M. German, *Microstructure effects on tensile properties of tungsten-Nickel-Iron composites.* Metallurgical Transactions A, 1988. **19**(6): p. 1523-1532.

104. Bourguignon, L.L. and R.M. German, *Sintering temperature effects on a tungsten heavy alloy.* International Journal of Powder Metallurgy, 1988. **24**(2): p. 115-121.

105. Kim, D.-K., S. Lee, and J.-W. Noh, *Dynamic and quasi-static torsional behavior of tungsten heavy alloy specimens fabricated through sintering, heat-treatment, swaging and aging.* Materials Science and Engineering: A, 1998. **247**(1–2): p. 285-294.

106. Fan, J., et al., *Thermal stability, grain growth and structure changes of mechanically alloyed W–Ni–Fe composite during annealing.* International Journal of Refractory Metals and Hard Materials, 2001. **19**(2): p. 73-77.

107. Ravi Kiran, U., et al., *Swaging and heat treatment studies on sintered 90W–6Ni–2Fe–2Co tungsten heavy alloy.* International Journal of Refractory Metals and Hard Materials, 2012. **33**(0): p. 113-121.

108. Liu, H., et al., *Densification, microstructure and mechanical properties of 90W–4Ni–6Mn heavy alloy.* International Journal of Refractory Metals and Hard Materials, 2013. **37**(0): p. 121-126.

109. Taya, M. and R.J. Arsenault, *Metal matrix composites thermomechanical behavior*. 1989, Elmsford, New York, Pergamon Press.

110. Coates, R. and K. Ramesh, *The rate-dependent deformation of a tungsten heavy alloy.* Materials Science and Engineering: A, 1991. **145**(2): p. 159-166.

111. Srikanth, V. and G.S. Upadhyaya, *Effect of cold work and annealing on the mechanical-properties of 90W-7Ni-3Fe heavy alloy.* Journal of Materials Science Letters, 1988. **7**(3): p. 195-197.

112. Ramesh, K.T. and R.S. Coates, *Microstructural influences on the dynamic-response of tungsten heavy alloys.* Metallurgical Transactions a-Physical Metallurgy and Materials Science, 1992. **23**(9): p. 2625-2630.

113. Rittel, D., R. Levin, and A. Dorogoy, *On the isotropy of the dynamic mechanical and failure properties of swaged tungsten heavy alloys.* Metallurgical and Materials Transactions a-Physical Metallurgy and Materials Science, 2004. **35A**(12): p. 3787-3795.

114. Kiran, U.R., et al., *Tensile and impact behavior of swaged tungsten heavy alloys processed by liquid phase sintering.* International Journal of Refractory Metals & Hard Materials, 2013. **37**: p. 1-11.

115. Caliskan, N.K., N. Durlu, and S. Bor, *Swaging of liquid phase sintered 90W-7Ni-3Fe tungsten heavy alloy.* International Journal of Refractory Metals & Hard Materials, 2013. **36**: p. 260-264.

116. Gero, R., L. Borukhin, and I. Pikus, *Some structural effects of plastic deformation on tungsten heavy metal alloys.* Materials Science and Engineering: A, 2001. **302**(1): p. 162-167.

117. Lee, W.S., G.L. Xiea, and C.F. Lin, *The strain rate and temperature dependence of the dynamic impact response of tungsten composite.* Materials Science and Engineering a-Structural Materials Properties Microstructure and Processing, 1998. **257**(2): p. 256-267.

118. Scapin, M., *Mechanical characterization and modeling of the heavy tungsten alloy IT180.* International Journal of Refractory Metals and Hard Materials, 2015. **50**(0): p. 258-268.

119. Bose, A., D. Sims, and R. German, *Test temperature and strain rate effects on the properties of a tungsten heavy alloy.* Metallurgical Transactions A, 1988. **19**(3): p. 487-494.

120. Yadav, S. and K. Ramesh, *The mechanical properties of tungsten-based composites at very high strain rates.* Materials Science and Engineering: A, 1995. **203**(1): p. 140-153.

121. Wei, Z., et al., *Influence of stress condition on adiabatic shear localization of tungsten heavy alloys.* International Journal of Impact Engineering, 2001. **26**(1): p. 843-852.

122. Zhou, M., *Effects of microstructure on resistance to shear localization for a class of metal matrix composites.* Fatigue & fracture of engineering materials & structures, 1998. **21**(4): p. 425-438.

123. Dümmer, T., et al., *Effect of strain rate on plastic flow and failure in polycrystalline tungsten.* Acta Materialia, 1998. **46**(17): p. 6267-6290.

124. Mrovec, M., C. Elsässer, and P. Gumbsch, *Atomistic simulations of lattice defects in tungsten.* International Journal of Refractory Metals and Hard Materials, 2010. **28**(6): p. 698-702.

125. Bilello, J.C., *Nucleation of brittle fracture in sintered tungsten at low temperatures.* Transactions of the Metallurgical Society of AIME, 1968. **242**(4): p. 703-8.

126. Rupp, D. and S. Weygand, *Anisotropic fracture behaviour and brittle-to-ductile transition of polycrystalline tungsten.* Philosophical Magazine, 2010. **90**(30): p. 4055-4069.

127. Argon, A.S. and S.R. Maloof, *Plastic deformation of tungsten single crystals at low temperatures.* Acta Metallurgica, 1966. **14**(11): p. 1449-1462.

128. Rupp, D. and S.M. Weygand, *Experimental investigation of the fracture toughness of polycrystalline tungsten in the brittle and semi-brittle regime.* Journal of Nuclear Materials, 2009. **386**: p. 591-593.

129. Giannattasio, A., et al., *Brittle-ductile transitions in polycrystalline tungsten.* Philosophical Magazine, 2010. **90**(30): p. 3947-3959.

130. Stephens, J.R., *Effects of interstitial impurities on the low-temperature tensile properties of tungsten* (No. NASA-TN-D-2287). NASA Lewis Research Center, Cleveland, OH, 1964.

131. Krasko, G.L., *Effect of impurities on the electronic structure of grain boundaries and intergranular cohesion in iron and tungsten.* Materials Science and Engineering a-Structural Materials Properties Microstructure and Processing, 1997. **234**: p. 1071-1074.

132. Pan, Z., L.J. Kecskes, and Q. Wei, *The nature behind the preferentially embrittling effect of impurities on the ductility of tungsten.* Computational Materials Science, 2014. **93**: p. 104-111.

133. Giannattasio, A. and S.G. Roberts, *Strain-rate dependence of the brittle-to-ductile transition temperature in tungsten.* Philosophical Magazine, 2007. **87**(16-17): p. 2589-2598.

134. Hull, D., P. Beardmore, and A. Valintine, *Crack propagation in single crystals of tungsten.* Philosophical Magazine, 1965. **12**(119): p. 1021-1041.

135. Brunner, D., *Temperature dependence of the plastic flow of high-purity tungsten single crystals.* International Journal of Materials Research, 2010. **101**(8): p. 1003-1013.

136. Ripoll, M.R., E. Reisacher, and H. Riedel, *Texture induced tension–compression asymmetry of drawn tungsten wires.* Computational Materials Science, 2009. **45**(3): p. 788-792.

137. Margevicius, R.W., J. Riedle, and P. Gumbsch, *Fracture toughness of polycrystalline tungsten under mode I and mixed mode I/II loading.* Materials Science and Engineering: A, 1999. **270**(2): p. 197-209.

138. Chilton, A. and A. Wronski, *The effects of strain rate and pressurization on the ductile-brittle transition temperature of polycrystalline sintered tungsten.* Journal of the Less Common Metals, 1969. **17**(4): p. 447-450.

139. Pan, Z., et al., *Quasi-static and dynamic mechanical properties of commercial-purity tungsten processed by ECAE at low temperatures.* Journal of Materials Science, 2008. **43**(23-24): p. 7379-7384.

140. Lee, W.S., C.F. Lin, and G.L. Xiea, *Dynamic shear deformation and failure behaviour of pure polycrystalline tungsten.* Materials Science and Engineering a-Structural Materials Properties Microstructure and Processing, 1998. **247**(1-2): p. 102-112.

141. Giannattasio, A. and S.G. Roberts, *Strain-rate dependence of the brittle-to-ductile transition temperature in tungsten.* Philosophical Magazine, 2007. **87**(17): p. 2589-2598.

142. Subhash, G., Y.J. Lee, and G. Ravichandran, *Plastic deformation of CVD textured tungsten—I. Constitutive response.* Acta Metallurgica et Materialia, 1994. **42**(1): p. 319-330.

143. Subhash, G., Y. Lee, and G. Ravichandran, *Plastic deformation of CVD textured tungsten—II. Characterization.* Acta Metallurgica et Materialia, 1994. **42**(1): p. 331-340.

144. Hirsch, P. and S. Roberts, *The dynamics of edge dislocation generation along a plane orthogonal to a mode I crack.* Scripta Metallurgica, 1989. **23**(6): p. 925-930.

145. Hartmaier, A. and P. Gumbsch, *On the activation energy for the brittle/ductile transition.* Physica Status Solid B Basic Research, 1997. **202**: p. R1-R2.

146. Chen, Z., M. Mrovec, and P. Gumbsch, *Dislocation–vacancy interactions in tungsten.* Modelling and Simulation in Materials Science and Engineering, 2011. **19**(7): p. 074002.

147. Rupp, D., et al., *Fracture toughness and microstructural characterization of polycrystalline rolled tungsten.* International Journal of Refractory Metals and Hard Materials, 2010. **28**(6): p. 669-673.

148. Habainy, J., et al., *Fatigue behavior of rolled and forged tungsten at 25°, 280° and 480° C.* Journal of Nuclear Materials, 2015. **465**: p. 438-447.

149. Lee, H. and V. Tomar, *Understanding effect of grain boundaries in the fracture behavior of polycrystalline tungsten under mode-I loading.* Journal of Engineering Materials and Technology-Transactions of the Asme, 2012. **134**(3): p. 031010.

150. Zhang, X., et al., *Texture evolution and basic thermal–mechanical properties of pure tungsten under various rolling reductions.* Journal of Nuclear Materials, 2016. **468**: p. 339-347.

151. Lu, W.R., C.Y. Gao, and Y.L. Ke, *Constitutive modeling of two-phase metallic composites with application to tungsten-based composite 93W-4.9Ni-2.1Fe.* Materials Science and Engineering a-Structural Materials Properties Microstructure and Processing, 2014. **592**: p. 136-142.

152. Dunstan, D. and A. Bushby, *Grain size dependence of the strength of metals: the Hall–Petch effect does not scale as the inverse square root of grain size.* International Journal of Plasticity, 2014. **53**: p. 56-65.